

COLLOIDAL METAL PYROPHOSPHATE SALTS

PREPARATION, PROPERTIES AND APPLICATIONS

COLLOÏDALE METAAL-PYROFOSFAATZOUTEN

BEREIDING, EIGENSCHAPPEN EN TOEPASSINGEN

(MET EEN SAMENVATTING IN HET NEDERLANDS)

PROEFSCHRIFT

ter verkrijging van de graad van doctor aan de Universiteit Utrecht op gezag van de rector magnificus, prof.dr. G.J. van der Zwaan, ingevolge het besluit van het college voor promoties in het openbaar te verdedigen op woensdag 20 februari 2013 om 10.30 uur

door

YOURI MIKAL VAN LEEUWEN

geboren op 21 april 1984 te Utrecht

PROMOTOREN

Prof.dr. W.K. Kegel
Prof.dr. A.P. Philipse

Co-PROMOTOR

Dr. K.P. Velikov

Dit proefschrift werd mede mogelijk gemaakt met financiële steun van Agentschap NL als onderdeel van het Food Nutrition Delta Program

COVER DESIGN

Jorn van Leeuwen

www.JornvanLeeuwen.nl

FRONT COVER

$\text{Ca}_2\text{P}_2\text{O}_7$ (*Calcium pyrofosfaat kristallen*)

67,8 x 95,8 cm, olieverf op doek, 2012

BACK COVER

$\text{Fe}_4(\text{P}_2\text{O}_7)_3$ (*IJzer pyrofosfaat-eiwit composietdeeltje*)

80,0 x 88,0 cm, olieverf op doek, 2012

PRINTED BY

Proefschriftmaken.nl || Printyourthesis.com

ISBN

978-90-3935-907-5

Voor Merel

THE FOLLOWING CHAPTERS ARE BASED ON PUBLICATIONS

CHAPTER 2: Y.M. van Leeuwen, K.P. Velikov and W.K. Kegel

MORPHOLOGY OF COLLOIDAL METAL PYROPHOSPHATE SALTS 

RSC Advances, **2012**, 2, 2534-2540

CHAPTER 4: Y.M. van Leeuwen, K.P. Velikov and W.K. Kegel

STABILIZATION THROUGH PRECIPITATION IN A SYSTEM OF COLLOIDAL IRON(III) PYROPHOSPHATE SALTS 

Journal of Colloid and Interface Science, **2012**, 381, 43-47

CHAPTER 5: Y.M. van Leeuwen, K.P. Velikov and W.K. Kegel

REPEPTIZATION BY DISSOLUTION IN A COLLOIDAL SYSTEM OF IRON(III) PYROPHOSPHATE 

Langmuir, **2012**, 28, 16531–16535

CHAPTER 7 has been submitted for publication

OTHER PUBLICATIONS BY THE AUTHOR

S.H. Wadman, Y.M. van Leeuwen, R.W.A. Havenith, G.P.M. van Klink, and G. van Koten

A REDOX ASYMMETRIC, CYCLOMETALATED RUTHENIUM DIMER: TOWARD UPCONVERSION DYES IN DYE-SENSITIZED TiO₂ SOLAR CELLS 

Organometallics, **2010**, 29, 5635–5645

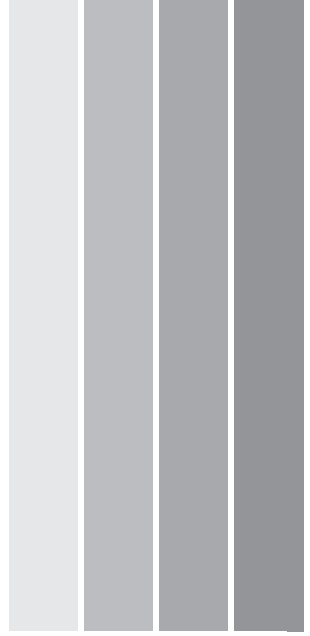
J. Pacifico, Y.M. van Leeuwen, M. Spuch-Calvar, A. Sánchez-Iglesias, L. Rodríguez-Lorenzo, J. Pérez-Juste, I. Pastoriza-Santos and L.M. Liz-Marzán

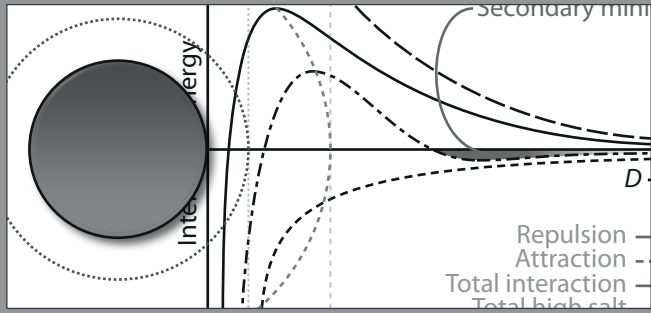
FIELD GRADIENT IMAGING OF NANOPARTICLE SYSTEMS: ANALYSIS OF GEOMETRY AND SURFACE COATING EFFECTS 

Nanotechnology, **2009**, 20, 095708

TABLE OF CONTENTS

 CHAPTER 1	1
<i>Introduction</i>	
 CHAPTER 2	13
<i>Morphology of Colloidal Metal Pyrophosphate Salts</i>	
 CHAPTER 3	23
<i>Preparation of Colloidal Mⁿ-Pyrophosphate Salts</i>	
 CHAPTER 4	35
<i>Stabilization through Precipitation in a System of Colloidal Iron(III) Pyrophosphate Salts</i>	
 CHAPTER 5	45
<i>Repeptization by Dissolution in a System of Colloidal Iron(III) Pyrophosphate</i>	
 CHAPTER 6	55
<i>Morphology and Stability of Mixed-Metal Pyrophosphate Salts</i>	
 CHAPTER 7	67
<i>A General Preparation Method for Biocompatible Composite Nanoparticles</i>	
 CHAPTER 8	77
<i>Reactivity of Colloidal Iron-Containing Pyrophosphate Salts</i>	
SUMMARY	87
SAMENVATTING	91
APPENDICES	99
DANKWOORD	111





CHAPTER 1

INTRODUCTION

1.1 INTRODUCTION

The fortification of food products with nanoparticles is an important field of research for food industry as the addition of such particles can be an efficient, simple and cost-effective way to fight mineral deficiencies both in developed and third world countries [1, 2]. The addition of iron to foodstuffs is the most problematic, mainly due to the reactivity of 'free' iron ions (from for instance iron sulfate) with various components of the products such as the polyphenols that are abundant in plant-based foodstuffs [3]. A more detailed discussion on this topic will follow in CHAPTER 8.

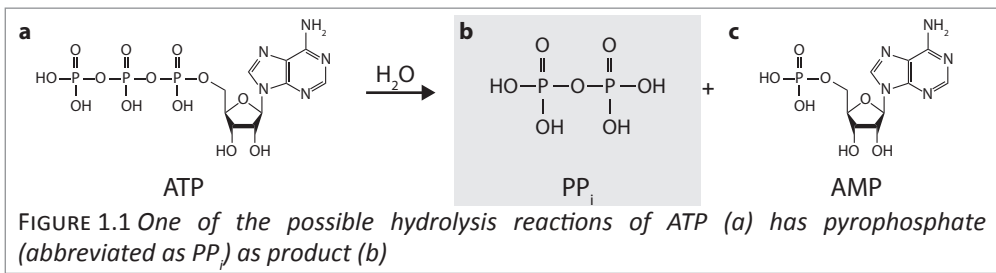
The main goal of this thesis is to contain the cation in small inorganic nanoparticles in order to reduce the reactivity of the iron as compared to ionic iron in solution. Next to edibility, an important prerequisite for these particles is that they should be insoluble in the food product (protecting the iron from reaction), but need to dissolve once consumed in order to allow the iron to be absorbed by the body. Therefore, we will make use of metal pyrophosphate salts that, while having a low solubility, are still capable of sufficiently fast dissolution in gastric conditions [4, 5]. Control over the size of the resulting particles will be beneficial here as the particles need to be large enough to prevent dissolution in the food product, while they should be small enough not to be noticed by the consumer.

Once we have obtained a suitable system of iron pyrophosphate we will incorporate a second mineral such as calcium with the purpose to dilute the (surface) concentration of iron in the particles, with the intent to further reduce its reactivity. An added benefit is that combining iron with other dietary minerals such as calcium, zinc or magnesium would make the resulting particles a multi-purpose, widely applicable delivery system for micronutrients [6, 7].

1.2 METAL PYROPHOSPHATE SALTS

In the preparation of inorganic iron-containing particles we use pyrophosphate (diphosphate or $P_2O_7^{4-}$, abbreviated in this thesis as PP_i) to precipitate the metal cations in an insoluble salt. Pyrophosphate is part of the biological energy cycle and DNA synthesis: it is released upon hydrolysis of adenosine triphosphate (ATP) to adenosine monophosphate (AMP): $ATP \rightarrow AMP + PP_i$, see FIGURE 1.1 [8]. In combination with most multivalent cations, pyrophosphate forms insoluble complexes in water [9-11] and its role as ligand has been widely studied [12, 13]. Metal pyrophosphate salts are known for their chemical and structural complexity [14] and wide industrial applications. They are used in catalysis [15-17], as solid electrolytes [18], as battery electrodes [19-21] and in phosphate glasses for immobilisation of nuclear waste [22]. Biomedical applications include artificial bone transplant material [23] and photoluminescent probes [24].

Furthermore, a type of arthritis known as pseudogout is caused by the deposition of small amounts of calcium pyrophosphate (CaPP_i) in articular tissue [25, 26] and thus



studying the formation of calcium pyrophosphate might be insightful for the treatment of this disease. Finally, as iron(III) pyrophosphate (ferric pyrophosphate, FePP) is the only white iron-containing material, it is commercially available as a food additive and mineral supplement [27]. It is a useful material for fighting iron deficiency by means of food fortification because of its good bioaccessibility [4-6, 28] and lack of colour. However, the current commercial product consists of large (aggregates of) particles dispersed by high concentrations of stabilizing molecules.

Most of the literature referred to above focuses on the preparation and characterization of macroscopic crystals and bulk materials while many of these applications would greatly benefit from a different, colloidal approach. In this thesis we prepare metal pyrophosphate salts as dispersions of colloidal particles in water. The size of these colloidal particles (ranging from nanometers to micrometers by definition [29]) allows for a greater solubility rate than macroscopic powders, while the resulting systems will still benefit from the reduced reactivity and the ability to remain dispersed for long periods of time [2, 30, 31].

1.3 COLLOIDAL INTERACTIONS

A significant part of the thesis will deal with the colloidal stability of the prepared materials. Here we briefly review two concepts that are crucial in the understanding and analysis of colloidal stability: DLVO theory (describing interparticle interactions) and zeta-potential analysis (as an indicator for the stability of the dispersions).

1.3.1 INTERPARTICLE INTERACTIONS

For various inorganic colloidal systems the interparticle interactions are predominantly composed of van der Waals attraction and double layer repulsion. These so-called electrostatic colloids can be described by the Derjaguin-Landau-Verweij-Overbeek (DLVO) theory, in which the attractive and repulsive potentials combined yield the full interaction potential [32, 33].

VAN DER WAALS ATTRACTION. The attractive potential is summarized by the Van der Waals force, a combination of the forces between molecules caused by (fluctuating) dipole interactions, either permanent or induced. When extending these forces to the interaction between two large objects such as colloids, the interactions can be treated as the pairwise interaction of the molecules within these objects as shown by Hamaker [34]. The resulting attractive potential for two spheres with equal radius will then be

$$u_{att} = -\frac{A}{6} \left(\frac{2}{s^2 - 4} + \frac{2}{s^2} + \ln \left[\frac{s^2 - 4}{s^2} \right] \right), \quad (i1)$$

where A is the Hamaker constant, $s = x/r$, r is the particle radius and x the center-to-

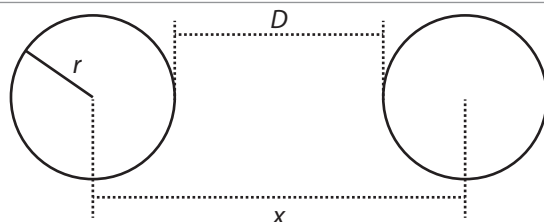


FIGURE 1.2 The three size variables r (radius), x (center-to-center distance) and D (surface-to-surface distance).

center distance between two particles, see FIGURE 1.2 [32]. The more commonly used abbreviated form

$$u_{att} = -Ar / 12D \quad (\text{i2})$$

is only valid for large particles at small separation distances, $r \gg D$. It can be seen from equation (i1) that besides the particle radius and separation distance, the calculation of this potential for two interacting spheres will only depend on the so-called Hamaker constant that is a result of the material properties:

$$A = \pi^2 C \rho_1 \rho_2, \quad (\text{i3})$$

with ρ_1 and ρ_2 the number of atoms or per unit volume in the two particles and C the pair interaction coefficient [34]. The Van der Waals force is a relatively short-distance force compared to electrostatic interactions but almost always dominates at short separation distances for colloidal particles.

DOUBLE LAYER REPULSION. A charged object immersed in a medium containing ions will attract oppositely charged ions to its surface. The resulting excess of ions near the object will create a so-called electric double layer; a layer of medium containing a high concentration of ions that screens the surface charge from its surroundings. When two such objects come in close proximity, the overlap of their double layers will result in an osmotic pressure forcing the objects apart. For two identical spheres the resulting repulsive potential between them will be [32, 33]

$$u_{rep} = \frac{64\pi k_B T r \rho}{\kappa^2} \gamma^2 e^{-\kappa D}, \quad (\text{i4})$$

with ρ the ionic strength in particles per m^3 , k_B the Boltzmann constant, T absolute temperature and κ the inverse Debye length:

$$\kappa = \left(\sum_i \rho_i e^2 z_i^2 / \varepsilon_r \varepsilon_0 kT \right)^{1/2}, \quad (\text{i5})$$

with e the elementary charge, z_i the valence of ion i , ε_0 the vacuum permittivity and ε_r the relative permittivity of the solvent. Finally,

$$\gamma = \tanh \frac{ve\psi_0}{4k_B T}, \quad (\text{i6})$$

where v is the valence of the electrolyte, e the elementary charge and ψ_0 the surface potential in mV [33]. Expression (i4) has been derived assuming a constant surface potential during the particle approach and is only accurate for separation distances larger than about one Debye length. At closer distances approximate models need to be applied to describe the interactions, assuming either a constant surface charge or a constant surface potential [33, 35].

TOTAL INTERACTION POTENTIAL. DLVO theory combines the attractive and repulsive potentials to yield the total interaction potential between two objects, see FIGURE 1.3a for a schematic representation of the interaction between two colloids in an ion-containing medium. The ionic strength is an experimental handle that can be used to influence the interactions by

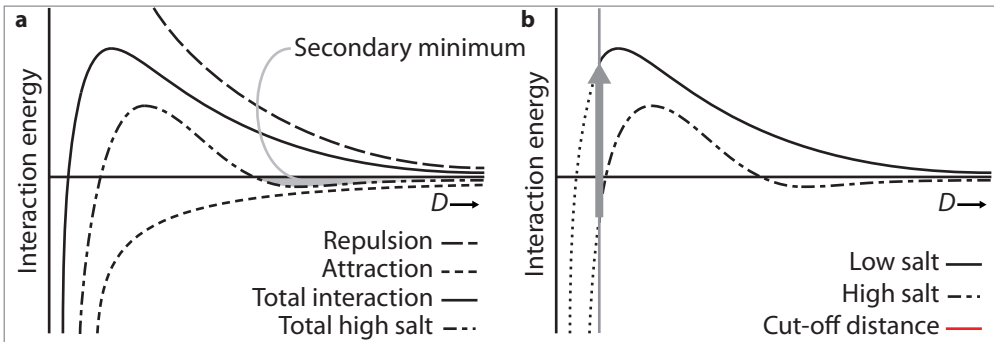


FIGURE 1.3 (a) Schematic representation of interparticle interaction potentials: the van der Waals attraction from eqn. (i1) (short dash) and the double layer repulsion from eqn. (i4) (long dash) together yield the total interaction potential (solid line). With increasing ionic strength, the repulsion decreases and the total potential first forms a secondary minimum (dot-dashed line) before the maximum completely disappears and the attraction dominates over all distances. (b) With the introduction of a cut-off distance, the deepest part of the primary minimum is unavailable to the particles (dotted lines) but it will still be negative at high ionic strengths (dot-dashed line). Under certain conditions, restoring the ionic strength to a lower value (arrow) will increase the maximum but also make the primary minimum positive, allowing for re-entrant aggregation.

changing the repulsive part of the potential; at low ionic strength the potential will consist of a deep primary minimum close to the particle surface and a high maximum or barrier preventing the particles from aggregating (solid line in FIGURE 1.3a). At intermediate ionic strength this barrier will decrease and a readily accessible secondary minimum will appear that may induce flocculation of the dispersion (dot-dashed line). At high ionic strength the repulsion will be negligible compared to the attraction potential and there will be no barrier left to stabilize the particles from complete aggregation in the primary minimum (short-dashed line). From experimental observations it is known that (i) washing away excess salts can result in restabilization (repeptization) of an aggregated dispersion, (ii) freshly aggregated systems are more readily repeptized and (iii) the timespan in which the system can still be repeptized depends on its temperature during storage [36].

While DLVO theory does predict repeptization from the secondary minimum of the interaction potential, restabilization of nanoparticles trapped in the primary minimum is not readily explained: the primary minimum is simply too deep to allow for redispersion of aggregated particles. To reconcile with the experimental observations mentioned above, additional theories were developed in which a cut-off distance was introduced below which the particles initially cannot enter [36-38]. Such a cut-off distance arises in an electrocratic system if interparticle interactions during a Brownian collision occur under constant surface charge instead of constant surface potential, as the re-equilibration needed for a constant potential takes place in a timespan orders of magnitude larger than that of the collisions. With this new distance of closest approach, the primary minimum might be shallow enough for the particles to be repeptized again upon subsequent increase of the ionic strength, see FIGURE 1.3b. However, the longer the particles are trapped within this shallow minimum, the more time the system has to re-equilibrate and irreversibly aggregate. This explains why fresh systems are more readily repeptized and why the timespan in which the system can still be repeptized depends on its temperature.

1.3.II ZETA POTENTIAL

The zeta-potential (ZP) is often used as an indicator for the stability of electrostatic dispersions [39] and it will be used extensively throughout this thesis. It can be derived from the analysis of the electrophoretic mobility of particles in dispersion; the movement of charged objects through a medium when an electric field is applied. However, the object moving through the medium is not just the particle itself, but also includes a surrounding 'cloud' of ions and solvent molecules that move along with it [40].

A schematic overview of the Stern model for a particle in a solvent containing ions is shown in FIGURE 1.4. The lower part depicts the electrostatic potential ψ_d which will be influenced by a number of factors. First of all, the surface charge and potential ψ_0 (i) are determined by the surface properties of the material, which can be influenced by the composition and pH of the solvent. Possible causes for such a surface charge are chargeable groups (e.g. acid or base), differential solution of one of the components (e.g. AgI nanoparticles) and isomorphous substitution in a surface (e.g. clays and zeolites) [29]. Next, ions from the medium can specifically adsorb at the surface of the particles in the so-called Stern layer (ii), leading to dampening of the potential and possibly even sign inversion for strongly adsorbing or multivalent ions. Finally, the slipping plane (iii) separates the solvent molecules that are bound to the surface of the particle from the mobile molecules in the bulk; the zeta-potential then is the electric potential at this plane. Another issue that is often ignored is the surface roughness that is present in every system and which can have a large effect on the schematic representation shown in FIGURE 1.4

This qualitative description already highlights a major problem of the model. While the surface potential ψ_0 is set by the (surface) properties of the material, the zeta-potential is

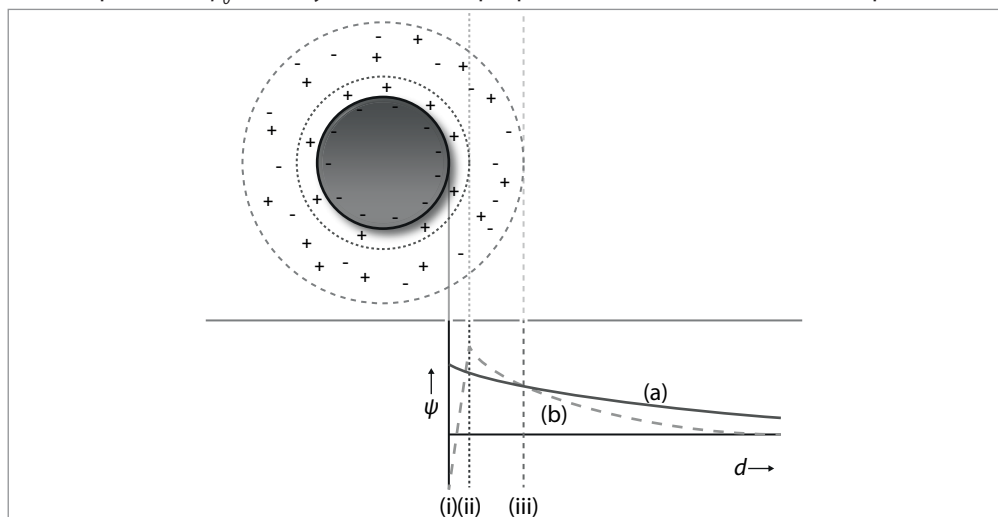


FIGURE 1.4 Top: schematic overview of a charged particle in an ion-containing medium. The surface properties of the particle determine the surface potential (i). Ions can adsorb specifically (close) to the surface, within the Stern layer (ii). Associated ions are also contained in the layer up to the slipping plane (iii). The electric potential at this plane is the zeta-potential. Bottom: two electrostatic potentials resulting in the same zeta-potential but with very different characteristics: the potential of a system without specific adsorption decreases slowly over the distance from the surface (a), while the potential of a system with specific adsorption (b) can result in complete charge inversion after the Stern layer.

the electric potential at a plane 'a certain distance from the surface', located at or beyond the Stern layer [41]. This means that the zeta-potential is only an indirect consequence of ψ_0 as the potential is already (partially) screened by the adsorbed ions in the first layer, causing a complex relation between the two as shown schematically in the lower part of FIGURE 1.4. The exact location and nature of this model plane and what factors determine its distance from the surface are a matter of debate [35, 41]. This is exemplified by the fact that the zeta-potential can be method-dependent under certain conditions. Another issue that is rarely discussed is the surface roughness of the particles which will have a strong influence on the schematic representation in FIGURE 1.4 and the model in general.

Regardless of the discussion on the theory and models behind it, experimentalists have been using the zeta-potential for decades as a measure of colloidal stability. As a rule of thumb a zeta-potential of (-)40 mV is considered the minimum for colloidal stability of electrocratic colloids in aqueous dispersions [42].

1.4 OUTLINE OF THIS THESIS

The goal of this thesis is to prepare stable colloidal dispersions of iron-containing (inorganic) materials and to assess whether the incorporation of iron into such a particle reduces its reactivity. The thesis is divided in three sections: Preparation, Properties and Applications.

In SECTION 1: PREPARATION we will discuss various ways to prepare colloidal metal pyrophosphate salts, detailing the coprecipitation method in CHAPTER 2 and the pH-dependent precipitation of $M^{II}PP_i$ s in CHAPTER 3. We find that simple coprecipitation can be used to prepare stable dispersions of $M^{III}PP_i$, but the resulting $M^{III}PP_i$ s will sediment completely within minutes to hours. The pH-dependent method can be used to prepare stable colloidal dispersions of $MgPP_i$, but using calcium or zinc as the cation will still yield unstable systems.

In SECTION 2: PROPERTIES we start with two chapters discussing the colloidal stability of iron pyrophosphate. We find unexpected behaviour of $FePP_i$ in two ways: first, in CHAPTER 4 we show that while the nanoparticles that form during preparation are unstable and immediately aggregate into larger clusters, these clusters can remain stable in dispersion for long periods of time. Second, in CHAPTER 5 we find that aggregated systems of $FePP_i$ can be redispersed under circumstances that should not allow for reprecipitation according to common (experimental) knowledge. CHAPTER 6 investigates the morphology and stability of mixed-metal pyrophosphate salts. Here we show that stable dispersions of mixed systems can be prepared at high Fe content for all cations except calcium, but they can only be prepared at low Fe content when using magnesium.

Finally, in SECTION 3: APPLICATIONS we first demonstrate a novel preparation method for colloidal protein-pyrophosphate composite systems in CHAPTER 7. We show that we are also able to incorporate nanoparticles of various other materials, and that the resulting $FePP_i$ -containing systems are stable for longer periods of time than a dispersion of $FePP_i$ itself. In the final chapter (CHAPTER 8) we study the reactivity of the iron-containing materials prepared throughout this work by using a model system for foodstuffs. We find that preparing iron as an inorganic pyrophosphate salt decreases its reactivity compared to 'free' Fe^{3+} and that a layer of protein further protects the incorporated iron. For the mixed systems we surprisingly find that when there is more Fe than M^{II} present in the particle the reactivity is actually higher than that of pure $FePP_i$. However, when excess M^{II} is present the reactivity is completely inhibited.

1.5 REFERENCES

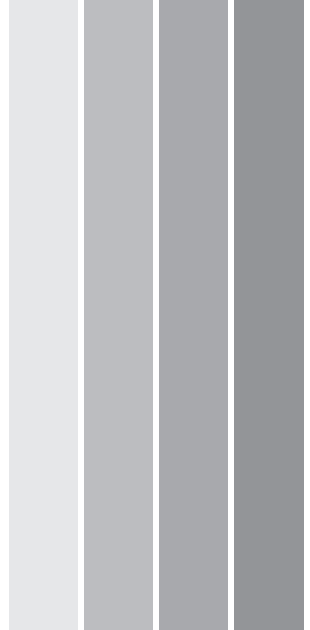
- [1] Acosta, E. Bioavailability of Nanoparticles in Nutrient and Nutraceutical Delivery. *Curr. Opin. Colloid In.* **2009**, *14*, 3-15.
- [2] Velikov, K. P.; Pelan, E. Colloidal Delivery Systems for Micronutrients and Nutraceuticals. *Soft Matter* **2008**, *4*, 1964-1980.
- [3] Mellican, R. I.; Li, J.; Nielsen, S. S. The Role of Iron and the Factors Affecting Off-Color Development of Polyphenols. *J. Agric. Food Chem.* **2003**, *51*, 2304-2316.
- [4] Wegmüller, R.; Zimmermann, M. B.; Hurrell, R. F. Particle Size Reduction and Encapsulation Affect the Bioavailability of Ferric Pyrophosphate in Rats. *J. Nutr.* **2004**, *134*, 3301-3304.
- [5] Rohner, F.; Ernst, F. O.; Zimmermann, M. B. Synthesis, Characterization, and Bioavailability in Rats of Ferric Phosphate Nanoparticles. *J. Nutr.* **2007**, *137*, 614-619.
- [6] Hilty, F. M.; Arnold, M.; Zimmermann, M. B. Iron from Nanocompounds Containing Iron and Zinc is Highly Bioavailable in Rats without Tissue Accumulation. *Nature Nanotechnology* **2010**, *5*, 374-380.
- [7] Mehansho, H.; Mellican, R. I.; Walter, T. Multiple-Micronutrient Fortification Technology Development and Evaluation: From Lab to Market. *Food Nutr. Bull.* **2003**, *24*, S111-S119.
- [8] Alberts, B.; Johnson, A.; Lewis, J., et al. In *Molecular Biology of the Cell*; Garland Science: New York, New York, 1983.
- [9] Hogfeldt, E. In *Stability constants of metal-ion complexes. (Special publication No. 17)*; The Chemical Society: London, 1964.
- [10] Sillen, L. G.; Martell, A. E. In *Stability constants of metal-ion complexes. (Special publication No. 25)*; The Chemical Society: London, 1970.
- [11] Sillen, L. G.; Martell, A. E. In *Stability constants of metal-ion complexes. (Special publication No. 17)*; The Chemical Society: London, 1964.
- [12] Shao, N.; Wang, H.; Chan, W. Spiropyran-Based Fluorescent Anion Probe and its Application for Urinary Pyrophosphate Detection. *Anal. Chem.* **2010**, *82*, 4628-4636.
- [13] Guo, Z.; Zhu, W.; Tian, H. Hydrophilic Copolymer Bearing Dicyanomethylene-4H-Pyran Moiety as Fluorescent Film Sensor for Cu and Pyrophosphate Anion. *Macromolecules* **2010**, *43*, 739-744.
- [14] Belkouch, J.; Monceaux, L.; Courtine, P. Comparative Structural Study of Mixed Metals Pyrophosphates. *Mater. Res. Bull.* **1995**, *30*, 149-160.
- [15] Belkouch, J.; Taouk, B.; Hecquet, G. Cesium Promotion of Iron Phosphate Catalyst and Influence of Steam on the Oxidative Dehydrogenation of Isobutyric Acid to Methacrylic Acid. *Stud. Surf. Sci. Catal.* **1994**, *82*, 819-828.
- [16] Millet, J. M. M.; Vedin, J. C. Role of Cesium in Iron Phosphates used in Isobutyric Acid Oxidative Dehydrogenation. *Appl. Catal.* **1991**, *76*, 209-219.
- [17] Hutchings, G. J. Effect of Promoters and Reactant Concentration on the Selective Oxidation of N-Butane to Maleic Anhydride using Vanadium Phosphorus Oxide Catalysts. *Appl. Catal.* **1991**, *72*, 1-32.
- [18] Morozova, N. Y.; Selivanova, N. Y. The $K_4P_2O_7$ - $Zn_2P_2O_7$ - H_2O System at 25°C. *Russ. J. Inorg. Chem.* **1976**, *21*, 878-879.
- [19] Ait Salah, A.; Jozwiak, P.; Julien, C. M. FTIR Features of Lithium-Iron Phosphates as Electrode Materials for Rechargeable Lithium Batteries. *Spectrochim. Acta A* **2006**, *65*, 1007-1013.
- [20] Barpanda, P.; Ye, T.; Yamada, A. Sodium Iron Pyrophosphate: A Novel 3.0V Iron-Based Cathode for Sodium-Ion Batteries. *Electrochem. Commun.* **2012**, *24*, 116-119.

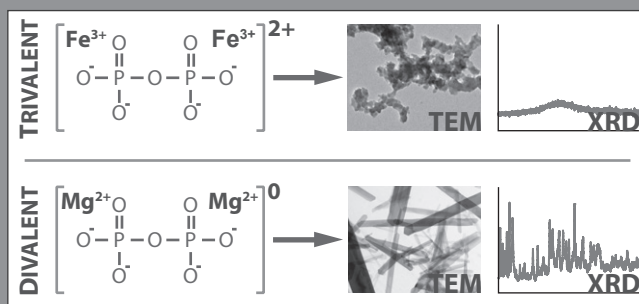
- [21] Kim, H.; Shakoor, R. A.; Choi, J. W. $\text{Na}_2\text{FeP}_2\text{O}_7$ as a Promising Iron-Based Pyrophosphate Cathode for Sodium Rechargeable Batteries: A Combined Experimental and Theoretical Study. *Adv. Funct. Mater.* **2012**, DOI: 10.1002/adfm.201201589.
- [22] Ray, C. S.; Fang, X.; Day, D. E. Effect of Melting Temperature and Time on Iron Valence and Crystallization of Iron Phosphate Glasses. *J. Non Cryst. Solids* **1999**, *249*, 1-16.
- [23] Gbureck, U.; Hölzel, T.; Grover, L. M. Preparation of Tricalcium Phosphate/Calcium Pyrophosphate Structures Via Rapid Prototyping. *J. Mater. Sci.: Mater. Med.* **2008**, *19*, 1559-1563.
- [24] Doat, A.; Pellé, F.; Lebugle, A. Europium-Doped Calcium Pyrophosphates: Allotropic Forms and Photoluminescent Properties. *J. Solid State Chem.* **2005**, *178*, 2354-2362.
- [25] Groves, P. J.; Wilson, R. M.; Shellis, R. P. Synthesis of Triclinic Calcium Pyrophosphate Crystals. *J. Mater. Sci. Mater. Med.* **2007**, *18*, 1355-1360.
- [26] Mandel, G. S.; Halverson, P. B.; Mandel, N. S. Calcium Pyrophosphate Crystal Deposition: The Effect of Soluble Iron in a Kinetic Study using a Gelatin Matrix Model. *Scanning Microsc.* **1988**, *2*, 1177-1188.
- [27] Sakaguchi, N.; Theertham, P. R.; Juneja, L. R. Iron Absorption and Bioavailability in Rats of Micronized Dispersible Ferric Pyrophosphate. *Int. J. Vitam. Nutr. Res.* **2004**, *74*, 3-9.
- [28] Fidler, M. C.; Walczyk, T.; Hurrell, R. F. A Micronised, Dispersible Ferric Pyrophosphate with High Relative Bioavailability in Man. *Br. J. Nutr.* **2004**, *91*, 107-112.
- [29] Everett, D. H. In *Basic Principles of Colloid Science*; The Royal Society of Chemistry: 1988.
- [30] Oberdörster, G.; Oberdörster, E.; Oberdörster, J. Nanotoxicology: An Emerging Discipline Evolving from Studies of Ultrafine Particles. *Environ. Health Perspect.* **2005**, *113*, 823-839.
- [31] Chau, C. F.; Wu, S. H.; Yen, G. C. The Development of Regulations for Food Nanotechnology. *Trends in Food Science and Technology* **2007**, *18*, 269-280.
- [32] Verwey, E. J. W.; Overbeek, J. T. G. In *Theory of the Stability of Lyophobic Colloids*; Dover Publications, Inc.: 1999.
- [33] Israelachvili, J. N. In *Intermolecular & Surface Forces*; Academic Press, Inc.: 1985.
- [34] Hamaker, H. C. The London-Van Der Waals Attraction between Spherical Particles. *Physica* **1937**, *4*, 1058-1072.
- [35] Overbeek, J. T. G. Strong and Weak Points in the Interpretation of Colloid Stability. *Adv. Colloid Interface Sci.* **1982**, *16*, 17-30.
- [36] Frens, G.; Overbeek, J. T. G. Repeptization and the Theory of Electrocratic Colloids. *J. Colloid Interface Sci.* **1972**, *38*, 376-387.
- [37] Overbeek, J. T. G. Recent Developments in the Understanding of Colloid Stability. *J. Colloid Interface Sci.* **1977**, *58*, 408-422.
- [38] Frens, G. On Coagulation in the Primary Minimum. *Faraday Discuss. Chem. Soc.* **1978**, *65*, 146-155.
- [39] Hunter, R. J. In *Foundations of Colloid Science*; Oxford University Press: 2001.
- [40] O'Brien, R. W.; White, L. R. Electrophoretic Mobility of a Spherical Colloidal Particle. *J. Chem. Soc., Faraday Trans. 2* **1978**, *74*, 1607-1626.
- [41] Lyklema, J.; Van Leeuwen, H. P.; Minor, M. DLVO-Theory, a Dynamic Re-Interpretation. *Adv. Colloid Interface Sci.* **1999**, *83*, 33-69.
- [42] Hunter, R. J. In *Zeta potential in colloid science: principles and applications*; Academic Press: London, 1981

SECTION 1

MORPHOLOGY OF COLLOIDAL METAL PYROPHOSPHATE SALTS

PREPARATION OF COLLOIDAL MI-PYROPHOSPHATE SALTS
PREPARATION





CHAPTER 2

MORPHOLOGY OF COLLOIDAL METAL PYROPHOSPHATE SALTS

We report the preparation and characterization of colloidal particles of several metal pyrophosphate salts. The materials are compared in order to determine the influence of the composition and experimental conditions on particle morphology. From this we make two observations. First, the metal ion valence determines the degree of crystallinity of the material: while the trivalent metal ions lead to amorphous precipitates, the divalent ones result in crystalline nanoparticles. Furthermore, the nature of the metal ion has a significant influence on the morphology of the crystalline particles as we find clear shape preference for each metal ion. Second, methods such as autoclave treatment and surfactant addition can be used to further change particle morphology.

2.1 INTRODUCTION

As mentioned in CHAPTER 1, the main goal of this thesis is to prepare colloidal particles of metal pyrophosphates salts in order to reduce the reactivity of the contained minerals compared to 'free' ions in solution. Metal pyrophosphate salts are currently mainly prepared by solid state synthesis at high temperatures [1-8], although a more gentle 'wet chemistry' method is sometimes used as well [9, 10]. However, these methods lack control over the morphology of the resulting particles while this is crucial for many of the biological and food applications as health risks can be induced by particle size and shape, asbestos being a notorious example.

In this chapter we present a systematic overview of the colloidal metal pyrophosphate salts prepared by a coprecipitation method. We study the influence of the valence and nature of the metal ion on the morphology of the resulting materials. The cations used were Ca^{2+} , Mg^{2+} , Zn^{2+} , Fe^{3+} , Al^{3+} : iron(III) and the divalent metals were chosen considering biocompatibility, aluminium was used as another trivalent cation. We show that particle morphology is very diverse and depends on the metal ion as well as the preparation method. The coprecipitation method was also modified in three ways:

1. By autoclave treatment, which is used in literature for changing gel-like materials into crystalline particles [11-13].

2. By ultrasonic treatment during or after precipitation, which can help prevent aggregation during the growth of the particles that are formed [14]

3. By the addition of surfactant molecules during preparation, as this can have strong effects on particle morphology [15, 16]. Three types of surfactant were used: anionic (SDS), cationic (CTAB) and nonionic (NP-5), see FIGURE 2.1.

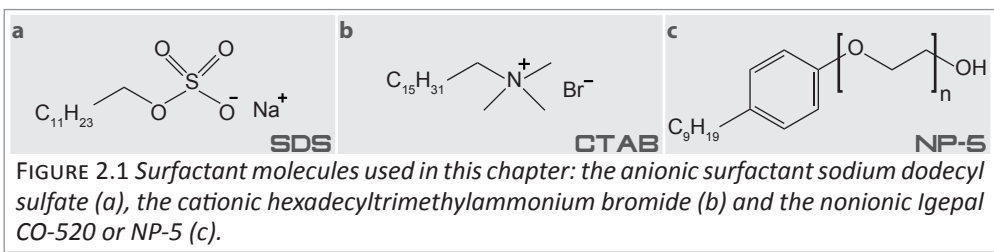
2.2 EXPERIMENTAL SECTION

2.2.I MATERIALS

$\text{FeCl}_3 \cdot 6\text{H}_2\text{O}$, $\text{CaCl}_2 \cdot 2\text{H}_2\text{O}$, $\text{AlCl}_3 \cdot 6\text{H}_2\text{O}$, sodium dodecyl sulphate (SDS), hexadecyltrimethylammonium bromide (CTAB), Igepal CO-520 (NP-5) and disodium ethylenediamine-tetraacetic acid dihydrate (Na_2EDTA) were all obtained from Sigma Aldrich. $\text{Na}_4\text{P}_2\text{O}_7 \cdot 10\text{H}_2\text{O}$ and $\text{Zn}(\text{NO}_3)_2 \cdot 4\text{H}_2\text{O}$ were bought from Merck and $\text{MgCl}_2 \cdot 6\text{H}_2\text{O}$ from Fluka. All chemicals were used as received; aqueous solutions were prepared using water deionized by a Millipore Synergy water purification system.

2.2.II PREPARATION

Colloidal particles of iron pyrophosphate were prepared by dissolving 0.857 mmol FeCl_3 in 50 ml water and adding this solution dropwise in about 15 minutes to 0.643 mmol $\text{Na}_4\text{P}_2\text{O}_7$ in 100 ml while stirring. A turbid white dispersion forms during the addition of the final 5 ml iron(III) solution. For some experiments, the addition was performed in an ultrasonic bath. These dispersions were stirred for another 30 minutes while ultrasonating



after complete addition. For autoclave experiments, after complete addition the reaction mixture was transferred to a Teflon holder in a steel autoclave cylinder and stored at 100 °C for four days without stirring. All reaction mixtures were cleaned after preparation by centrifugation and washing with millipore water twice.

The influence of surfactants was investigated as well. For these experiments surfactant (anionic SDS, cationic CTAB or non-ionic NP-5) was used in a four times excess to the pyrophosphate concentration; 2.6 mmol of the surfactant was dissolved in the pyrophosphate solution before adding the metal ion solution. This resulted in a concentration of 17 mM in the final volume: beyond the critical micelle concentration (cmc) for all surfactants. These samples were centrifuged five times instead of two to remove excess surfactant.

Alternative preparation methods that were investigated are discussed in APPENDIX I.

2.2.III ANALYSIS

Dynamic Light Scattering (DLS) measurements were performed on a Malvern Instruments Zetasizer Nano series machine in backscatter mode at 25°C with 5 minutes of equilibration time. Samples were dried on a carbon-coated copper grid prior to transmission electron microscopy (TEM) and Energy-dispersive X-ray spectroscopy (EDX) performed on a Tecnai 12 and Tecnai 20 from FEI Company, respectively. Samples for material analysis using X-ray powder diffraction (XRD) and Fourier transform Infrared spectroscopy (FTIR) were prepared by centrifuging the dispersion again, washing the sediment three times with acetone and drying in an oven at 40 degrees for 24 hours. FTIR spectra were measured on a Perkin-Elmer IR spectrometer using the KBr pellet technique, XRD measurements were carried out on a Bruker-AXS D8 Advance powder X-ray diffractometer in Bragg-Brentano mode equipped with automatic divergence slit (0.6 mm 0.3°) and a PSD Vântec-1 detector. The radiation used was Cobalt $K\alpha_{1,2}$, $\lambda = 1.79026 \text{ \AA}$, operated at 30kV, 45 mA. Elemental analysis using inductively coupled plasma atomic emission spectroscopy (ICP-AES) was performed on a solution prepared by dissolving the dried samples using a four times excess of Na_2EDTA compared to the (estimated) metal ion content. Measurements performed using a SPECTRO CIROSCCD ICP (8.13) with a radial plasma ion source and Paschen-Runge spectrometer.

2.3 RESULTS

2.3.I METAL PYROPHOSPHATE MORPHOLOGY

Comparing the influence of divalent and trivalent metal ions we find that the precipitation method yields similar particles for aluminum, iron and calcium pyrophosphates. TEM analysis shows clusters consisting of primary particles of roughly 20 nm, see FIGURE 2.2a-c. Magnesium and zinc show different morphology: magnesium pyrophosphate forms large micrometer-sized needles and spheres (FIGURE 2.2d), while zinc results in thin platelets with either sharp or rounded corners, see FIGURE 2.2e. As it is generally known from colloidal synthesis that the preparation method can have a drastic influence on the morphology of the resulting particles, we tested three frequently used methods for their influence on metal pyrophosphates.

First, autoclave treatment has a strong influence on metal pyrophosphate morphology. For the trivalent materials the primary particles have become hollow, see FIGURE 2.2f and g. We were unable to take high resolution images of these hollow particles during TEM analysis because these seem to be much more beam sensitive than the untreated particles

shown in FIGURE 2.2a and b. Even at low-dose illumination the particles shrink within seconds and the hollow center is no longer visible. CaPP_i grows into rods resembling those found from similar treatment of the chemically related hydroxyapatite [17], FIGURE 2.2h. The size of these rods can be slightly influenced by the autoclave temperature and treatment time (results not shown). MgPP_i forms micrometer sized, ellipsoidal platelets and autoclave treatment of the ZnPP_i particles results in thicker, rounded platelets, see FIGURE 2.2i and j.

In the second method, ultrasonication of the dispersions during and/or after preparation does not have a significant influence on particle shape on any material but CaPP_i . This system changes into micrometer sized, crystalline platelets, see FIGURE 2.2k.

With the third method, surfactant addition, we find that while surfactants have no discernable influence on FePP_i and AlPP_i , it does change the morphology of the $\text{M}^{\text{II}}\text{PP}_i$ s. The results are summarized in the image-matrix in FIGURE 2.3. Two samples are missing from the matrix: Ca^{2+} forms a precipitate with SDS and therefore CaPP_i could not be prepared with SDS. This effect is not observed for any of the other metal ions used in this work. Using CTAB in the reaction mixture of MgPP_i results in a clear solution: no particles are formed.

For SDS, magnesium forms very thin, elongated platelets (FIGURE 2.3a) while zinc only forms the geometric shapes found in FIGURE 2.2e (FIGURE 2.3b). CaPP_i in the presence of CTAB forms large spherical clusters of platelets and ZnPP_i results in ellipsoidal platelets of around $3 \mu\text{m}$ that consist of multiple layers as shown in FIGURE 2.3c and d. Finally, CaPP_i grown in presence of NP-5 shows morphology similar to CTAB treatment but consisting of thinner platelets with frayed edges as shown in FIGURE 2.3e. MgPP_i shows particles smaller but similar to those formed with regular synthesis, ZnPP_i yields platelets with truncated corners when prepared with NP-5 (see FIGURE 2.3f and g).

Comparing these results we find that $\text{M}^{\text{II}}\text{PP}_i$ s form amorphous precipitates while $\text{M}^{\text{III}}\text{PP}_i$ s form different, possibly crystalline, shapes. MgPP_i preferably forms elongated, needle-

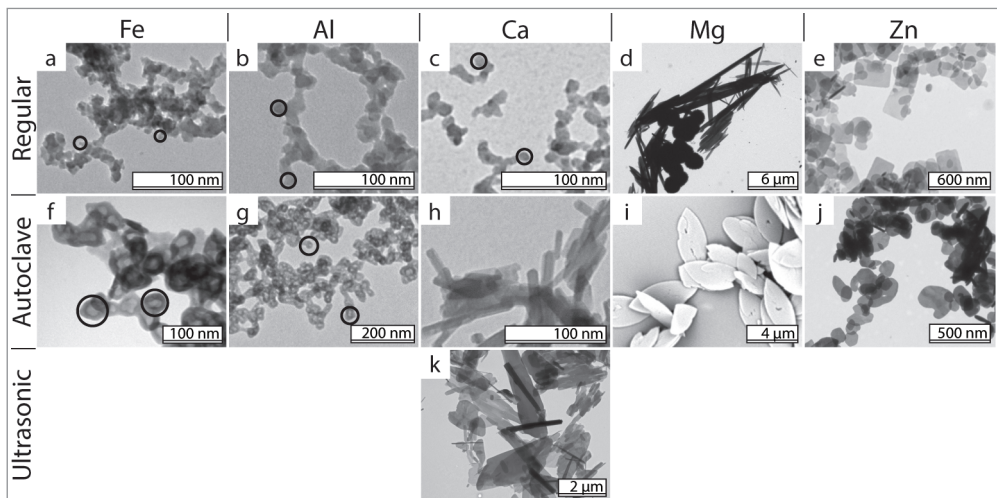


FIGURE 2.2 TEM image matrix summarizing the influence of preparation method and metal ion on colloidal MPP_i s. Rows indicate the preparation method, columns the metal ion used. The circles indicate what we refer to as the primary particles in the amorphous aggregates. Figure i is a SEM image.

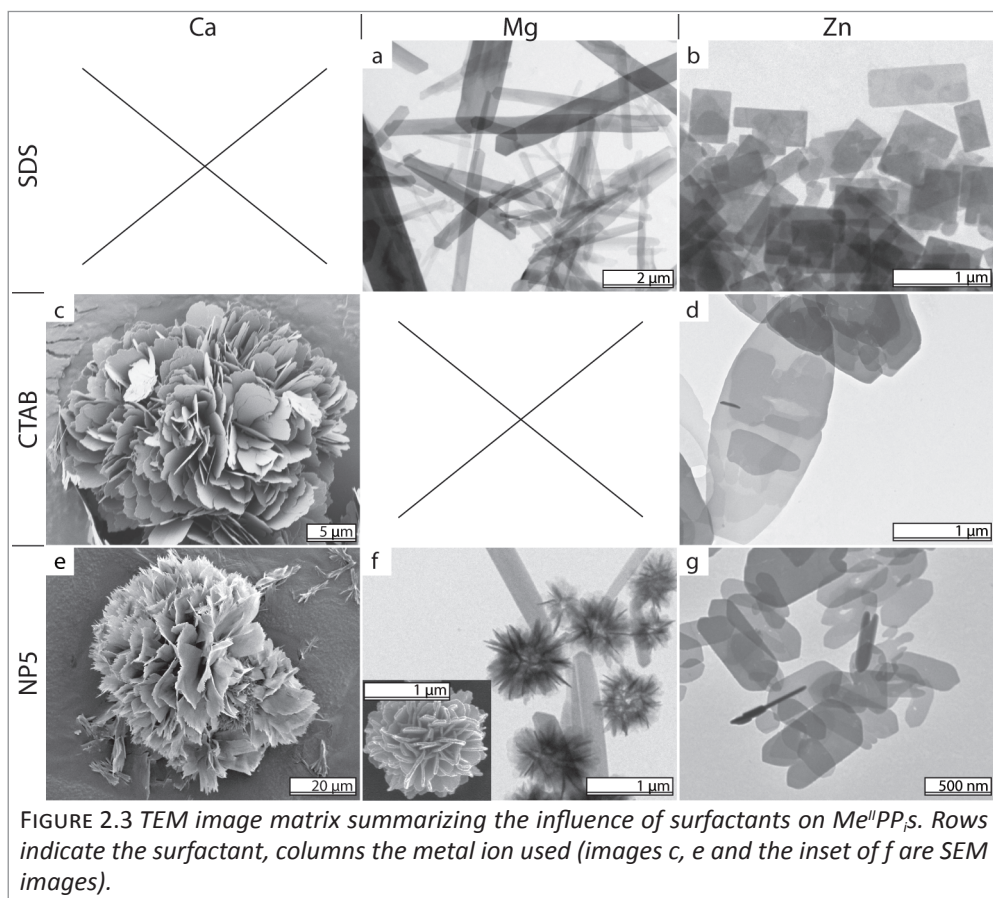


FIGURE 2.3 TEM image matrix summarizing the influence of surfactants on $Me^II PP_i$ s. Rows indicate the surfactant, columns the metal ion used (images c, e and the inset of f are SEM images).

like particles. The spheres shown in FIGURE 2.2d seem to be an exception to this, but they actually consist of platelets and needles clustered together, just like the particles shown in the inset of FIGURE 2.3f. $ZnPP_i$ has a clear preference for thin platelets and $CaPP_i$ morphology differs per preparation method. In general, the $M^II PP_i$ s have a preference for thin platelets or needles.

DLS analysis of $FePP_i$ yields sizes on the order of 200 nm, which is larger than the particles found from TEM (~ 20 nm). This indicates that the precipitates formed are present as clusters in dispersion, possibly resembling what is found from TEM analysis (FIGURE 2.2a and b). It should be noted here that aggregates observed from TEM are not necessarily representative for the situation in dispersion, as TEM samples are dried prior to analysis. DLS analysis of $AlPP_i$ and the $M^II PP_i$ s was not successful due to colloidal instability. The fact that DLS analysis on $MgPP_i$ and $ZnPP_i$ would not be possible could have been expected from TEM analysis: micrometer sized (aggregated) particles of these materials will sediment rapidly. However, while $AlPP_i$ and $CaPP_i$ look morphologically similar to $FePP_i$ in TEM images (FIGURE 2.2a, b and c), sedimentation was fast in these samples as well. From this it might be concluded that much larger aggregates are formed in $AlPP_i$ and $CaPP_i$ compared to $FePP_i$. This is confirmed by the macroscopic observation of the $AlPP_i$ and $CaPP_i$ dispersions sedimenting significantly faster than the $FePP_i$ dispersion (see FIGURE 2.4). This behaviour could not be influenced by ultrasonication during or after preparation.

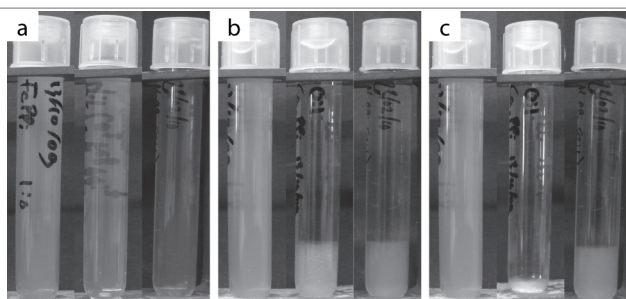


FIGURE 2.4 Sedimentation in three metal pyrophosphate dispersions over time: freshly prepared (a), after 24 hours (b) and after three days (c). From left to right: FePP_i , CaPP_i , and AlPP_i . After three days de gel-like state formed in (b) has collapsed completely into dense aggregates for CaPP_i .

We have also attempted other variations on the preparation method such as varying the speed or order of addition, but we have found no significant influence on the morphology of the resulting particles, see APPENDIX IA.

XRD analysis confirms the difference between $\text{M}^{\text{II}}\text{PP}_i$ and $\text{M}^{\text{III}}\text{PP}_i$ found from TEM analysis in FIGURE 2.2 and FIGURE 2.3. While the XRD spectra for both $\text{M}^{\text{III}}\text{PP}_i$ s show only noise indicating amorphous materials, the spectra for $\text{M}^{\text{II}}\text{PP}_i$ s show clear signals, see FIGURE 2.5a. However, the high signal-to-noise ratio indicates that part of the $\text{M}^{\text{II}}\text{PP}_i$ particles is amorphous as well. The influence of the preparation method is also visible in XRD analysis. For example, autoclave treatment of calcium pyrophosphate increases crystallinity and changes its crystal structure as can be seen from the reduction in background noise and shift in peak location in FIGURE 2.5b, comparing the spectra of CaPP_i before (yellow, bottom) and after autoclave treatment (orange, middle). Similar effects have been shown in literature for solid-state preparation methods at much higher temperatures [5, 7, 18]. Ultrasonication also changes the XRD spectrum of CaPP_i , see the red top spectrum in FIGURE 2.5b. Magnesium shows similar changes and the presence of SDS slightly influences the obtained pattern but not as drastic as the change in preparation method, see FIGURE 2.5c. Comparison of these XRD spectra with literature yields little to no agreement. This could be explained by the fact that, as mentioned before, most of those characterizations are performed on macroscopic crystals obtained from solid-state preparation often at high temperatures likely to induce different crystal structures [6-8, 10, 19-21].

FTIR analysis shows that peak positions coincide between materials due to the fact that the main vibrationally active species is the same in all materials (PP_i), see FIGURE 2.6. The one exception to this is AlPP_i , for which the spectrum is slightly shifted: e.g. the maximum at 1120 cm^{-1} shifts to 1170 cm^{-1} . This could indicate a stronger influence of Al^{3+} on the $\text{P}=\text{O}$ vibration compared to the other metal ions, but why a similar effect is not observed for Fe^{3+} is not clear.

$\text{M}^{\text{III}}\text{PP}_i$ s show broad, smooth peaks in FTIR analysis, while $\text{M}^{\text{II}}\text{PP}_i$ s result in sharper peaks. This is probably due to the partly amorphous nature of the $\text{M}^{\text{III}}\text{PP}_i$ s found from XRD analysis in FIGURE 2.5. This lower degree of crystallinity also explains the poor agreement in detail with FTIR analysis of crystalline (bulk) materials reported in literature, such as LiFePP_i [9] or CaPP_i [6, 22, 23]. More amorphous materials such as CoFePP_i give better agreement in the smoothness of the curves [1].

From ICP-AES elemental analysis we find that the particle composition is very similar

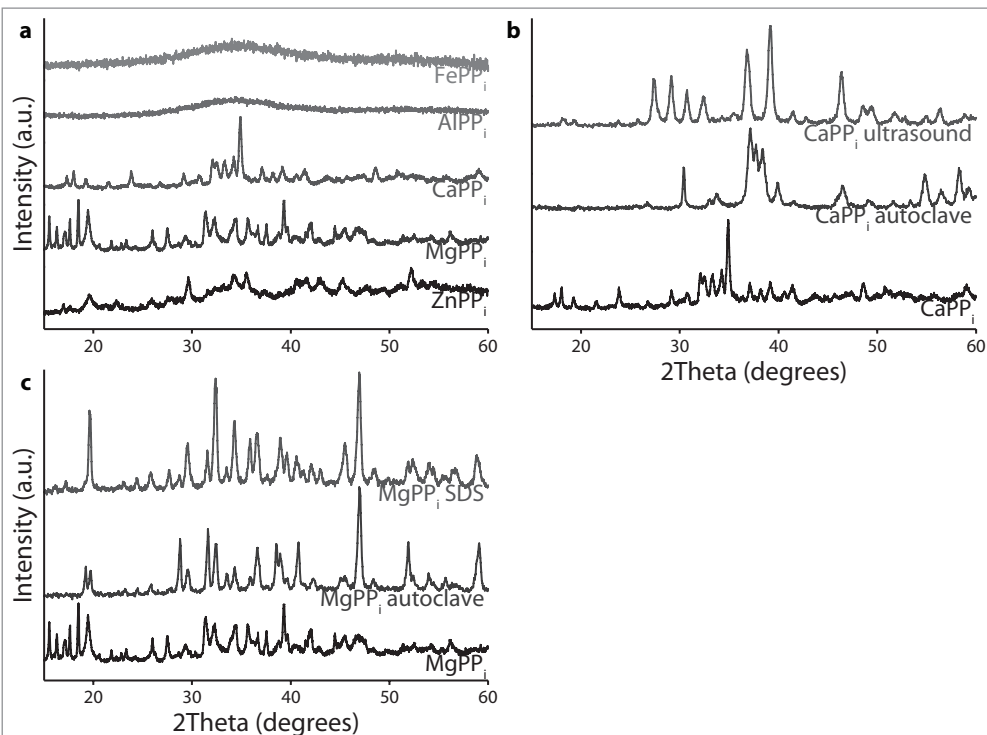


FIGURE 2.5 XRD analysis of the metal pyrophosphates. Comparison between $M^{II}PP_i$ and $M^{III}PP_i$ in (a) shows the $M^{III}PP_i$ s to be amorphous while the $M^{II}PP_i$ s are (partly) crystalline. Using different preparation methods such as addition of surfactant, ultrasonication or autoclave treatment results in different crystal structures for $CaPP_i$ (b) and $MgPP_i$ (c).

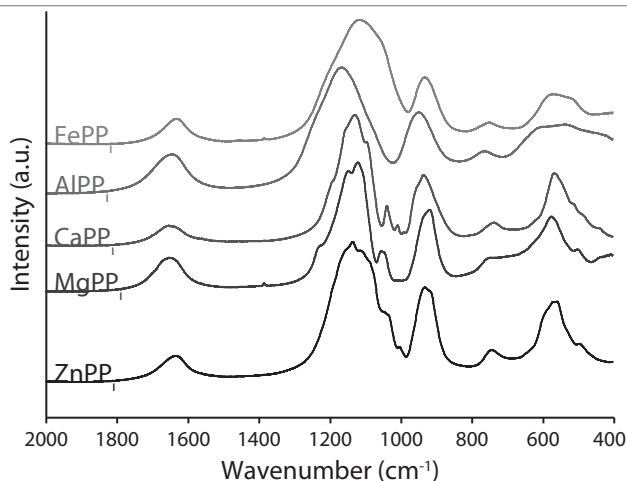
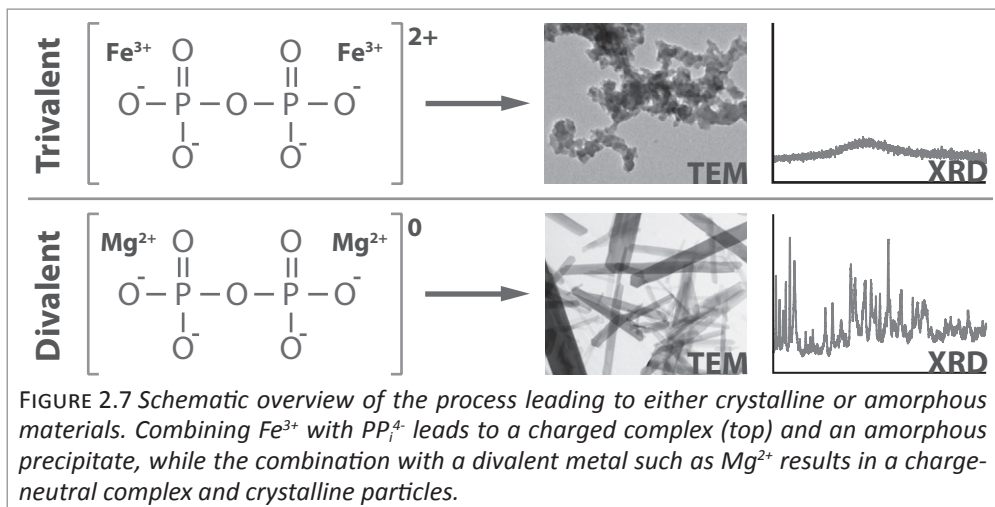


FIGURE 2.6 FTIR analysis of the metal pyrophosphates prepared by coprecipitation. At wavenumbers beyond 2000 cm^{-1} only a broad $-OH$ peak is found (not shown).



to what is added during reaction, except for the Na^+ and Cl^- which are predominantly left in solution. For FePP_i particles this results in $\text{Na}_{0.2}\text{Cl}_{0.3}\text{Fe}_4(\text{P}_2\text{O}_7)_{2.9}$, compared to the $\text{Na}_{12}\text{Cl}_{12}\text{Fe}_4(\text{P}_2\text{O}_7)_3$ added. Most likely the Na and Cl indicated in the formula of the precipitate are largely present as counterions in solution not washed away during cleaning of the reaction mixture, not so much incorporated into the material.

We have shown that the degree of crystallinity of the colloidal particles is determined by the valence of the metal ion used as we find the $\text{M}^{\text{III}}\text{PP}_i$ s to be amorphous and the $\text{M}^{\text{II}}\text{PP}_i$ s to be mostly crystalline. It can be argued that this is caused by the 'valence mismatch' in $\text{M}^{\text{III}}\text{PP}_i$ s. While $\text{M}^{\text{II}}\text{PP}_i$ can easily form a charge-neutral Me_2PP_i unit for (bulk) crystalline material, the combination of M^{3+} and PP_i^{4-} needs a more complicated stoichiometry to reach charge neutrality. During fast precipitation this could result in an amorphous structure, see FIGURE 2.7. It is therefore slightly surprising to find so little Na^+ or Cl^- in the chemical analysis as both could help in forming smaller charge-neutral subunits. Similar complicating effects could cause CaPP_i to initially form amorphous material if the Ca- PP_i bond is so strong that amorphous precipitation is faster than crystallization.

It is interesting to note that the chemically related metal phosphate salts seem to follow the opposite trend in valence dependent crystallinity, as colloidal aluminum phosphate (vascerite) is crystalline [24] while phosphates containing divalent metals can be prepared as amorphous particles even after autoclave treatment [25, 26]. This might be caused by the same effect mentioned above: as the phosphate ion is trivalent, the divalent metals would have the 'valence mismatch' and the trivalent metals can immediately form a charge neutral complex. That iron phosphate forms micrometer-sized, amorphous particles [27] could be caused by a similar effect as mentioned for calcium pyrophosphate.

2.4 CONCLUSIONS

In this work we have studied the morphology of metal pyrophosphate salts. First, we have shown the influence of the metal ion valence on the morphology of metal pyrophosphates; while the trivalent metal ions yield amorphous precipitates, the divalent ones result in crystalline particles. Furthermore, the type of divalent metal ion determines the shape of the particles formed as we find different particles for the different metal ions. Second, we have shown that the morphology of these materials can be further modified

by changes in experimental conditions by using methods such as autoclave treatment or addition of surfactants. In general, $M^{II}PP_i$ s have a preference for thin, flat platelets or needles differing in size or shape per preparation method, while the $M^{III}PP_i$ s form the same amorphous nanoparticles for every preparation method. The only exception is autoclave treatment: amorphous metal pyrophosphates aged at elevated temperatures slightly increase in size and become hollow. They do not form the crystalline particles one might expect from other work [11-13]. Analysis using XRD shows that these changes in shape coincide with different crystal structures, but no exact match is found with materials in literature.

ICP-AES analysis indicates overall particle composition to be consistent with what was added during preparation. The difference in crystallinity between $M^{II}PP_i$ and $M^{III}PP_i$ might be caused by the greater complexity needed for forming an uncharged unit of $M^{III}PP_i$ compared to $M^{II}PP_i$, thereby preferring an amorphous structure upon fast precipitation.

2.5 ACKNOWLEDGEMENTS

We thank the following people for characterization and analysis: F. Soulimani and M. Versluijs-Helder of the Inorganic Chemistry and Catalysis group at the University of Utrecht for FTIR and XRD measurements, respectively. J.D. Meeldijk of the Electron Microscopy group in Utrecht is thanked for SEM analysis and H.C. de Waard of the Geolab Analytical services in Utrecht for ICP-AES measurements.

Reprinted from: Y.M. van Leeuwen, K.P. Velikov and W.K. Kegel, *RSC Advances*, **2012**, 2, 2534-2540 - Reproduced by permission of The Royal Society of Chemistry

2.6 REFERENCES

- [1] Boonchom, B.; Phuvongpha, N. Synthesis of New Binary Cobalt Iron Pyrophosphate $CoFeP_2O_7$. *Mater. Lett.* **2009**, 63, 1709-1711.
- [2] Hutchings, G. J. Effect of Promoters and Reactant Concentration on the Selective Oxidation of N-Butane to Maleic Anhydride using Vanadium Phosphorus Oxide Catalysts. *Appl. Catal.* **1991**, 72, 1-32.
- [3] Gbureck, U.; Hölzel, T.; Grover, L. M. Preparation of Tricalcium Phosphate/Calcium Pyrophosphate Structures Via Rapid Prototyping. *J. Mater. Sci.: Mater. Med.* **2008**, 19, 1559-1563.
- [4] Doat, A.; Pellé, F.; Lebugle, A. Europium-Doped Calcium Pyrophosphates: Allotropic Forms and Photoluminescent Properties. *J. Solid State Chem.* **2005**, 178, 2354-2362.
- [5] Bian, J.; Kim, D.; Hong, K. Phase Transformation and Sintering Behavior of $Ca_2P_2O_7$. *Mater Lett* **2004**, 58, 347-351.
- [6] El Kady, A. M.; Mohamed, K. R.; El-Bassyouni, G. T. Fabrication, Characterization and Bioactivity Evaluation of Calcium Pyrophosphate/Polymeric Biocomposites. *Ceram. Int.* **2009**, 35, 2933-2942.
- [7] Xiao, Z. W.; Hu, G. R.; Gao, X. G. Solid State Synthesis and Characterization of Iron(II) Pyrophosphate $Fe_2P_2O_7$. *Chinese Chem. Lett.* **2007**, 18, 1525-1527.
- [8] Pang, R.; Li, C.; Su, Q. Luminescent Properties of a New Blue Long-Lasting Phosphor $Ca_2P_2O_7:Eu^{2+}, Y^{3+}$. *Mater. Chem. Phys.* **2009**, 113, 215-218.
- [9] Ait Salah, A.; Jozwiak, P.; Julien, C. M. FTIR Features of Lithium-Iron Phosphates as Electrode Materials for Rechargeable Lithium Batteries. *Spectrochim. Acta A* **2006**, 65, 1007-1013.
- [10] Belkouch, J.; Monceaux, L.; Courtine, P. Comparative Structural Study of Mixed Metals

- Pyrophosphates. *Mater. Res. Bull.* **1995**, *30*, 149-160.
- [11] Shen, S.; Chow, P. S.; Tan, R. B. H. Synthesis of Submicron Gibbsite Platelets by Organic-Free Hydrothermal Crystallization Process. *J. Cryst. Growth* **2006**, *292*, 136-142.
- [12] Hickey, L.; Klopogge, J. T.; Frost, R. L. Effects of various Hydrothermal Treatments on Magnesium-Aluminum Hydrotalcites. *J. Mater. Sci.* **2000**, *35*, 4347-4355.
- [13] Lagaly, G.; Mecking, O.; Penner, D. Colloidal Magnesium Aluminum Hydroxide and Heterocoagulation with a Clay Mineral. II. Heterocoagulation with Sodium Montmorillonite. *Colloid Polym. Sci.* **2001**, *279*, 1097-1103.
- [14] Claesson, E. M.; Philipse, A. P. Monodisperse Magnetizable Composite Silica Spheres with Tunable Dipolar Interactions. *Langmuir* **2005**, *21*, 9412-9419.
- [15] Nikoobakht, B.; El-Sayed, M. A. Preparation and Growth Mechanism of Gold Nanorods (NRs) using Seed-Mediated Growth Method. *Chem. Mater.* **2003**, *15*, 1957-1962.
- [16] Manna, L.; Scher, E. C.; Alivisatos, A. P. Synthesis of Soluble and Processable Rod-, Arrow-, Teardrop-, and Tetrapod-Shaped CdSe Nanocrystals. *J. Am. Chem. Soc.* **2000**, *122*, 12700-12706.
- [17] Riman, R. E.; Suchanek, W. L.; Oakes, C. S. Solution Synthesis of Hydroxyapatite Designer Particulates. *Solid State Ionics* **2002**, *151*, 393-402.
- [18] Ciopec, M.; Muntean, C.; Barvinschi, P. Synthesis and Thermal Behavior of Double Copper and Potassium Pyrophosphate. *Thermochimica Acta* **2009**, *488*, 10-16.
- [19] Elbouaanani, L. K.; Malaman, B.; Ijjaali, M. Crystal Structure Refinement and Magnetic Properties of $\text{Fe}_4(\text{P}_2\text{O}_7)_3$ Studied by Neutron Diffraction and Mössbauer Techniques. *J. Solid State Chem.* **2002**, *163*, 412-420.
- [20] Bian, J.; Kim, D.; Hong, K. Microwave Dielectric Properties of $(\text{Ca}_{1-x}\text{Zn}_x)_2\text{P}_2\text{O}_7$. *Mater Lett* **2005**, *59*, 257-260.
- [21] Boonchom, B.; Baitahe, R. Synthesis and Characterization of Nanocrystalline Manganese Pyrophosphate $\text{Mn}_2\text{P}_2\text{O}_7$. *Mater. Lett.* **2009**, *63*, 2218-2220.
- [22] Linstrom, P. J.; Mallard, W. G. Coblenz Society, Inc., "Evaluated Infrared Reference Spectra". *NIST Chemistry WebBook, NIST Standard Reference Database Number 69*.
- [23] Parekh, B. B.; Joshi, M. J. Growth and Characterization of Gel Grown Calcium Pyrophosphate Tetrahydrate Crystals. *Cryst. Res. Technol.* **2007**, *42*, 127-132.
- [24] Gómez Morales, J.; Rodríguez Clemente, R.; Matijević, E. The Mechanism of Precipitation of Colloidal Variscite ($\text{AlPO}_4 \cdot 2\text{H}_2\text{O}$) Particles. *J. Colloid Interface Sci.* **1992**, *151*, 555-562.
- [25] Springsteen, L. L.; Matijević, E. Preparation and Properties of Uniform Colloidal Metal Phosphates IV. Cadmium-, Nickel-, and Manganese(II)-Phosphates. *Colloid Polym. Sci.* **1989**, *267*, 1007-1015.
- [26] Ishikawa, T.; Matijević, E. Preparation and Properties of Uniform Colloidal Metal Phosphates. III. Cobalt(II) Phosphate. *J. Colloid Interface Sci.* **1988**, *123*, 122-128.
- [27] Wilhelmy, R. B.; Matijević, E. Preparation and Growth Kinetics of Monodispersed Ferric Phosphate Hydrosols. *Coll. Surf.* **1987**, *22*, 111-131.



CHAPTER 3

PREPARATION OF COLLOIDAL M^{II} -PYROPHOSPHATE SALTS

In this chapter we investigate several preparation methods that could lead to stable colloidal systems of pyrophosphate salts containing a divalent cation (calcium, magnesium or zinc, together referred to as M^{II}). These methods are based on a pH-dependent precipitation method that consists of two steps. In the first step M^{II} -pyrophosphate salt is coprecipitated and the counterions remaining in solution are removed. In the second step the material is redissolved in acid and the pH is subsequently raised again in one of two ways; either via the decomposition of urea or via the injection into alkaline media. We find that the urea decomposition method cannot be used to prepare stable dispersions as all systems settle within minutes to hours independent of further washing steps or addition of surfactants. For calcium and magnesium the instability is due to the large size of the resulting particles, but while zinc pyrophosphate does form small particles initially, these particles aggregate completely and no stable dispersions were obtained. The injection method yields stable dispersions when magnesium is used as the cation and no surfactants are added; the resulting dispersions of magnesium pyrophosphate are stable for months. Calcium and zinc pyrophosphates can be prepared as small particles with this method, but again these do not result in stable dispersions independent of system composition. The calcium pyrophosphate prepared with phosphocitrate shows some very interesting behaviour as the nanometer-sized particles that initially form and aggregate into larger clusters can be separated again by ultrasonication, but the resulting open structure is still connected by a thin, wire-like material.

3.1 INTRODUCTION

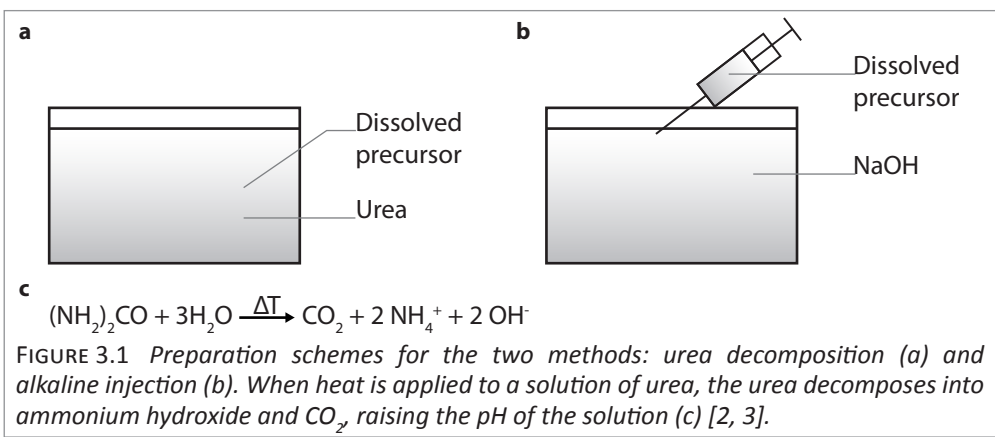
In CHAPTER 2 we have prepared metal pyrophosphate particles by coprecipitation of the precursor salts. While this method results in stable colloidal dispersions of iron pyrophosphate (FePP_i), we have shown that pyrophosphate coprecipitated with a divalent metal ($\text{M}^{\text{II}}\text{PP}_i$) in general forms particles that are too large to remain in suspension. Moreover, additional methods used for changing the morphology of colloids such as autoclave treatment or surfactant addition did not result in significantly smaller particles or stable dispersions. Because coprecipitation by slow addition is an ill-defined method of preparation (see APPENDIX IA for the influence of the order and rate of addition on the resulting particles), we attempt more controlled ways of preparing $\text{M}^{\text{II}}\text{PP}_i$ particles and try to influence their morphology in this chapter.

As $\text{M}^{\text{II}}\text{PP}_i$ s are soluble at low pH [1] we use a two-step preparation method in which the material is first coprecipitated, washed and dried and subsequently re-dissolved in acid. The pH of the solution is then raised again using one of two methods: urea decomposition or alkaline injection, see FIGURE 3.1 for details. The pH dependent solubility of metal pyrophosphate salts has been investigated in more detail as described in APPENDIX II

The urea decomposition method has previously been used by Groves *et al.* to prepare micrometer sized calcium pyrophosphate crystals [4]. As our goal is to prepare a dispersion of colloidal particles, we attempt to inhibit this growth by making use of organic (surfactant) molecules, either general or specific. Here the 'general' molecules are surfactants often used in colloidal synthesis such as the cationic CTAB, the anionic SDS and the nonionic NP-5 (also known as Igepal CO-520), see FIGURE 3.2a-c. By 'specific' molecules we refer to molecules that are not normally used as surfactants, but that are interesting candidates for inhibiting the crystal growth of MPP_i s. These inhibitors are adenosine 5'-triphosphate (ATP) and phosphocitrate (PC), see FIGURE 3.2d and e.

As explained in CHAPTER 1, PP_i is one of the possible hydrolysis products of ATP. By adding ATP to the growing particles, it is possible that the triphosphate group will be incorporated into the crystal while the large adenosine group blocks further growth of the particles.

Phosphocitrate is a well-studied molecule that is proposed as a strong inhibitor for the formation of calcium pyrophosphate [5-10], a common cause of arthritis [5, 6, 8]. As the morphology of CaPP_i is very diverse [11], using phosphocitrate to trap it into a specific crystalline state and inhibiting further growth might be way of preparing nanosized crystals.



3.2 METHODS

3.2.I MATERIALS

$\text{FeCl}_3 \cdot 6\text{H}_2\text{O}$, $\text{CaCl}_2 \cdot 2\text{H}_2\text{O}$, sodium dodecyl sulphate (SDS), hexadecyltrimethylammonium bromide (CTAB) and Igepal CO-520 (NP-5) were all obtained from Sigma Aldrich. $\text{Na}_4\text{P}_2\text{O}_7 \cdot 10\text{H}_2\text{O}$ and $\text{Zn}(\text{NO}_3)_2 \cdot 4\text{H}_2\text{O}$ were bought from Merck and $\text{MgCl}_2 \cdot 6\text{H}_2\text{O}$ from Fluka. Urea was obtained from Carl Roth GmbH and Adenosine 5'-triphosphate disodium from Brunschwig Chemie. All chemicals were used as received; aqueous solutions were prepared using water deionized by a Millipore Synergy water purification system.

3.2.II INTERMEDIATE

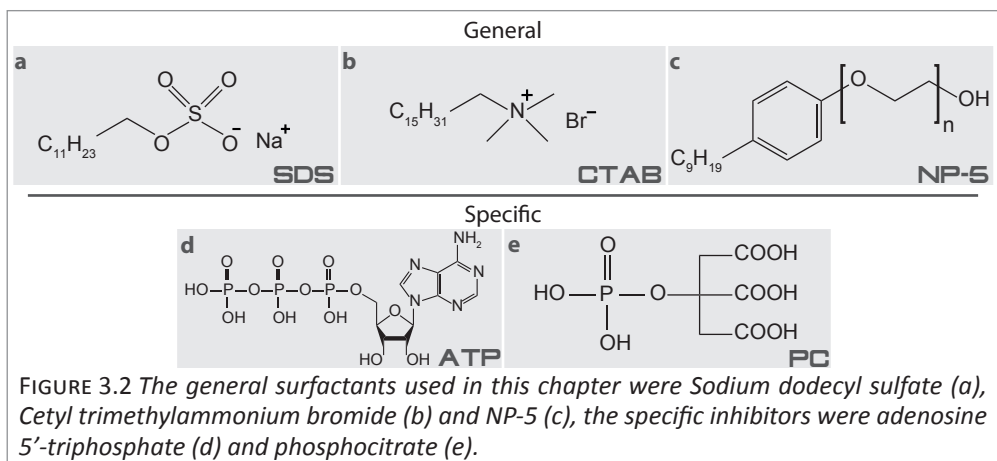
50 mL 1 M $\text{M}^{III}\text{Cl}_2$ solution was added drop wise in one hour to 800 mL 0.0625 M sodium pyrophosphate solution while stirring with a magnetic stirrer. Stirring was continued for another hour after complete addition. The resulting white suspension was washed by centrifugation three times with water and twice with acetone. Finally, the precipitate was dried in an oven at 37°C for 2 days.

3.2.III pH-DEPENDENT PRECIPITATION BY UREA DECOMPOSITION

0.56 grams of intermediate was dissolved in 15 mL 1 M HCl and filtered over a Minisart disposable cellulose acetate filter ($0.2\ \mu\text{m}$ pore size, 16534-K). Urea was added to result in a 1.0 M solution, heated to 90°C and kept at that temperature while stirring for 2-3 hours [4]. During this period the pH rose to 7, a white suspension started to form around pH 5. When the pH had reached 7 the solution was allowed to cool to room temperature and subsequently washed 3 times with water and redispersed in a final volume of 50 ml water. 5 mmol of the respective surfactant was added to the samples for the surfactant experiments before heating.

3.2.IV pH-DEPENDENT PRECIPITATION BY INJECTION IN ALKALINE MEDIA

0.56 grams of intermediate was dissolved in 15 mL 1 M HCl and filtered over a Minisart disposable cellulose acetate filter ($0.2\ \mu\text{m}$ pore size, 16534-K). The solution is injected into 35 mL 0.39 M NaOH solution while stirring vigorously using a magnetic stirrer. The turbid white dispersion was stirred for another 10 minutes after injection (final pH is 7).



The sample was washed twice by centrifugation and redispersed in a final volume of 50 mL water. 5 mmol of the respective surfactant was added to the NaOH solution before injection for the samples for the surfactant experiments.

3.2.V ORGANIC SYNTHESIS OF PHOSPHOCITRATE

As phosphocitrate was not commercially available at the time of writing, it was prepared following the work of Turhanen *et al.*: a six-step organic synthesis starting from the triethyl ester of citric acid and MeOPCl_2 [12]. Using this method we have successfully obtained the desired compound as confirmed by ^1H - and ^{31}P -NMR analysis (not shown).

3.2.VI ANALYSIS

Dynamic Light Scattering (DLS) measurements were performed on a Malvern Instruments Zetasizer Nano series machine in backscatter mode at 25°C with 5 minutes of equilibration time. Samples were dried on a carbon-coated copper grid prior to transmission electron microscopy (TEM) performed on a Tecnai 12 or scanning electron microscopy (SEM) using a Phenom scanning electron microscope, both from FEI Company.

3.3 RESULTS

3.3.I UREA METHOD

The urea-decomposition method did not result in stable dispersions for any of the prepared materials, independent of whether or not surfactants were added during preparation. For calcium pyrophosphate all preparations resulted in large crystals and although some beautiful and interesting particle morphologies were obtained, the results

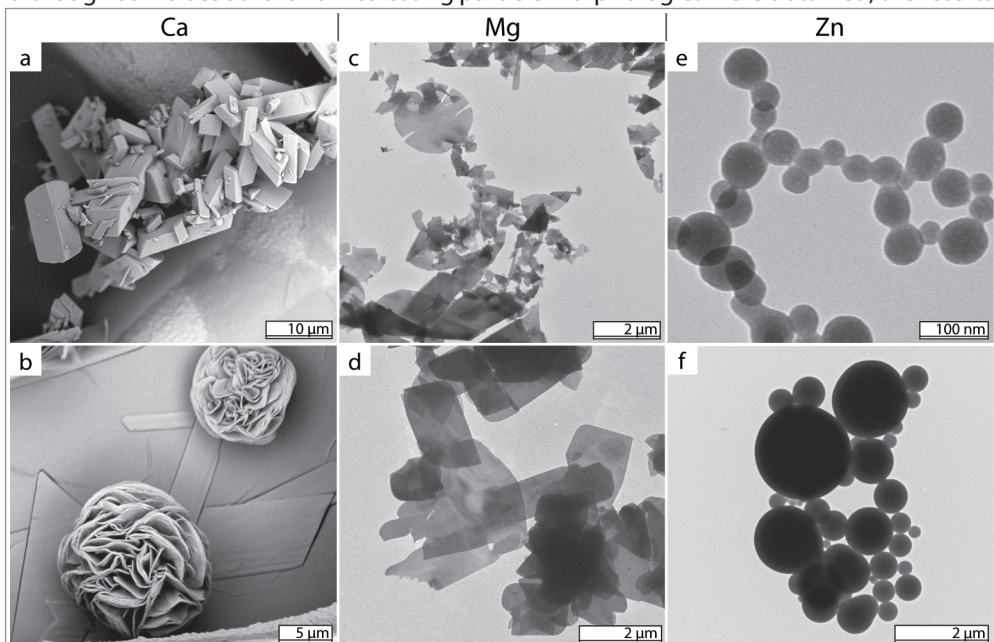


FIGURE 3.3 $M^{\text{II}}\text{PP}_5$ prepared by the urea-decomposition method. SEM images of calcium pyrophosphate prepared without any added surfactant (a) and in presence of SDS (b). TEM images of magnesium pyrophosphate with ATP (c) and CTAB (d) and zinc pyrophosphate without any surfactants (e) and with CTAB (f).

were irreproducible as each successive preparation yielded particles of different size and morphology, see FIGURE 3.3a and b. This could be due to the diverse morphology of CaPP_i that has been mentioned elsewhere [11].

MgPP_i most often forms the ellipsoidal platelets also found in CHAPTER 2, but with ATP (FIGURE 3.3c) or CTAB (FIGURE 3.3d) the resulting particles are either more rounded or rectangular, respectively. The fracturing of the particles most likely occurred during the centrifugation steps. TEM-analysis of ZnPP_i shows spherical particles of about 50 nm that might be stable when separate in solution (FIGURE 3.3e) but the dispersions sedimented within minutes regardless of further washing steps or addition of surfactants. Addition of CTAB yields significantly larger spheres (FIGURE 3.3f), but still no stable dispersion.

The preparation method proved too harsh for ATP, as the solutions containing ATP turned yellow while heating, probably indicating (partial) decomposition of the ATP [13]. Therefore, we decided not to attempt this preparation method with phosphocitrate as we had only limited amounts of the material available.

Instead of using urea to slowly raise the pH of the solution we also attempted to achieve this by slow titration with NaOH. Unfortunately, this method proved to be just as irreproducible as the particles differed in size and shape for every preparation. Moreover, none of these preparations yielded a stable dispersion, even if TEM-analysis showed nanoparticles that were small enough to be stable in dispersion.

3.3.II INJECTION METHOD

The injection method did not yield any stable dispersions for the systems containing calcium or zinc. For calcium, adding CTAB and NP-5 both yielded particles similar to those

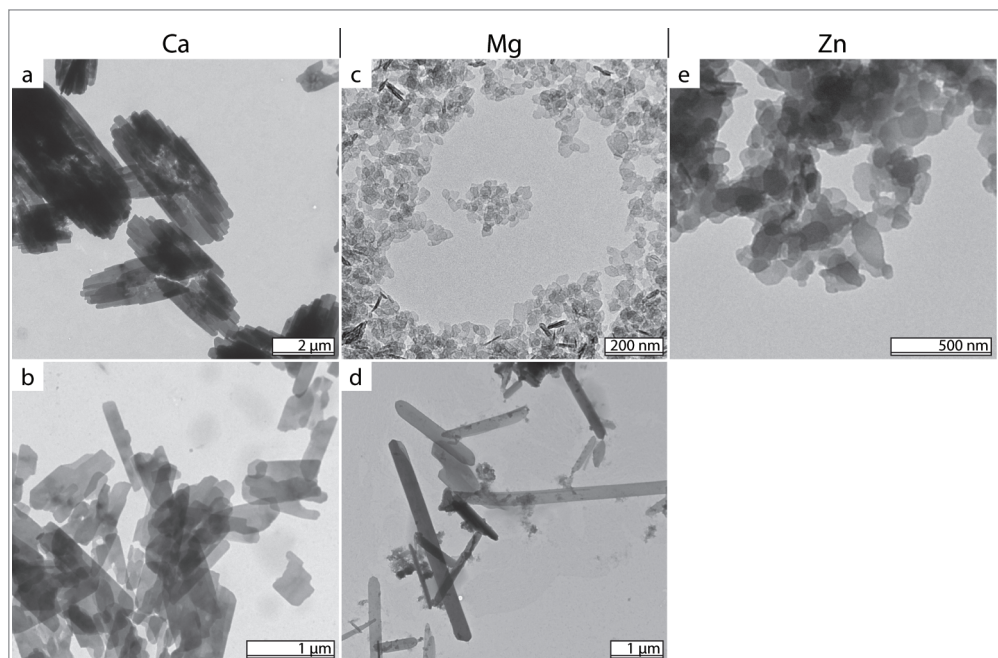


FIGURE 3.4 $M^{II}\text{PP}_i$ s prepared by the injection method. TEM images of calcium pyrophosphate without any surfactant (a) and with SDS (b), magnesium pyrophosphate without any surfactants (c) and with CTAB (d) and zinc pyrophosphate (e).

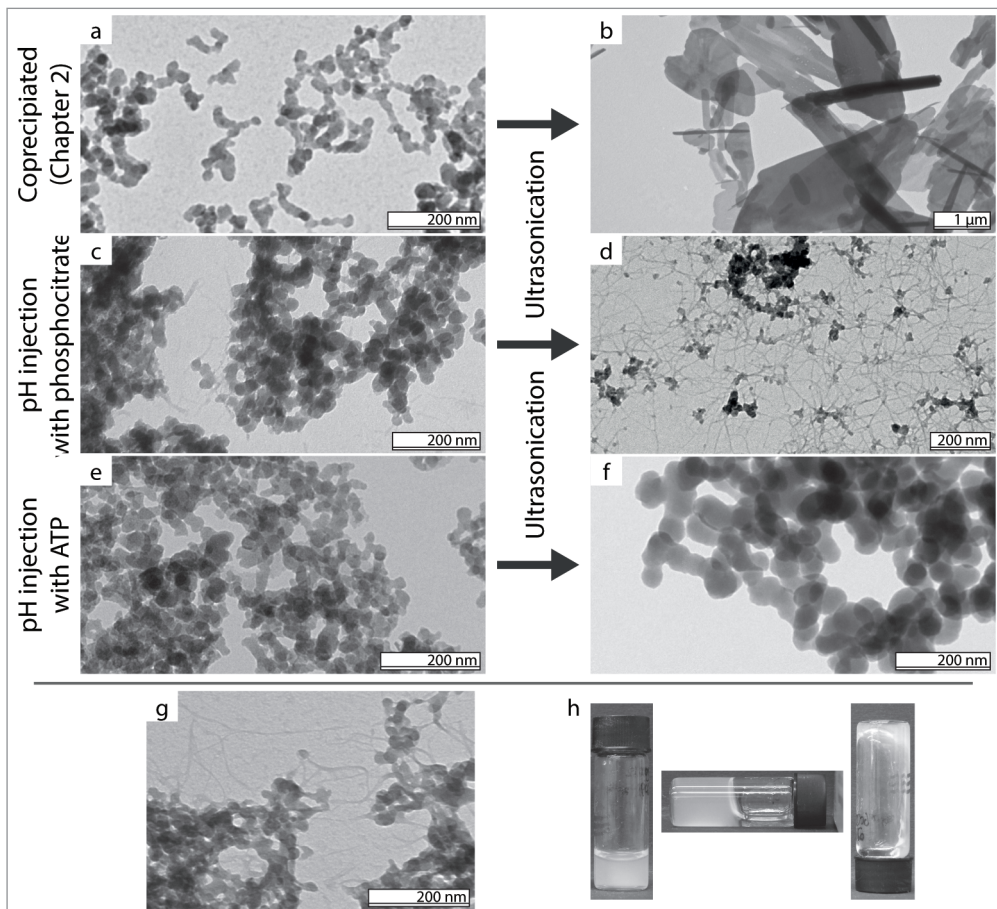


FIGURE 3.5 Calcium pyrophosphate prepared by the injection method in the presence of the specific molecules phosphocitrate or ATP. The freshly prepared samples containing phosphocitrate (c) and ATP (e) closely resemble CaPP_i prepared using the coprecipitation method from CHAPTER 2 shown here for reference (a). However, while the coprecipitated material changes into large platelets after ultrasonication (b), the clusters in the sample containing phosphocitrate are separated but still connected by wire-like material (d) and the particles containing ATP have grown in size (f). When CaPP_i is prepared using the coprecipitation method at pH 10 similar structures are found, but these are less pronounced and less connected (g). The phosphocitrate-containing sample treated with ultrasound is notably more viscous and even gel-like (h).

from the system without surfactants: large, slightly ellipsoidal platelets of around 5 μm , see FIGURE 3.4a. This morphology changed in the presence of SDS, where thinner and more rectangular platelets were found, see FIGURE 3.4b.

The inhibitor molecules ATP and phosphocitrate both had a significant influence on calcium pyrophosphate morphology. Comparing FIGURE 3.4a to FIGURE 3.5c and e, the particles had become orders of magnitude smaller in size when prepared with phosphocitrate or ATP. They closely resemble the CaPP_i found from coprecipitation (CHAPTER 2) shown in FIGURE 3.5a. Moreover, where the coprecipitated CaPP_i formed large, crystalline particles upon ultrasonic treatment, the phosphocitrate-containing CaPP_i prepared here did not change

morphology during ultrasonication. Instead, FIGURE 3.5b shows that the clusters seem to have separated while still being connected by a thin, wire-like material. It is unlikely that this is a drying effect only visible by TEM as macroscopically the dispersion becomes a soft gel after ultrasonication (see FIGURE 3.5h), confirming a connected structure. Similar thin wires have been observed when CaPP_i was prepared by coprecipitation in basic media (FIGURE 3.5g), but the sample containing PC was at neutral pH. The exact nature and origin of these wires are currently under investigation. Ultrasonic treatment of samples containing ATP resulted in somewhat larger but still amorphous particles, see FIGURE 3.5f.

For zinc pyrophosphate, none of the surfactants had influence on the morphology as these systems always resulted in the same thin, irregular platelets shown in FIGURE 3.4e and no stable dispersions were obtained.

The only system that was able to form stable dispersions was magnesium pyrophosphate. Morphologically all magnesium containing systems looked similar: from TEM analysis we found the small, thin, irregular platelets of about 50 nm shown in FIGURE 3.4c. The only exception is the system containing CTAB, which formed long needles resembling those found in CHAPTER 2, see FIGURE 3.4d. It is interesting to note here that in CHAPTER 2 we were unable to prepare MgPP_i using CTAB as surfactant as no particles were formed after complete addition of the precursor solutions. This might be a concentration effect, however, as we are using higher concentrations of MgPP_i in this chapter (0.56 g of $\text{MgPP}_i \cdot 3\text{H}_2\text{O}$ [1] intermediate in 50 ml is around 80 mM of Mg^{2+} , versus the 7 mM of Mg^{2+} in CHAPTER 2). Interestingly, the systems to which surfactant was added did not result in stable dispersions, while the system without any surfactant remained stable for more than four months, see FIGURE 3.6. The addition of more surfactant or further washing steps did not improve dispersion stability for any of the systems.

3.4 CONCLUSIONS

We have been able to prepare stable dispersions of magnesium pyrophosphate using the pH-dependent precipitation by injection method, resulting in dispersions that remained stable for over four months. The urea-decomposition method proved to be unreliable and irreproducible and could not be improved by the addition of surfactants, further washing steps or substituting the urea decomposition reaction by slow titration with NaOH. While the injection method did not result in stable dispersions of CaPP_i or ZnPP_i , we did use this method to demonstrate that phosphocitrate and ATP both inhibit the crystal formation and growth of calcium pyrophosphate. Furthermore, when phosphocitrate is used, the aggregated nanoparticles can be separated by ultrasonication, but they will still be

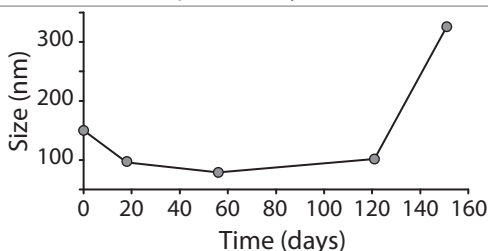


FIGURE 3.6 Particle size of a magnesium pyrophosphate dispersion prepared by the injection method as analysed by Dynamic Light Scattering. The average particle size remains stable around 100 nm for almost four months after having dropped from 150 in the first few days. After this period the particle size increases, indicating aggregation.

connected by thin, wire-like material. Similar effects have been observed in CaPP_i samples coprecipitated at high pH and this phenomenon is currently under further investigation.

3.5 ACKNOWLEDGEMENTS

Simone Vissers and Jenneke Pandelaar are thanked for preparing a great part of the samples shown in this chapter. Prof. Bert Klein-Gebbink and Nesibe Demirors of the Organic Chemistry group are thanked for their help with the synthesis of phosphocitrate.

3.6 REFERENCES

- [1] Haynes, W. M. In *Handbook of Chemistry and Physics*; Lide, D. R., Ed.; CRC Press: Boca Raton, FL, 2011.
- [2] Shaw, W. H. R.; Bordeaux, J. J. The Decomposition of Urea in Aqueous Media. *J. Am. Chem. Soc.* **1955**, *77*, 4729-4733.
- [3] Schaber, P. M.; Colson, J.; Brauer, J. Thermal Decomposition (Pyrolysis) of Urea in an Open Reaction Vessel. *Thermochim. Acta* **2004**, *424*, 131-142.
- [4] Groves, P. J.; Wilson, R. M.; Shellis, R. P. Synthesis of Triclinic Calcium Pyrophosphate Crystals. *J. Mater. Sci. Mater. Med.* **2007**, *18*, 1355-1360.
- [5] Cheung, H. S.; Sallis, J. D.; Wierzbicki, A. Phosphocitrate Blocks Calcification-Induced Articular Joint Degeneration in a Guinea Pig Model. *Arthritis & Rheum.* **2006**, *54*, 2452-2461.
- [6] Dalal, P.; Zanotti, K.; Cheung, H. S. Molecular Dynamics Simulation Studies of the Effect of Phosphocitrate on Crystal-Induced Membranolysis. *Biophys. J.* **2005**, *89*, 2251-2257.
- [7] Demadis, K. D. Structure and in Vivo Anticalcification Properties of a Polymeric Calcium-sodium-phosphocitrate Organic-inorganic Hybrid. *Inorg. Chem. Comm.* **2003**, *6*, 527-530.
- [8] Demadis, K. D.; Sallis, J. D.; Baran, P. A Crystallographically Characterized Nine-Coordinate Calcium-Phosphocitrate Complex as Calcification Inhibitor in Vivo. *J. Am. Chem. Soc.* **2001**, *123*, 10129-10130.
- [9] Wierzbicki, A.; Cheung, H. S. Molecular Modeling of Inhibition of Crystals of Calcium Pyrophosphate Dihydrate by Phosphocitrate. *J. Molecular Struct. (Theochem)* **1998**, *454*, 287-297.
- [10] Tew, W. P.; Malis, C. D.; Lehninger, A. L. Phosphocitrate Inhibits Mitochondrial and Cytosolic Accumulation of Calcium in Kidney Cells in Vivo. *Proc. Natl. Acad. Sci. USA.* **1981**, *78*, 5528-5532.
- [11] Mandel, G. S.; Halverson, P. B.; Mandel, N. S. Calcium Pyrophosphate Crystal Deposition: The Effect of Soluble Iron in a Kinetic Study using a Gelatin Matrix Model. *Scanning Microsc.* **1988**, *2*, 1177-1188.
- [12] Turhanen, P. A.; Demadis, K. D.; Vepsäläinen, J. J. A Novel Strategy for the Preparation of Naturally Occurring Phosphocitrate and its Partially Esterified Derivatives. *J. Org. Chem.* **2007**, *72*, 1468-1471.
- [13] Stockbridge, R. B.; Schroeder, G. K.; Wolfenden, R. The Rate of Spontaneous Cleavage of the Glycosidic Bond of Adenosine. *Bioorg. Chem.* **2010**, *38*, 224-228.



SECTION 2

STABILIZATION THROUGH PRECIPITATION IN A SYSTEM OF COLLOIDAL

REPEPTIZATION BY DISSOLUTION IN A SYSTEM

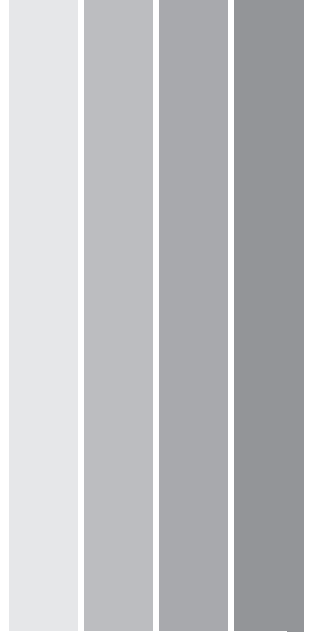
MORPHOLOGY

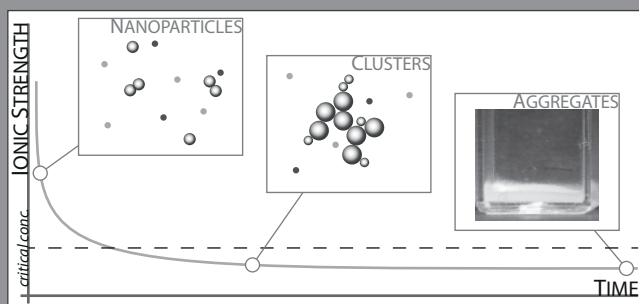
IRON(III) PYROPHOSPHATE SALTS

SYSTEM OF COLLOIDAL IRON(III) PYROPHOSPHATE

SYNTHESIS AND STABILITY OF MIXED-METAL PYROPHOSPHATE SALTS

PROPERTIES





CHAPTER 4

STABILIZATION THROUGH PRECIPITATION IN A SYSTEM OF COLLOIDAL IRON(III) PYROPHOSPHATE SALTS

The ionic strength of a solution decreases during the precipitation of an insoluble salt, which can cause an initially unstable colloidal system to stabilize during its formation. We show this effect in the precipitation and aging of colloidal iron(III) pyrophosphate, where we observe two distinct stages in the aggregation process. The first stage is the formation of nanoparticles that immediately aggregate into clusters with sizes on the order of 200 nm. In the second stage these clusters slowly grow in size but remain in dispersion for days, even months for dialyzed systems. Eventually these clusters become macroscopically large and sediment out of dispersion. Noting the clear instability of the nanoparticles, it is interesting to find two stages in their aggregation even without the use of additives such as surface active molecules. This is explained by accounting for the rapid decrease of ionic strength during precipitation, rendering the nanoparticles relatively stable when precipitation is complete. Calculating the interaction potentials for this scenario we find good agreement with the experimental observations. These results indicate that coupling of ionic strength to aggregation state can be significant and should be taken into account when considering colloidal stability of insoluble salts.

4.1 INTRODUCTION

In this chapter we present a systematic study of the stability of colloidal iron(III) pyrophosphate (FePP_i) salts and observe two characteristic stages in the aging of the system. The first stage consists of the precipitation of small nanoparticles that immediately aggregate into larger clusters. In the second stage, these clusters slowly grow in size but form an intermediate colloidal system. Eventually they become macroscopically large and sediment out of dispersion. During this growth, no change is found on the nanoparticle scale. By calculating the interaction potentials (that were discussed in CHAPTER 1) at various ionic strengths we find that the experimental results can be explained by taking into account the decreasing ionic strength during precipitation.

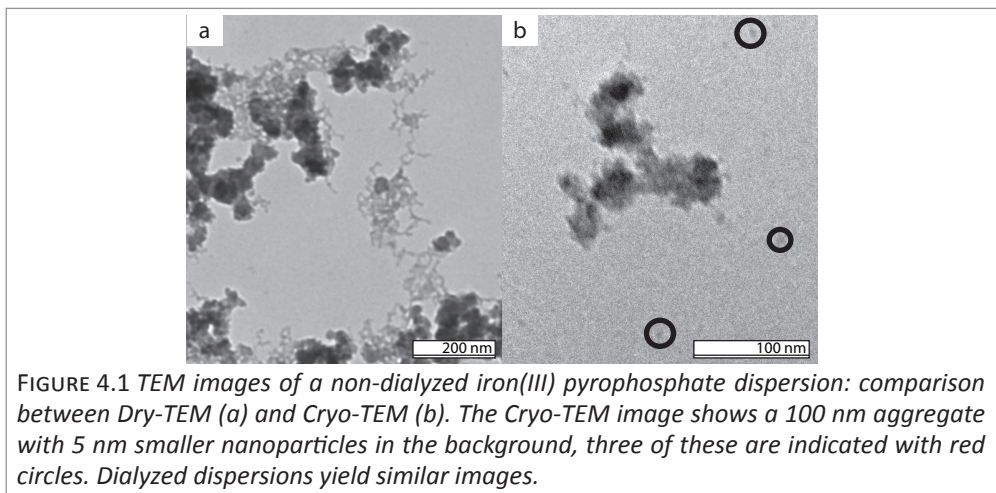
4.2 EXPERIMENTAL METHODS

4.2.I MATERIALS

$\text{FeCl}_3 \cdot 6\text{H}_2\text{O}$ and $\text{AlCl}_3 \cdot 6\text{H}_2\text{O}$ were purchased from Sigma Aldrich, NaCl and $\text{Na}_4\text{P}_2\text{O}_7 \cdot 10\text{H}_2\text{O}$ from Merck and $\text{Mg}(\text{NO}_3)_2 \cdot 6\text{H}_2\text{O}$ from Acros. All chemicals were used as received.

4.2.II PREPARATION

Colloidal particles of iron pyrophosphate were prepared by dissolving 0.857 mmol FeCl_3 in 50 ml water and adding this dropwise in about 15 minutes to 0.643 mmol $\text{Na}_4\text{P}_2\text{O}_7$ in 100 ml water while stirring in a 250 ml round bottom flask (rbf). In general, a turbid white dispersion forms during the addition of the final ~ 5 ml. For the concentration series, different concentrations of iron and pyrophosphate were used. All concentrations mentioned in this work refer to the concentration of iron(III) in the final volume. The ratio $\text{Fe}:\text{PP}_i$ used in the precipitation is always stoichiometric, 4:3. All solutions were prepared in water deionized by a Millipore Synergy water purification system. Dialysis experiments were performed using Spectra/Por 2 Dialysis Membrane, MWCO 12-14,000. In a typical dialysis experiment the dispersion is dialyzed for 12 days during which the water is changed six times. The dialysis medium reaches a stable conductivity of 2.7 $\mu\text{S}/\text{cm}$ after changing the medium three times.



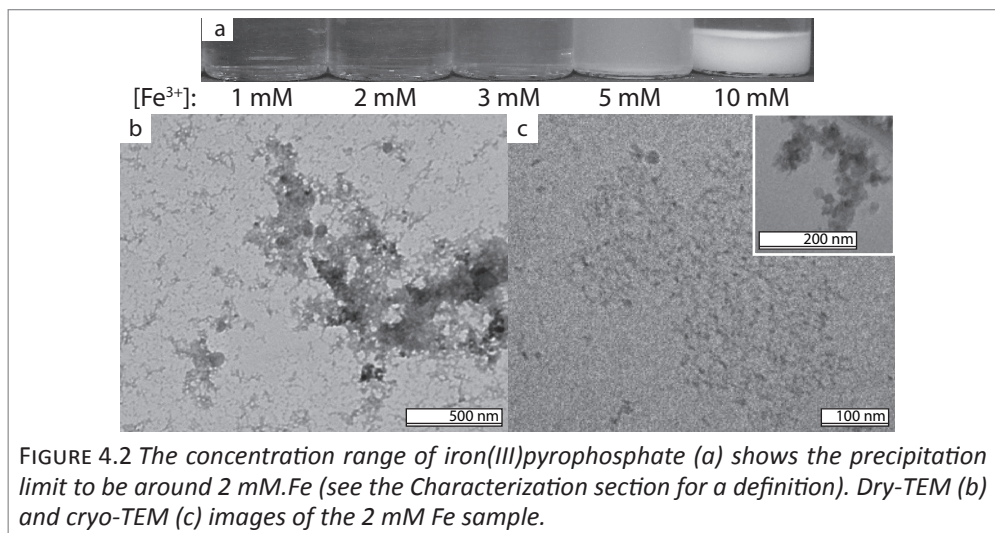


FIGURE 4.2 The concentration range of iron(III)pyrophosphate (a) shows the precipitation limit to be around 2 mM. Fe (see the Characterization section for a definition). Dry-TEM (b) and cryo-TEM (c) images of the 2 mM Fe sample.

4.2.III ANALYSIS

Dynamic Light Scattering (DLS) and zeta potential (ZP) measurements were performed on a Malvern Instruments Zetasizer Nano series machine in backscatter mode at 25°C with 5 minutes of equilibration time. The DLS measurements were performed in ten runs of 15 measurements per run yielding a size averaged over all ten runs and a standard deviation between the runs. The zeta potential measurements followed the same procedure but used ten runs of 50 measurements. For transmission electron microscopy (TEM), dispersions were diluted ten times and dried on a copper grid prior to analysis using a Tecnai 12 electron microscope from FEI Company. This method is referred to as dry-TEM in this work. For cryo-TEM, one drop of unaltered dispersion was placed on a cryo-TEM grid and blotted for 1 second before being quenched in liquid ethane. Samples were stored in liquid nitrogen before being analyzed using a Tecnai 20 electron microscope.

4.3 RESULTS AND DISCUSSION

4.3.I CHARACTERIZATION

IRON PYROPHOSPHATE. FIGURE 4.1a depicts a typical dry-TEM image of an (dialyzed or non-dialyzed) FePP_i dispersion, showing extended aggregates consisting of polydisperse particles of 20 nm on average, with attached networks of ~ 5 nm particles. Cryo-TEM analysis in FIGURE 4.1b yields similar images with one main difference: many of the smaller 5 nm nanoparticles are present as individual particles. This indicates that while drying effects occur for the 5 nm particles during the dry-TEM preparation method, the 20 nm particles are mostly unaffected. As the preparation method can have a large effect on particle size and shape and colloidal stability, we have tried various addition speeds and orders of addition. However, we have found little difference in particle morphology between methods as discussed in APPENDIX I.

CONCENTRATION. A concentration series ranging from 0.1 to 10 mM Fe was prepared. As mentioned in the Preparation section, concentrations refer to the concentration of iron(III) in the final volume, the ratio between Fe and PP_i is always stoichiometric (4:3). The concentration in the standard procedure was 5.7 mM. Five of the samples around the precipitation limit are shown in FIGURE 4.2a. From these samples the precipitation limit was

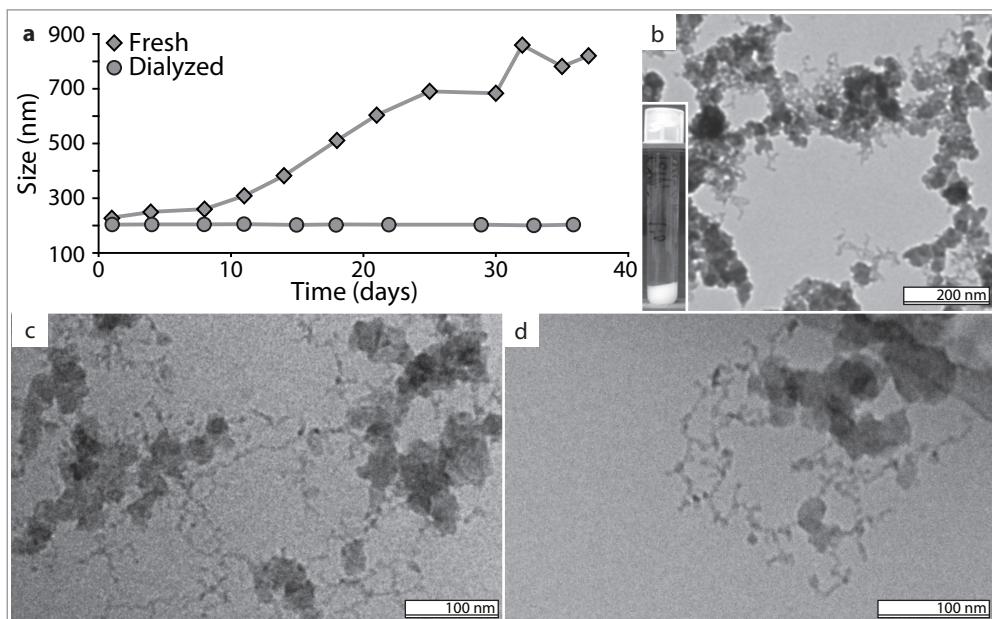


FIGURE 4.3 (a) DLS analysis shows growth of the cluster size over time for the dialyzed and non-dialyzed systems, while the TEM image (b) of the non-dialyzed system 15 days after preparation reveals no clear difference with the freshly prepared system. At this time the dispersion has sedimented completely (see inset). Cryo-TEM after 15 days (c) and four months (d) shows the smaller 5 nm nanoparticles forming a network. This network formation was not observed for the dialyzed system.

estimated to be 2 mM: below this concentration the samples showed hardly any reflection when illuminated with a laser. DLS analysis of the dispersions from 2 to 5 mM shows cluster sizes similar to the standard concentration (5.7 mM) with a polydisperse particle size of 150 nm on average. Below 2.0 mM the noise levels become too high for DLS analysis. Both cryo- and dry-TEM images of the 2 mM sample show extended networks of small particles, see FIGURE 4.2b and c. Aggregates of 20 nm particles are also observed as shown in the inset of inset of FIGURE 4.2c, but there are fewer present than at higher concentrations.

4.3.II CLUSTER STABILITY

When a non-dialyzed system is redispersed after having sedimented completely, subsequent sedimentation is noticeably faster. After several sedimentation and redispersion cycles it will even settle within minutes to hours depending on sample concentration and age. This observation is quantified by following the cluster size of a 5.7 mM system over time using DLS, see FIGURE 4.3a. After about 24 days the aggregates in this dispersion became too large and polydisperse for the DLS measurements to be reliable. During this period, the cluster size in a dialyzed system remained stable at 200 nm. Comparing dry-TEM images of fresh dispersions (FIGURE 4.1a) to those aged for fifteen days (FIGURE 4.3b), we find no significant difference in particle size or morphology. However, cryo-TEM images of aged samples show that the small, 5 nm subunits are now forming a network (FIGURE 4.3c and d), while the aged dialyzed system shows no difference (not shown). The dialyzed system eventually also aggregates completely: after 6 months the

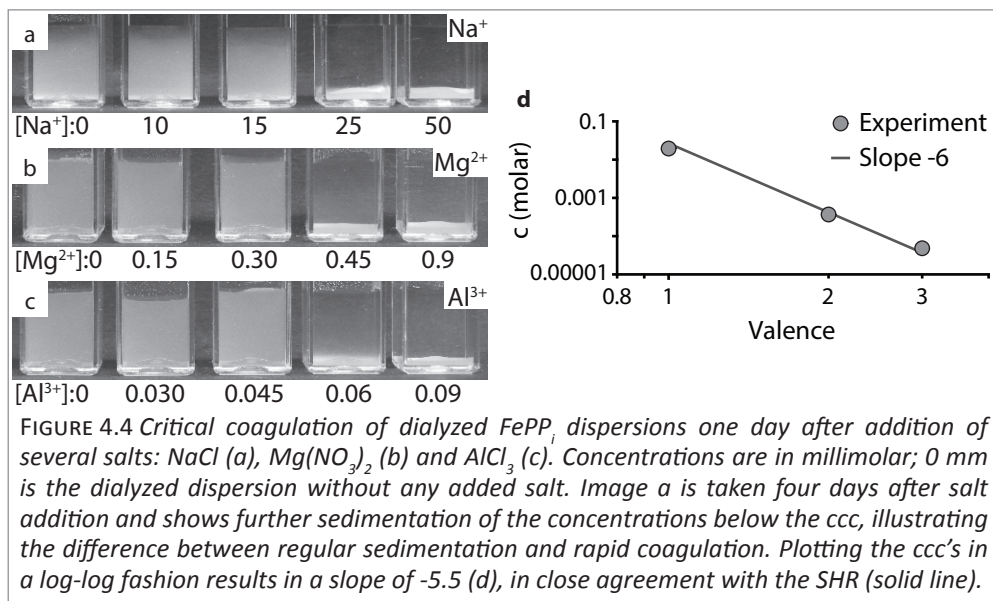


FIGURE 4.4 Critical coagulation of dialyzed $FePP_1$ dispersions one day after addition of several salts: $NaCl$ (a), $Mg(NO_3)_2$ (b) and $AlCl_3$ (c). Concentrations are in millimolar; 0 mM is the dialyzed dispersion without any added salt. Image a is taken four days after salt addition and shows further sedimentation of the concentrations below the ccc, illustrating the difference between regular sedimentation and rapid coagulation. Plotting the ccc's in a log-log fashion results in a slope of -5.5 (d), in close agreement with the SHR (solid line).

cluster size has become too large for DLS analysis and the system cannot be redispersed anymore.

4.3.III EFFECT OF SALT ADDITION

We find that the addition of a fixed concentration of salt critically destabilizes a dialyzed system of $FePP_1$ and that this concentration varies with the valence of the added cation: 25 mM for Na^+ , 0.45 mM for Mg^{2+} and 0.06 mM for Al^{3+} , see FIGURE 4.4. From here on we will refer to this concentration as the critical coagulation concentration (ccc) [1]. The difference between regular sedimentation and a critically destabilized system can be seen in FIGURE 4.4; the 0 mM sample in FIGURE 4.4b is a freshly dialyzed system without any added salt, the 0 mM in FIGURE 4.4a is four days after preparation. This illustrates the gradual sedimentation of a dialyzed system, while comparing the samples above and below the ccc shows the critical destabilization. The empirical Schulze-Hardy rule (SHR) states that the concentration of electrolyte needed to critically destabilize a colloidal dispersion inversely scales with ion valence to the power six [2]. Plotting the ccc values in a log-log fashion in FIGURE 4.4d we find a slope of -5.5 (circles), in close agreement with the SHR (red line).

The results of DLS and zeta potential analyses of these dispersions are summarized in TABLE 4.1. DLS analysis of the Na^+ concentration range reflects the results of FIGURE 4.4a: the sample at the ccc has a higher average cluster size and higher standard deviation. The Mg^{2+} and Al^{3+} samples show similar behavior slightly above the ccc. As can be seen from TABLE 4.1, the critical coagulation was not caused by reaching the iso-electric point of the particles as the zeta potential had not yet reached zero. The strong dependence of the zeta potential on the (concentration of the) added ion shown in TABLE 4.1 is a known effect for specifically adsorbing ions [1, 3]. The negative Zeta potential and the fact that it responds so strongly to addition of cations both indicate a negative surface charge of the $FePP_1$ particles.

TABLE 4.1 Cluster size and zeta potential depending on concentration of added ion

Cation	Concentration (mM)	Size (nm)	St. dev.* (nm)	Zeta potential (mV)	St. dev.** (mV)
Dialyzed***	-	211	1.9	-51.2	0.9
Na ⁺	15	213	1.5	-45.0	5.74
	25 (ccc)	290	19	-42.3	15.9
Mg ²⁺	0.30	212	1.5	-19.6	0.15
	0.45 (ccc)	214	1.5	-18.8	0.12
	0.60	269	16	-18.3	0.35
Al ³⁺	0.045	220	1.2	-25.9	0.32
	0.060 (ccc)	246	2.4	-24.1	0.60
	0.090	2000	30	-19.3	0.15

*DLS measurements are performed in 10 runs with 15 measurements per run, the standard deviation is the deviation between the averages of the runs. Note that this is not the standard deviation of the cluster size.

**Zeta potential measurements are performed in 10 runs of 50 measurements. All samples are at pH 3.6.

***Dialyzed system without any additional salt.

4.3.IV CALCULATION OF THE INTERACTION POTENTIAL

As long as not all FePP_i has precipitated, the ionic strength during precipitation is higher than just the NaCl counterion concentration of the final dispersion. Complete precipitation is defined here as the point at which the ionic strength of Fe^{3+} and PP_i^{4-} in solution is negligible: at the end of the precipitation process all material is present in the form of solid FePP_i particles as the solubility of FePP_i is very low.

Therefore, the ionic strength

$$I = \frac{1}{2} \sum_{i=1}^n c_i z_i^2 \quad (4.1)$$

(with c_i the molar concentration and z_i the valence of ion i) will only be 17 mM (Na⁺ and Cl⁻) at complete precipitation. At the start of the reaction an additional 5.7 mM Fe^{3+} and 4.3 mM PP_i^{4-} are present, resulting in an ionic strength of 77 mM. The initial concentration of Fe^{3+} is much higher than the ccc found for trivalent ions in FIGURE 4.4, but will decrease during precipitation. We calculate the full interaction potential for the small (5 nm) and large (20 nm) nanoparticles at various concentrations of Fe^{3+} during the precipitation reaction to estimate particle stability, see FIGURE 4.5 for results. In these calculations we used a Hamaker constant of $25 k_B T$ and a surface potential of -45 mV. For details on these calculations see APPENDIX III. We refer to the iron concentration as c_{Fe} and the initial iron concentration as c_0 (5.7 mM), the concentration of PP_i used in the calculations is always 3/4 that of iron. Note here that the potentials in FIGURE 4.5 are expressed in the concentration of Fe^{3+} instead of the total ionic strength, but the calculations include all ions.

We find that at the start of the reaction both particle sizes are unstable because no (significant) stabilizing barrier is present in the interaction potentials (dash-dotted lines, $c_{\text{Fe}} = c_0$). When half of the FePP_i has precipitated, the 5 nm particles have a stabilizing barrier of roughly $1 k_B T$ while the 20 nm particles are still unstable at this point (dotted lines, $c_{\text{Fe}} = 0.5 \cdot c_0$). For the 20 nm particles, the potential becomes only just positive when

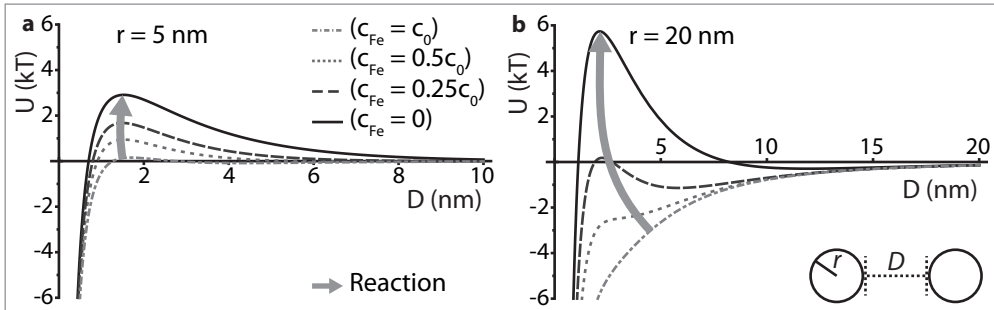


FIGURE 4.5 Interaction potentials in units of $k_B T$ of 5 nm (a) and 20 nm (b) particles at various concentrations of Fe^{3+} during the precipitation process. The concentration of iron in solution is labeled c_{Fe} , c_0 is the initial concentration at the start of the precipitation (5.7 mM). The green arrows indicate the change in the potential during the course of the precipitation process.

3/4 of the FePP_i has precipitated (dashed lines, $c_{\text{Fe}} = 0.25 \cdot c_0$). However, when precipitation is complete the stabilizing barrier is higher for the 20 nm particles than for the 5 nm particles (solid lines, $c_{\text{Fe}} = 0$).

4.3.v DISCUSSION

The experimental results show two stages in the aggregation process of the system. The first stage consists of the precipitation of nanoparticles and their immediate aggregation into 200 nm clusters. These clusters appear to be colloidally stable for long periods, illustrated by the presence of a ccc and the fact that the system obeys the Schulze-Hardy rule. However, the clusters slowly but continuously grow over time until they become too large to remain in dispersion. The calculated interaction potentials provide us with an explanation for these observations. FIGURE 4.5 shows that the 20 nm particles initially are unstable and will aggregate while the 5 nm particles are kept relatively stable by the small energy barrier, as seen in FIGURE 4.1. During precipitation the ionic strength of the solution decreases until the 20 nm particles also become stable, stopping further immediate aggregation and yielding finite (~200 nm) clusters in dispersion. The continuous further growth of these clusters could be caused by the formation of the networks of 5 nm particles shown in FIGURE 4.3, which seems to occur on a similar timescale. As the final stabilizing barrier is relatively low for the 5 nm particles (~3 kT, see FIGURE 4.5), these particles can slowly aggregate and connect the already existing larger clusters. This is confirmed by the fact that the dialyzed system remains stable for much longer periods, as the stabilizing barrier will be higher with the lowered ionic strength. The entire process is schematically summarized in FIGURE 4.6. In this process we assume that the 5 nm particles will also aggregate with the 20 nm particles (especially in the early stages of the precipitation), or with 5 nm particles already attached to clusters of 20 nm particles, see FIGURE 4.6 image 3 and 4.

While significantly larger, the clusters are not unlike the prenucleation clusters found for apatite (calcium phosphate). While Dey *et al.* [4] study the formation of these clusters and crystals on templates, they also encounter the clusters in solution without any template present. It is therefore possible that the formation and growth of FePP_i is governed by similar principles: the 5 nm nanoparticles have grown from the prenucleation seeds and the 20 nm nanoparticles from the densification of the clusters in absence of a template.

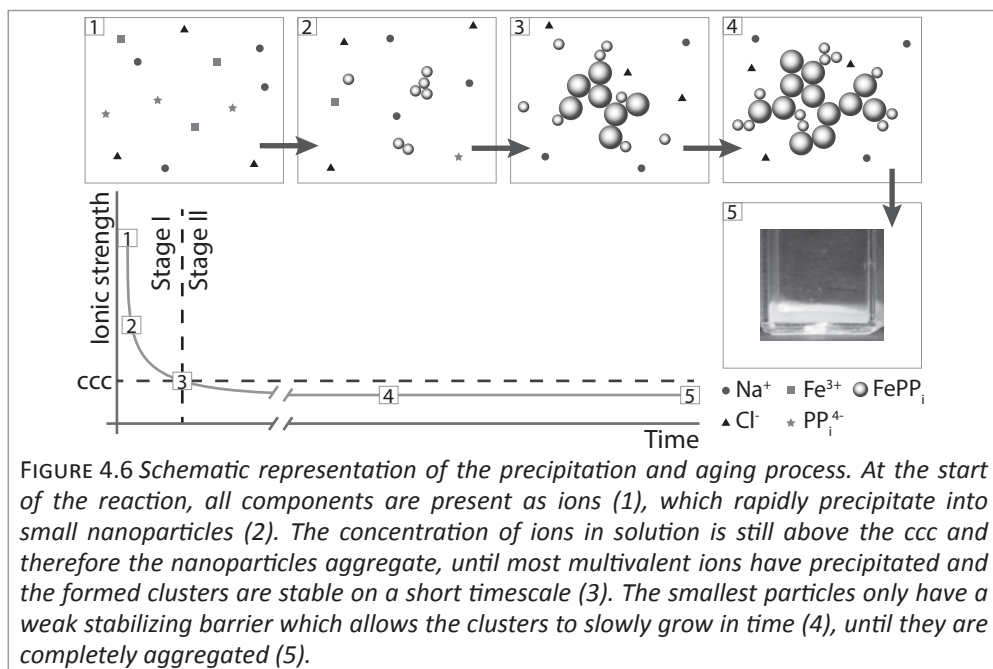


FIGURE 4.6 Schematic representation of the precipitation and aging process. At the start of the reaction, all components are present as ions (1), which rapidly precipitate into small nanoparticles (2). The concentration of ions in solution is still above the ccc and therefore the nanoparticles aggregate, until most multivalent ions have precipitated and the formed clusters are stable on a short timescale (3). The smallest particles only have a weak stabilizing barrier which allows the clusters to slowly grow in time (4), until they are completely aggregated (5).

It would be interesting to see if crystallization of FePP_i can be induced by performing the precipitation in the presence of a template, as colloidal FePP_i always forms amorphous precipitates (see CHAPTER 2 [5]).

Having demonstrated that decreasing ionic strength during precipitation is the cause of the observed two stage precipitation, we expect that this effect is general for the precipitation of insoluble salts. However, as the precipitating ions are multivalent in the case of FePP_i , this effect is amplified as these ions have a stronger effect on colloidal stability (see FIGURE 4.4). When working with mono- and divalent ions it is likely that the concentration is below the ccc before and after precipitation and thus this effect will not be observed.

4.4 CONCLUSIONS

We have studied the colloidal system of iron(III) pyrophosphate and find two stages in its aggregation process. In the first stage small nanoparticles precipitate and immediately form clusters. In the second stage these clusters slowly grow over the course of days until they become macroscopically large and sediment out of dispersion. While the nanoparticle and aggregated states are common in most colloidal systems, the presence of this intermediate cluster stage is surprising regarding the instability of the nanoparticles. Our experimental observations are consistently explained by calculating the particle interaction potentials at various ionic strengths. Taking into account that the ionic strength decreases during precipitation, we find that the nanoparticles are unstable at the start of the precipitation but form a stabilizing barrier in their interaction potential when precipitation is complete. These results explain both the immediate clustering of the nanoparticles and the slow further growth of the system. Finally, we have shown that the slow growth can be inhibited by dialysis. As this lowers the ionic strength even further, the stabilizing barrier increases and the system is kept from complete aggregation for

periods of months.

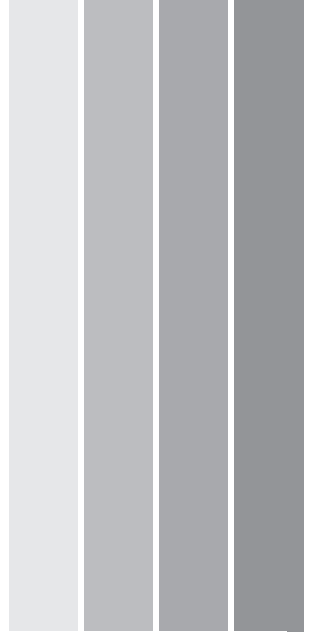
4.5 ACKNOWLEDGEMENTS

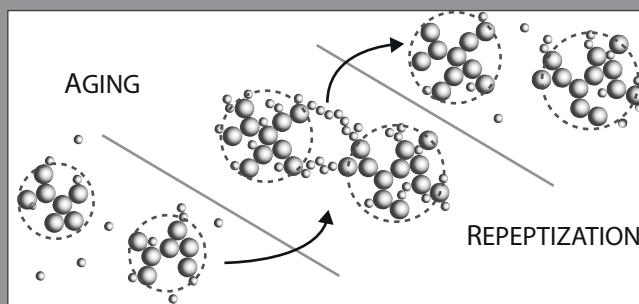
We thank J.D. Meeldijk of the Electron Microscopy group in Utrecht for cryo-TEM analysis.

This chapter has been reprinted from *Journal of Colloid and Interface Science*, 381, Y.M. van Leeuwen, K.P. Velikov and W.K. Kegel, Stabilization through precipitation in a system of colloidal iron(III) pyrophosphate salts, 43-47, **2012**, with permission from Elsevier

4.6 REFERENCES

- [1] Hunter, R. J. In *Foundations of Colloid Science*; Oxford University Press: 2001.
- [2] Verwey, E. J. W.; Overbeek, J. T. G. In *Theory of the Stability of Lyophobic Colloids*; Dover Publications, Inc.: 1999.
- [3] Saka, E. E.; Güler, C. The Effects of Electrolyte Concentration, Ion Species and pH on the Zeta Potential and Electrokinetic Charge Density of Montmorillonite. *Clay Miner.* **2006**, *41*, 853-861.
- [4] Dey, A.; Bomans, P. H. H.; Sommerdijk, N. A. J. M. The Role of Prenucleation Clusters in Surface-Induced Calcium Phosphate Crystallization. *Nature Materials* **2010**, *9*, 1010-1014.
- [5] van Leeuwen, Y. M.; Velikov, K. P.; Kegel, W. K. Morphology of Colloidal Metal Pyrophosphate Salts. *RSC Adv.* **2012**, *2*, 2534-2540.





CHAPTER 5

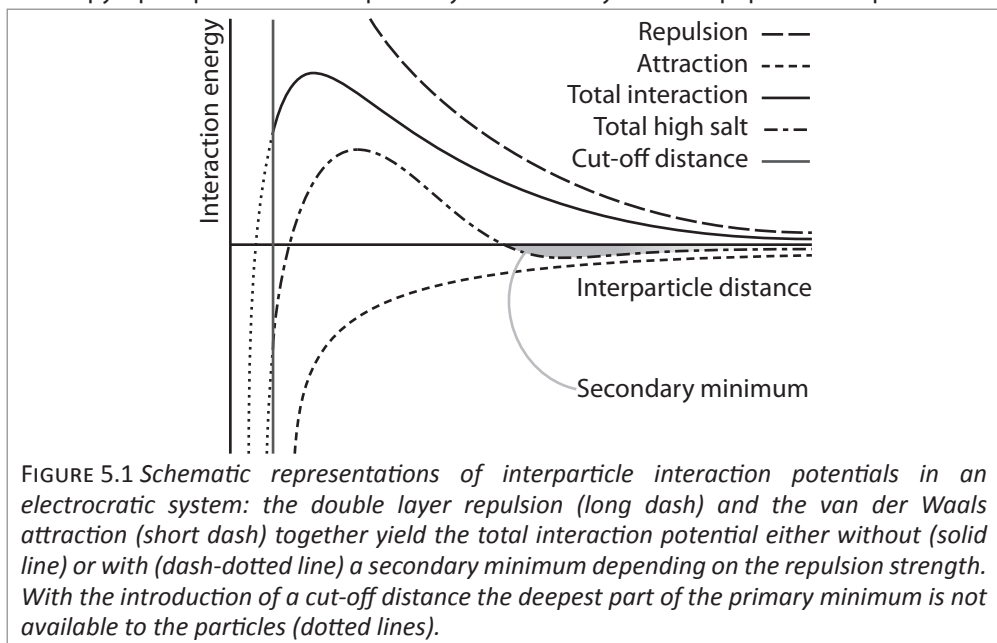
REPEPTIZATION BY DISSOLUTION IN A SYSTEM OF COLLOIDAL IRON(III) PYROPHOSPHATE

Repeptization (redispersion) from an aggregated state is usually only possible in charge-stabilized colloidal systems if the system is either coagulated in the secondary minimum of the interaction potential, or if the system cannot settle completely into the primary minimum. In this Chapter we analyse the zeta-potential (ZP), conductivity and long-term stability of colloidal systems of iron(III) pyrophosphate and surprisingly find that the system seems to defy conventional wisdom as it can be repeptized from its coagulated state regardless of aging time and background ions. Moreover, after having been stored for up to a month in 2 M NaCl, dialysis of iron pyrophosphate will yield a colloidal dispersion that is actually stable for a longer period of time than a fresh system with background electrolyte removed.

5.1 INTRODUCTION

Destabilization and coagulation in the primary minimum of the interaction potential occurs when colliding particles overcome the repulsion and cross the stabilizing barrier, see FIGURE 5.1. Once trapped, lowering the ionic strength will only reeptize (redisperse) the particles if there is a distance of closest approach (or 'cut-off' distance) between the particles, otherwise reeptization from the deep primary minimum will be impossible [1]. A possible cause for such a cut-off distance in an electrocratic (charge-stabilized) system arises if interparticle interactions during a Brownian collision occur under constant surface charge instead of constant surface potential, as the re-equilibration needed for a constant potential takes place in a timespan orders of magnitude larger than that of the collisions. This implies that the cut-off distance will vanish over time with equilibration, explaining why aged systems cannot be reeptized as is indeed often observed [2, 3]. Other possible causes for a cut-off distance include surface roughness and the presence of the hydration layer itself, but these will also vanish over time by re-equilibration or sintering [1, 4-6]. Note that we are working with a system that contains no stabilizing agents such as surfactants or polymers, making steric stabilization (another common cause for a distance of closest approach) highly unlikely.

While reeptization is important from a practical viewpoint as it governs the ability for colloidal dispersions to be dried, stored and redispersed, it is almost exclusively studied when going from the dried to the dispersed state [4, 7], comprising only a minor part of the phenomenon. However, current literature agrees that while reeptization from the primary minimum can be experimentally realized when coagulation is induced by monovalent background ions and short aging times, the reeptization of systems aggregated by polyvalent ions is not possible by simply lowering the ionic strength of the medium: it needs additional means such as addition of surfactants [8] or complexing agents [9]. In this work we further investigate the long-term stability of colloidal systems of iron pyrophosphate and unexpectedly find that they can be reeptized independent of



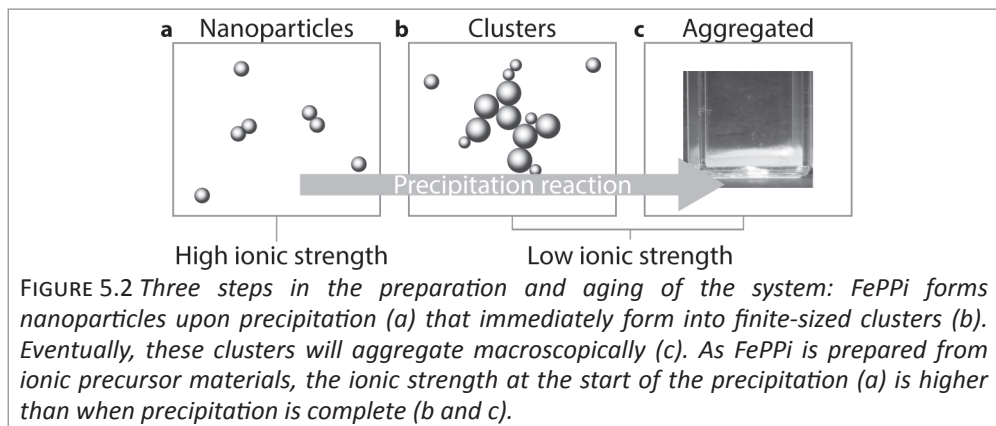


FIGURE 5.2 Three steps in the preparation and aging of the system: FePPI forms nanoparticles upon precipitation (a) that immediately form into finite-sized clusters (b). Eventually, these clusters will aggregate macroscopically (c). As FePPI is prepared from ionic precursor materials, the ionic strength at the start of the precipitation (a) is higher than when precipitation is complete (b and c).

aging time and valence of background ions and without any further additives.

We have shown in CHAPTER 4 that when colloidal iron pyrophosphate is prepared by coprecipitation, the material precipitates into nanometer sized particles that immediately aggregate into ~ 200 nm clusters. While these clusters remain in dispersion for days, they slowly grow until the system is macroscopically aggregated. Our calculations showed that that the initial instability (resulting in the aggregation into small clusters) is caused by the higher ionic strength at the start of the precipitation. When precipitation is complete, the ionic strength is lower and the clusters have become (meta)stable. We also observed that the system consists of two particle sizes: 20 nm particles in the clusters and 5 nm particles both in the clusters and separate in solution, see FIGURE 5.2. These results, together with cryo-TEM analysis, lead us to propose that the individual 5 nm particles caused the further aggregation by linking the clusters together.

In the current work we further investigate the colloidal stability of FePPI and find that (1) we can prepare a system that remains stable for more than a year and (2) we are able to reepectize a system that has been coagulated under circumstances that should not allow for reepectization as discussed above.

5.2 EXPERIMENTAL

5.2.1 PREPARATION

Samples were prepared as described in CHAPTER 2. In brief, 0.857 mmol $\text{FeCl}_3 \cdot 6\text{H}_2\text{O}$ (Sigma Aldrich) in 50 ml water was added drop wise in about 15 min to 0.643 mmol $\text{Na}_4\text{P}_2\text{O}_7 \cdot 10\text{H}_2\text{O}$ (Acros) in 100 ml water while stirring. For the dialysis experiments dispersions were dialyzed using Spectra/Por 2 Dialysis Membrane, molecular weight cut-off (MWCO) 12-14.000 Da, corresponding to roughly 1.5 nm. In each dialysis run, 20 ml dispersion in a dialysis tube was stored in 500 ml medium, which was replaced with new water every day. For the reepectization experiment, NaCl, $\text{LiCl} \cdot x\text{H}_2\text{O}$, KCl, $\text{MgCl}_2 \cdot 6\text{H}_2\text{O}$ and $\text{AlCl}_3 \cdot 6\text{H}_2\text{O}$ were all obtained from Sigma Aldrich. All chemicals were used as received, solutions were prepared in water deionized using a Millipore Synergy water purification system, which was also used for the dialysis medium. We have prepared samples containing excess metal or pyrophosphate and samples containing excess background ions, these are described in Appendix IV.

5.2.II ANALYSIS

Dynamic Light Scattering and electrophoretic mobility analysis measurements were performed using a Malvern Instruments Zetasizer Nano series machine operating in backscatter mode at 25°C with 5 minutes of equilibration time. Samples for the DLS time series were filtered over a Minisart disposable cellulose acetate filter (0.45 μm poresize, 16555-K) and stored in a plastic disposable DLS cuvette sealed with parafilm. Samples for electrophoretic mobility measurements were taken from the stock sample, DLS analysis of these samples showed no difference with the sealed DLS samples. For cryo-TEM, one drop of unaltered dispersion was placed on a cryo-TEM grid and blotted for 1 second before being quenched in liquid ethane. Samples were stored in liquid nitrogen before being analyzed using a Tecnai 20 electron microscope.

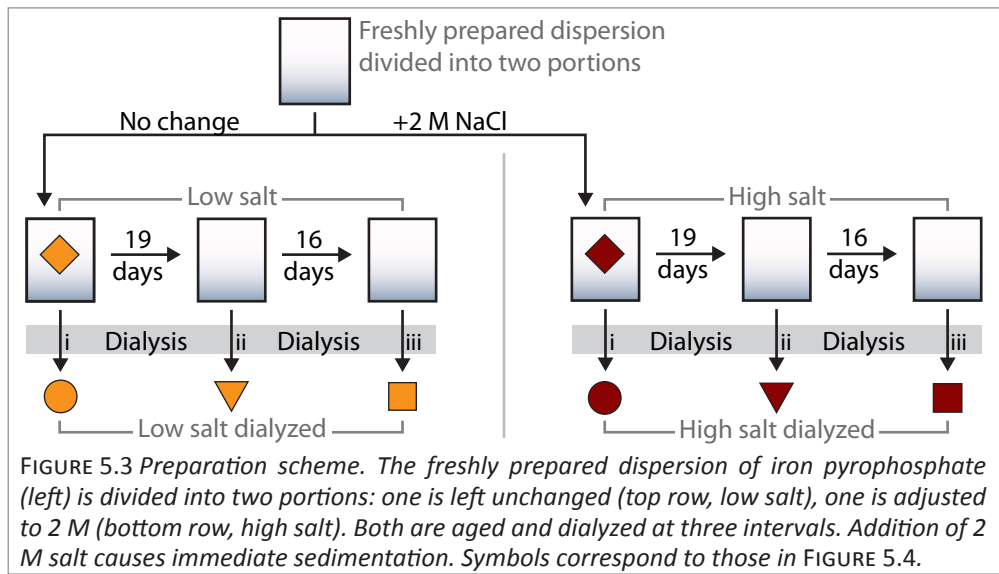
5.3 RESULTS

A freshly prepared dispersion of iron pyrophosphate was divided into two portions. One solution was left unchanged (containing 17 mM NaCl and labeled low salt or LS), to the other NaCl, KCl or LiCl was added to obtain a 2 M solution (labeled high salt or HS). Samples were taken from both dispersions at three intervals: (i) one hour, (ii) 19 days and (iii) 35 days after preparation, see FIGURE 5.3 for a schematic overview of the sample preparation. These samples were dialyzed for three or six days and followed over time by means of Dynamic Light Scattering (DLS) analysis.

For clarity we divide our results in two parts in this section: (I) the reptitization of aggregated systems and (II) the long-term stability of (dialyzed) systems.

5.3.I REPEPTIZATION OF AGGREGATED SYSTEMS

As can be seen in FIGURE 5.4a, all dialyzed samples (either low salt or NaCl high salt) were reptitized independent of waiting time or salt concentration. The low salt samples have cluster sizes of around 200 nm after dialysis, while the high salt samples show sizes of around 500 nm immediately after dialysis, which slowly decrease to 400 nm in days. Note that these sizes should not be interpreted as absolute numbers; polydispersity is very high



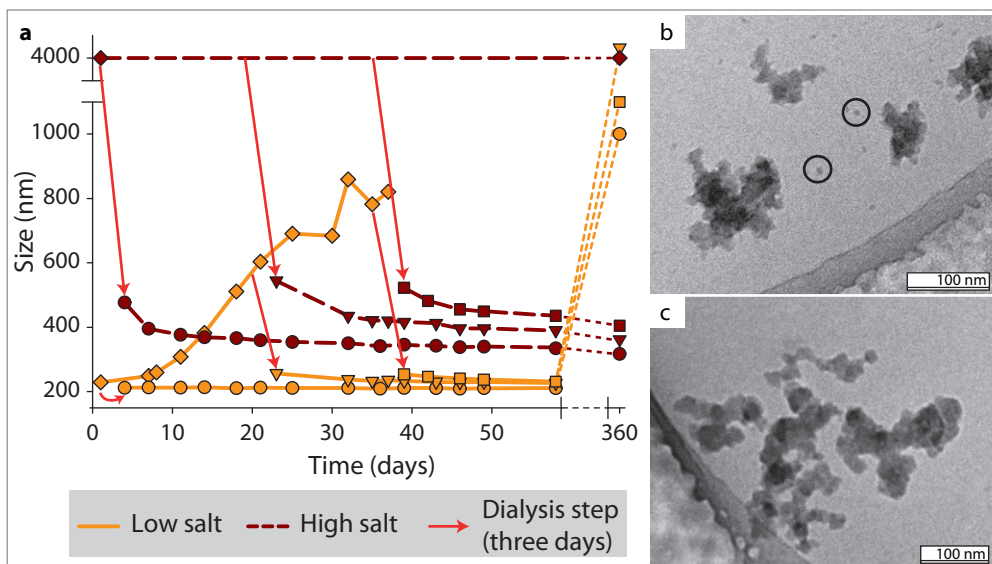


FIGURE 5.4 Growth of the cluster size over time for the NaCl reptization experiment measured by Dynamic Light Scattering (a). The dispersion without any added salt shows similar growth as before (light diamonds). The dispersion with an additional 2 M NaCl could not be accurately analyzed due to the macroscopic size of the particles, but is indicated for reference (dark diamonds). Dialysis (three days) performed immediately (circles), 19 days (triangles) and 35 days (squares) after preparation, red arrows indicate dialysis steps. Symbols correspond to those in FIGURE 5.3. Cryo-TEM analysis of the low salt system dialyzed for three days (b) shows no difference with previous images, two individual 5 nm are indicated with circles. After six days of dialysis, the 5 nm particles are absent (c).

in these samples (>30%). The unchanged initial low salt system shows the characteristic growth found CHAPTER 4 and is completely aggregated after 20 days. The cryo-TEM micrograph depicted in FIGURE 5.4b shows no change in size or number of nanoparticles after 3 days of dialysis, but after 6 days of dialysis the unbound, approximately 5 nm sized particles are no longer present (FIGURE 5.4c). The pore size of the dialysis membrane is sufficiently small to prevent the 5 nm particles from leaking out. Longer dialysis times and different background cations (K^+ , Li^+) yield similar results (not shown).

TABLE 5.1 shows that high salt systems with Mg^{2+} and Fe^{3+} as background ions can also be reptitized although they result in larger cluster sizes. It should be noted here that the Fe^{3+} system is not aged with a 1 M excess, as adding such an amount of Al^{3+} or Fe^{3+} completely dissolves the particles. This is most likely due to a change in pH, see APPENDIX IV A for details. Because it could be argued that an excess of 0.2 mM might lead to aggregation in the secondary minimum instead of the primary, the system was aged for one month before dialysis to allow for further aggregation into the primary minimum.

5.3.II DIALYSIS TIME AND LONG-TERM STABILITY

While all systems were initially reptitized, most systems had aggregated completely roughly one year after preparation. FIGURE 5.4a shows that the only samples that were still stable after one year were those prepared by a 3-day dialysis of the high salt system, independent of waiting time. Note that the high salt systems that were dialyzed for 6 days

TABLE 5.1 Dynamic light scattering, zeta-potential and conductivity results of the high salt systems with multivalent ions

Sample	Dialysis duration	Size (nm)	Zeta-potential (mV)	Conductivity (mS/cm)
1 M MgCl ₂	No dialysis	*10000	*+14	110
	3 days	590	-25	0.07
	6 days	610	-29	0.03
0.2 mM FeCl ₃	No dialysis	*10000	*+4	2.5
	3 days	570	-27	0.04
	6 days	750	-27	0.04

Stable systems are highlighted in grey.

*These are indicative values as size and measurement polydispersity too large for accurate analysis. Sizes larger than roughly 1000 nm usually indicate macroscopic aggregation in this system.

TABLE 5.2 Dynamic light scattering, zeta-potential and conductivity results of the low salt and high salt systems

Sample	Dialysis duration	Size (nm)		Zeta-potential (mV)		Conductivity (mS/cm)	
		0 days	360 days	0 days	360 days	0 days	360 days
Low salt	No dialysis	210	*4000	-37	*-25	2.20	2.4
	3 days	220	*1000	-35	*-26	0.02	0.146
	6 days	210	*1000	-38	*-24	0.02	0.085
2 M NaCl	No dialysis	*4000	*14000	-	*+8	-	163
	3 days	440	410	-	-	-	-
	6 days	360	*2000	-37	*-17	0.01	0.080

Stable systems are highlighted in grey, the only preparation route that leads to systems still stable after one year (high salt Na⁺ dialyzed for 3 days) is also highlighted in bold. Note that this behaviour has been observed in multiple samples, see FIGURE 5.4.

*Indicative values, size and measurement polydispersity too large for accurate analysis. Sizes larger than roughly 1000 nm usually indicate macroscopic aggregation in this system

have destabilized as well after one year. The results are summarized in TABLE 5.2, the only preparation route that leads to systems with long-term (more than one year) stability is indicated in bold. In general, all unstable samples had initial zeta-potentials close to -40 mV that fell below -30 mV after one year, while the stable samples started out above -50 mV and ended up above -40 mV. It is a well-known effect for electrocratic systems that the zeta-potential can change sign upon addition of background electrolyte due to specific adsorption, although this is usually found for multivalent ions [10, 11].

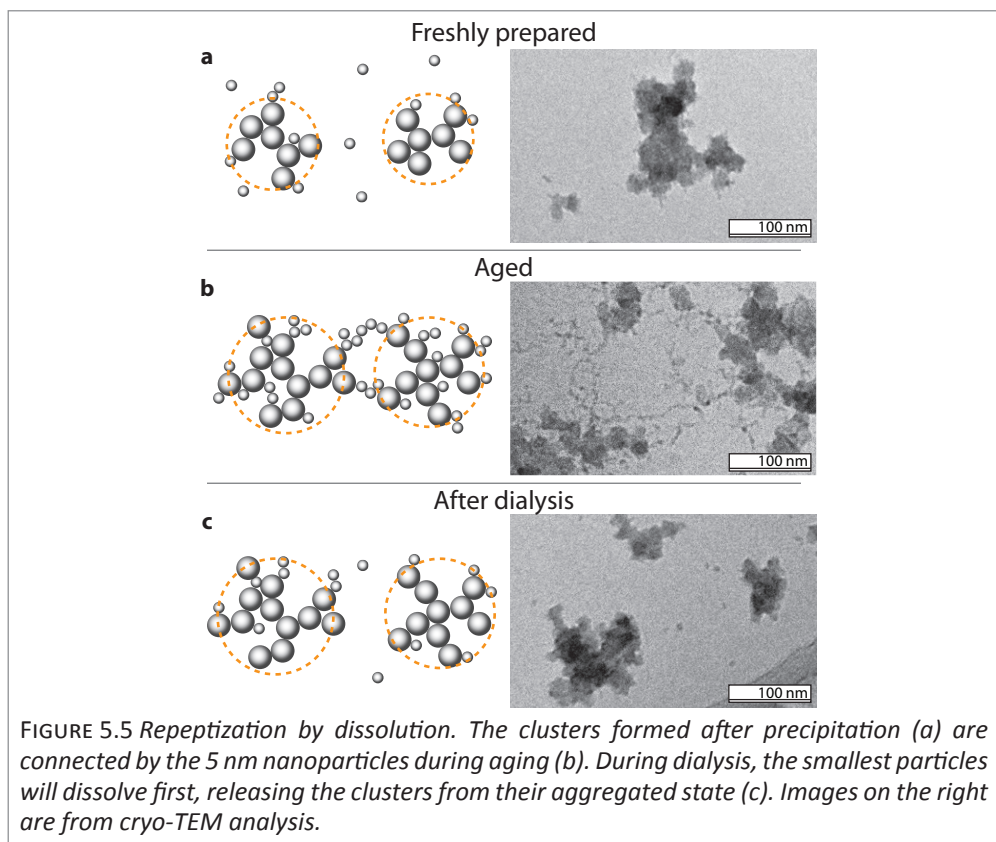
5.4 DISCUSSION

This section is divided in two parts discussing the two phenomena, as it is plausible that these are governed by separate, but related, mechanisms. These phenomena are: (I) the reeptization of aggregated iron pyrophosphate and (II) the long-term stability of the

dialyzed high salt system.

5.4.1 REPEPTIZATION

Colloidal iron pyrophosphate shows the characteristic properties for electrocratic systems like the dependence of zeta-potential on background ionic strength and excess precursor salt (see CHAPTER 4 and APPENDIX IVB). However, the reptization reported here shows some important differences with that of well-studied redispersible electrocratic systems such as the silver iodide sols [3, 12]. First of all, the iron pyrophosphate system can be reptized even after having aged for more than a month, while for most systems the possibility to reptize the system after aggregation drastically decreases over time [2, 3]. Second, colloidal iron pyrophosphate can be reptized when coagulated with multivalent ions, something which is unknown for other electrocratic systems [8, 9, 12]. This unexpected reptization of iron pyrophosphate is likely caused by the amorphous nature and open structure of the precipitate, which is observed independent of preparation method [13]. During coprecipitation of FePP_i the 5–20 nm particles immediately form ~ 200 nm clusters that slowly aggregate further until they are macroscopically large. We have proposed in CHAPTER 4 that this slow further growth occurs by connecting the smaller, 5 nm particles that have a lower stabilizing barrier. In none of our (cryo-)TEM analyses have we found that the resulting open structure of the clusters collapses completely after full aggregation and aging of the system. The smallest particles will dissolve first during dialysis (also indicated

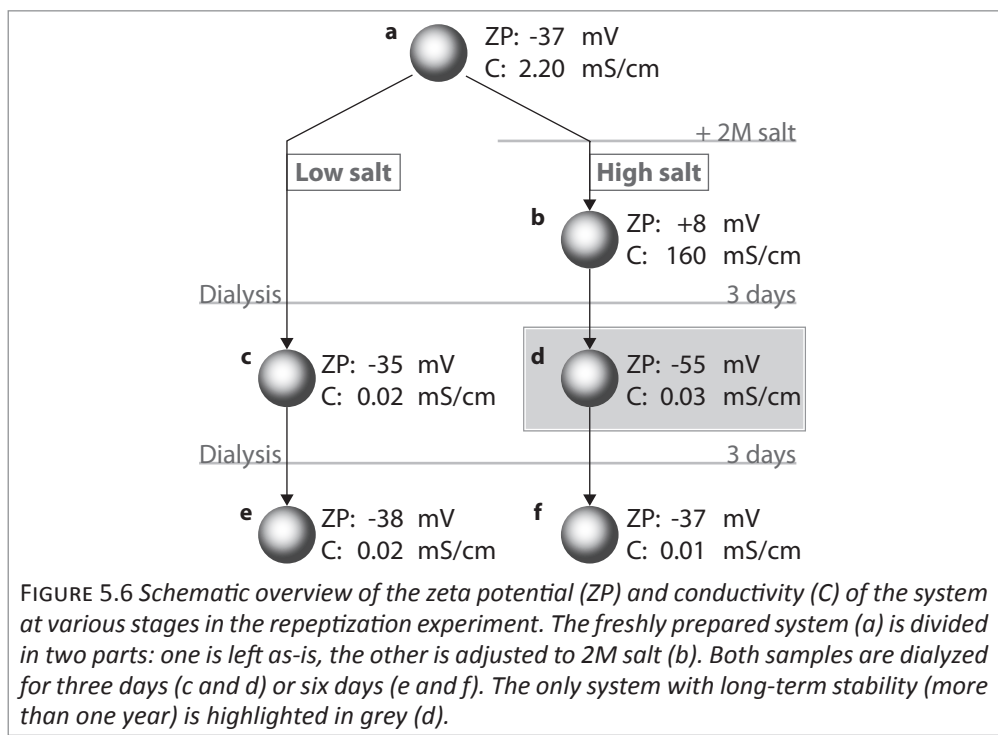


in FIGURE 5.4b and c) due to their higher solubility [11]. Also, the interactions are very short ranged as we have shown in CHAPTER 4 (>10 nm) [14]. Therefore, removing the 'linking' 5 nm particles will be sufficient to release the clusters from their aggregated state. This would avoid the need for a permanent cut-off distance that is often achieved by the addition of surfactants. The process is schematically summarized in FIGURE 5.5.

5.4.II LONG-TERM STABILITY

The results are schematically recapitulated in FIGURE 5.6, emphasizing the specific preparation route that leads to the system with long-term stability (d, highlighted in grey). The most obvious difference between the stable and unstable systems is the zeta-potential: while the potentials and conductivities of FIGURE 5.6c, e and f are equal within error limits, the potentials of c and d are very far off while they are at similar conductivity. It is not immediately clear why a system prepared in this way yields a stronger zeta-potential (d), or why it subsequently decreases again with longer dialysis time (f).

While we currently have no ready explanation for this phenomenon, the long-term stability of the high salt system dialyzed for three days is likely due to its stronger zeta-potential: it is the only system with a zeta-potential (ZP) below -50 mV. We expect that this is caused by a combination of surface effects and the slight solubility of the material (see APPENDIX II A) and we consider the following model. In this model some modification of the particle surface occurs at the highest ionic strength (FIGURE 5.6b). Possible causes for this are specific adsorption of background electrolyte, preferential dissolution of one of the components, or generation of extra surface charges facilitated by the strong screening at high ionic strength. However, in none of our previous studies have we found evidence for either specific adsorption of Cl^- ions or preferential dissolution of Fe^{3+} .



Upon dialysis (of three days), the excess electrolyte is removed but the surface remains altered with the additional charge remaining on the particle, yielding a more negative zeta-potential (comparing FIGURE 5.6c and d) and the observed long-term stability. Dialysis of another three days then etches the surface of the particles due to the slight solubility of the material, resulting in a 'clean' surface similar to the low salt system (comparing FIGURE 5.6e and f).

To identify the mechanism behind this phenomenon it would be insightful to know the exact surface composition of the particles at the various states in FIGURE 5.6. Unfortunately due to the small size of the particles and the beam-sensitivity of the material[13] we have yet to find a suitable technique to analyse this.

5.5 CONCLUSIONS

We report two findings. (1) Colloidal systems of iron pyrophosphate destabilized by addition of a large excess of salt can be repeptized by means of dialysis, independent of waiting time or concentration and valence of the excess salt. This is surprising as the system shows most of the characteristics expected for an electrocratic system and we have not seen other systems that can be repeptized from such circumstances elsewhere in literature. We argue that this unexpected repeptization can be explained by the open structure and limited solubility of the material. (2) The stability of colloidal iron pyrophosphate can be increased by the addition of salt and subsequent dialysis of the sample, but excessive dialysis of such a sample again leads to stability comparable to a system dialyzed just after preparation. This is most likely due to the complex interplay between the experimental conditions and the zeta-potential of slightly soluble materials, causing a stability optimum at a certain ionic strength and surface composition. Understanding of these two mechanisms will be helped greatly by analysis of the surface composition of the particles at various states during dissolution (for the repeptization) and at various compositions of the medium (for the long-term stability). However, due to the beam-sensitivity and small size of the particles we have yet to find a suitable analysis technique for this.

5.6 ACKNOWLEDGEMENTS

Reprinted with permission from Y.M. van Leeuwen, K.P. Velikov and W.K. Kegel, *Langmuir*, **2012**, *28*, 16531–16535. Copyright 2012 American Chemical Society.

5.7 REFERENCES

- [1] Israelachvili, J. N. In *Intermolecular & Surface Forces*; Academic Press, Inc.: 1985.
- [2] Frens, G.; Overbeek, J. T. G. Repeptization and the Theory of Electrocratic Colloids. *J. Colloid Interface Sci.* **1972**, *38*, 376-387.
- [3] Overbeek, J. T. G. Recent Developments in the Understanding of Colloid Stability. *J. Colloid Interface Sci.* **1977**, *58*, 408-422.
- [4] Desset, S.; Spalla, O.; Cabane, B. Redispersion of Alumina Particles in Water. *Langmuir* **2000**, *16*, 10495-10508.
- [5] Molina-Bolivar, J.; Galisteo-Gonzalez, F.; Hidalgo-Alvarez, R. Colloidal Aggregation in Energy Minima of Restricted Depth. *J. Chem. Phys.* **1999**, *110*, 5412-5420.
- [6] Rohrsetzer, S.; Bán, S.; Pászli, I. Colloidal Stability of Electrostatically Stabilized Sol Particles. - Part II: The Role of Hydration and the Concentration of Potential-Determining Ions in Coagulation and Peptization of Ferric Hydroxide Sols. *Colloid Polym. Sci.* **1995**,

273, 189-194.

[7] Qi, L.; Sehgal, A.; Cousin, F. Redispersible Hybrid Nanopowders: Cerium Oxide Nanoparticle Complexes with Phosphonated-PEG Oligomers. *ACS Nano* **2008**, *2*, 879-888.

[8] Poovarodom, S.; Berg, J. C. Spontaneous Repeptization of Colloidal Dispersions. *Colloids Surf. A* **2009**, *342*, 16-23.

[9] Wu, W.; Giese, R.; van Oss, C. Linkage between Sigma-Potential and Electron Donicity of Charged Polar Surfaces .2. Repeptization of Flocculation Caused by Plurivalent Counterions by Means of Complexing Agents. *Colloids Surf. A* **1994**, *89*, 253-262.

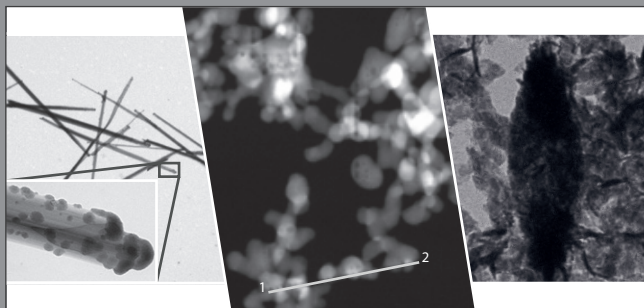
[10] Schneider, C.; Hanisch, M.; Ballauff, M. Experimental Study of Electrostatically Stabilized Colloidal Particles: Colloidal Stability and Charge Reversal. *J. Colloid Interface Sci.* **2011**, *358*, 62-67.

[11] Hunter, R. J. In *Foundations of Colloid Science*; Oxford University Press: 2001.

[12] Frens, G.; Overbeek, J. T. G. Repeptization of AgI-Flocs. *J. Colloid Interface Sci.* **1971**, *36*, 286-288.

[13] van Leeuwen, Y. M.; Velikov, K. P.; Kegel, W. K. Morphology of Colloidal Metal Pyrophosphate Salts. *RSC Adv.* **2012**, *2*, 2534-2540.

[14] van Leeuwen, Y. M.; Velikov, K. P.; Kegel, W. K. Stabilization through Precipitation in a System of Colloidal Iron(III) Pyrophosphate Salts. *J. Colloid Interface Sci.* **2012**, *38*, 43-47.



CHAPTER 6

MORPHOLOGY AND STABILITY OF MIXED-METAL PYROPHOSPHATE SALTS

In order to further reduce the reactivity of the iron in pyrophosphate salts we investigate in this chapter the preparation of mixed-metal pyrophosphates. By diluting the iron with another mineral such as calcium or magnesium we intend to lower the (surface) concentration of iron in the particles and thereby minimize its reactivity. We use two different synthesis methods to produce these materials. In the first method we introduce small amounts of a divalent metal cation (M^{II}) while preparing iron pyrophosphates by means of coprecipitation. In the second method we make use of the pH-dependent solubility of M^{II} -pyrophosphates and incorporate small amounts of Fe^{3+} . We study the resulting systems for their morphology and colloidal stability and find that stable dispersions of mixed materials can only be obtained at Fe content higher than 80 % by means of coprecipitation, or lower than 10% when using the pH-dependent precipitation method. Coprecipitated systems containing less than 80% iron and systems obtained from pH-dependent precipitation containing more than 10% iron aggregate completely upon precipitation and cannot be stabilized by means of autoclave treatment, ultrasonication or surfactant addition.

6.1 INTRODUCTION

As mentioned in CHAPTER 1, the main aim of this thesis is to decrease the reactivity of supplementary iron added to foodstuffs by embedding it in an inorganic matrix material: capturing the iron in an inorganic particle will reduce its reactivity compared to free ions in solution. It was also mentioned that introducing a second mineral could dilute the iron content at the surface of the particles and reduce the reactivity even further. Food-grade minerals that could be used in such a material are calcium and magnesium (and zinc to a lesser extent) as these are the most common dietary minerals [1]. In this respect sodium and potassium would be even more suitable, but complexes of these minerals with pyrophosphate are soluble up to high concentrations [2].

Not only could mixing minerals within a single particle reduce the reactivity of the contained iron, but combining iron with other dietary minerals in a single colloidal system would make it a multi-purpose, widely applicable delivery system for micronutrients [3].

In this chapter we will study the morphology and colloidal stability of mixed metal pyrophosphates (PP_i) containing iron(III) and a second mineral. To prepare these particles we use two approaches based on the two methods described in the first section of this thesis. In the first approach we prepare iron pyrophosphate ($FePP_i$) by using the coprecipitation method of CHAPTER 2. The second method makes use of the pH-dependent solubility of $M^{II}PP_i$ (see APPENDIX IIb) by first dissolving the material in acid and subsequently injecting it in an alkaline solution as described in CHAPTER 3. Mixed metal pyrophosphates are subsequently prepared by substituting Fe^{3+} by M^{II} in the first method, or M^{II} by Fe^{3+} in the second one.

6.2 METHODS

6.2.I MATERIALS

$CaCl_2 \cdot 2H_2O$ (ACS reagent grade, $\geq 99\%$), $Na_4P_2O_7 \cdot 10H_2O$ (ACS reagent grade), NaCl (p.a., $\geq 99.5\%$), NaOH (p.a., $\geq 99\%$) and HCl (fuming, p.a., 37% in water) were all used as obtained from Merck. $FeCl_3 \cdot 6H_2O$ (ACS reagent grade, 97%) and $ZnCl_2 \cdot 4H_2O$ (ACS reagent grade, $\geq 97\%$) were obtained from Sigma-Aldrich Chemie B.V. and $MgCl_2 \cdot 6H_2O$ (puriss. p.a., $\geq 99\%$) from Fluka Analytical (Sigma-Aldrich Chemie B.V.). All solutions were prepared in water deionized using a Millipore Synergy water purification system.

6.2.II PREPARATION

COPRECIPITATION We have shown in CHAPTER 4 that the stability of metal-pyrophosphate dispersions is strongly dependent on the ionic strength of the solution. Therefore, we prepared mixed systems at a fixed concentration of pyrophosphate as this will set the concentration of counterions. Iron pyrophosphate ($FePP_i$) was prepared by dissolving 0.857 mmol $FeCl_3$ in 50 ml water and adding this solution drop wise in about 15 minutes to 0.643 mmol $Na_4P_2O_7$ in 100 ml while stirring. A turbid white dispersion forms during the addition of the final 5 ml. Mixed systems were prepared by substituting part of the iron in the precursor solution by calcium, magnesium or zinc (together referred to as M^{II}), the amounts of Fe^{3+} and M^{II} in the mixture are then determined in stoichiometry with the concentration of PP_i . This resulted in the following Fe : M^{II} ratios: $Fe_{10}M^{II}PP_i$ (referred to as '10 : 1 ratio'), $Fe_{16}M^{II}PP_{i13}$ ('8 : 1'), $Fe_8M^{II}PP_{i7}$ ('4 : 1'), $Fe_4M^{II}PP_{i5}$ ('1 : 1'), $Fe_2M^{II}PP_{i7}$ ('1 : 5') or $Fe_2M^{II}PP_{i11}$ ('1 : 10'). Here we assumed complete precipitation without inclusion of the Na^+ and Cl^- from the reactants. Full substitution of iron results in the pure M^{II} pyrophosphate, $M^{II}PP_i$. For Fe : Na, the following ratios were prepared: $Fe_{22}Na_2PP_{i17}$ ('10 : 1'),

$\text{Fe}_{32}\text{Na}_4\text{PP}_{i25}$ ('8 : 1'), $\text{Fe}_{16}\text{Na}_4\text{PP}_{i13}$ ('4 : 1'), samples containing lower iron content remained clear and no particles were formed. All samples were stored in plastic (Teflon) bottles. Iron pyrophosphate prepared without any substitution will be referred to as 'pure FePP_i '.

pH-DEPENDENT PRECIPITATION As we have shown in CHAPTER 2, we have been unable to prepare stable colloidal dispersions of $\text{M}^{\text{II}}\text{PP}_i$ when using the coprecipitation method. Therefore, we have developed a two-step method that makes use of the pH-dependent solubility of metal-pyrophosphates as described in CHAPTER 3, partially based on the method described by Groves *et al.* [4]. **Intermediate:** 50 mL 1 M $\text{M}^{\text{II}}\text{Cl}_2$ solution was added drop wise in one hour to 800 mL 0.0625 M sodium pyrophosphate solution while stirring with a magnetic stirrer. The resulting white suspension was washed three times with water and twice with acetone, after which the precipitate was dried in an oven at 37°C for two days. Similar to the coprecipitation method, mixed intermediates were prepared by substituting part of the M^{II} by Fe^{III} while keeping the concentration of PP_i constant. This resulted in the following Fe : Mg ratios: $\text{Fe}_2\text{M}^{\text{II}}_{19}\text{PP}_{i11}$ ('1 : 10'), $\text{Fe}_2\text{M}^{\text{II}}_{39}\text{PP}_{i21}$ ('1 : 20'), $\text{Fe}_2\text{M}^{\text{II}}_{99}\text{PP}_{i51}$ ('1 : 50') and $\text{Fe}_2\text{M}^{\text{II}}_{199}\text{PP}_{i101}$ ('1 : 100'). **Product:** 0.56 g intermediate was dissolved in 15 mL 1 M HCl and filtered over a Minisart disposable cellulose acetate filter (0.2 μm pore size, 16534-K). Using a syringe, the solution is injected into 35 mL 0.39 M NaOH solution while stirring vigorously with a magnetic stirrer. The resulting turbid white dispersion was stirred for another 10 minutes after injection (final pH is 7) and subsequently washed twice by centrifugation and redispersed in a final volume of 50 mL water.



6.2.III ANALYSIS

Dynamic Light Scattering (DLS) and electrophoretic mobility measurements were performed using a Malvern Instruments Zetasizer Nano series machine operating in backscatter mode at 25°C with 5 minutes equilibration time. Samples for time-dependent DLS measurements (data in FIGURE 6.2) were prepared by filtering 3 ml of the stock samples through a Minisart disposable cellulose acetate filter (0.45 μm poresize, 16555-K) and storing them in a plastic disposable DLS cuvette. The cuvettes were subsequently sealed using parafilm. Samples for electrophoretic mobility measurements were taken from the stock sample. DLS analysis showed no significant difference between the stock and sealed samples during aging. For transmission electron microscopy (TEM) and Energy-dispersive X-ray spectroscopy (EDX), dispersions were diluted 10 times and dried on a polymer-film coated copper grid prior to analysis using a Tecnai 12 and 20 electron microscope from FEI Company, respectively. XRD measurements were carried out on a Bruker-AXS D8 Advance powder X-ray diffractometer in Bragg-Brentano mode equipped with automatic divergence slit (0.6 mm 0.3°) and a PSD Vântec-1 detector. The radiation used was Cobalt $\text{K}\alpha_{1,2}$, $\lambda = 1.79026 \text{ \AA}$, operated at 30kV, 45 mA.

6.3 RESULTS

6.3.I COPRECIPITATION METHOD

MORPHOLOGY Using the coprecipitation method we have prepared a series of iron pyrophosphates in which part of the iron(III) was substituted with another mineral (Ca^{2+} , Mg^{2+} or Na^+) while maintaining overall charge balance with the pyrophosphate. This yielded molar Fe: M^{II} ratios ranging from 10:1 to 1:10. For instance, the 'Ca 10:1 ratio' refers to the mixture in which the molar ratio between Fe^{3+} , Ca^{2+} and PP_i^{4-} was chosen such that it resulted in the charge-neutral stoichiometric composition $\text{Fe}_{10}\text{Ca}(\text{PP}_i)_8$, assuming that all material precipitates without inclusion of Na^+ and Cl^- . See the Methods section for details.

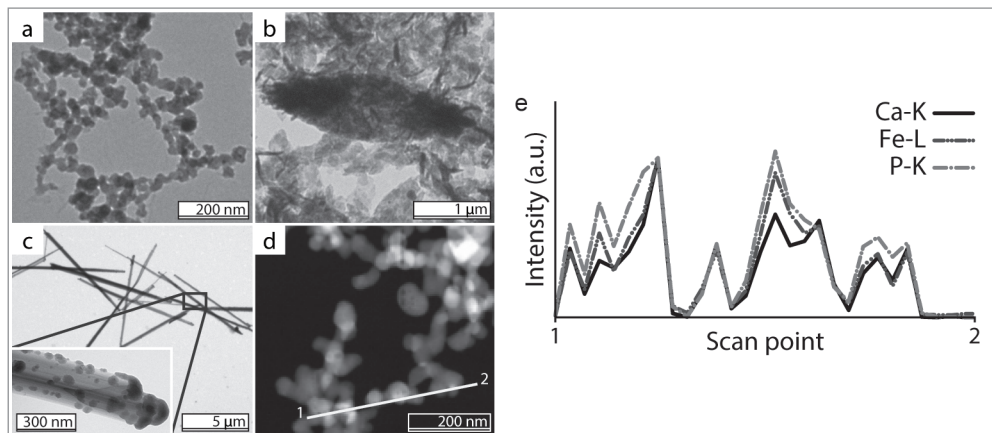


FIGURE 6.1 Morphology of mixed metal pyrophosphates resembles that of $M^{II}PP_i$ found in CHAPTER 2, as shown here for Fe:Ca 1:10 (a). The mixed ratios of 1:5 and higher in M^{II} content show different morphology, two representative TEM-images are given: Fe:Zn 1:5 (b) and Fe:Mg 1:10 (c). Dark-field TEM image of Fe:Ca 1:10 ratio (d) shows the position of the EDX scan line (scan direction from 1 to 2). The normalized intensities (e) show a uniform material distribution throughout the material.

Most resulting precipitates were similar to the particles obtained preparing the pure MPP_i of the cation in excess: at high iron(III) content the particles were similar to the amorphous clusters observed in CHAPTER 2, see FIGURE 6.1a. At Fe:Mg and Fe:Zn ratios of 1:5 and higher in M^{II} content other morphologies started to appear. In case of $FeZnPP_i$ rough, irregular platelets and elliptical shapes were found, see FIGURE 6.1b. For $FeMgPP_i$ needle-like particles were formed resembling those seen in CHAPTER 2 although some demixing seems to occur: smaller, roughly 20 nm particles which are expected to be $FePP_i$ can be seen on the surface of the needles, see FIGURE 6.1c. XRD analysis of the Fe:Ca 10:1 material showed it to be as amorphous as the $FePP_i$ (results not shown). Analysis of material composition using EDX corresponds to what was added during preparation only with slight excess of PP_i (most likely compensated with H^+ that cannot be analyzed using EDX). Line scans indicated homogeneous composition of the amorphous nanoparticles (on the resolution of the analysis method); FIGURE 6.1d and e shows that the normalized intensities follow each other closely.

STABILITY Samples with ratios of 1:1 and lower in Fe^{3+} formed particles that were too large to remain in dispersion after preparation as could already be deduced from TEM analysis (FIGURE 6.1), but the 10:1, 8:1 and 4:1 ratio systems all resulted in initially stable dispersions. The size of the clusters in these samples was followed over time using dynamic light scattering and the results are summarized in FIGURE 6.2. It should again be noted that due to the system's aggregated nature, the polydispersity of the 'stable' systems is still significant (>30%). Sizes are therefore not interpreted as absolute figures but only as trends.

Analogous to what we observed in CHAPTER 4, the size of the cluster grew over time while no change was seen in cryo-TEM analysis (not shown). It is interesting to note that most samples showed an initial period during which there was little to no change in cluster size. The duration of this period of relative stability was clearly influenced by the cation: Ca^{2+} substituted systems destabilized within days while Na^+ substituted systems remained stable for over three months. There appears to be no specific order in the effect of the

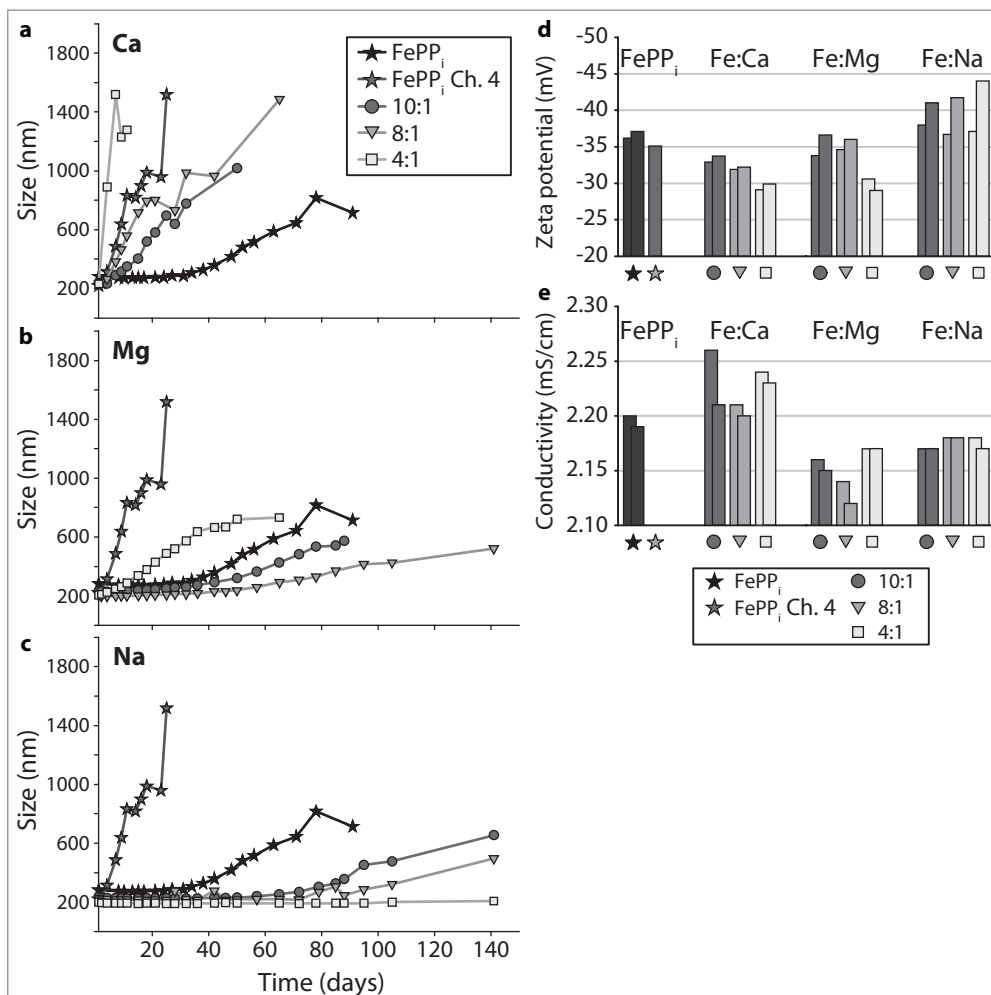


FIGURE 6.2 (a-c) Growth of cluster size over time as analyzed by dynamic light scattering for systems prepared by coprecipitation containing different ratios of metal pyrophosphates. Calcium (a), magnesium (b) and sodium (c) systems with Fe:M^{II} ratios of 10:1 (dark grey squares), 8:1 (diamonds) and 4:1 (triangles). A new pure FePP_i sample and the sample from CHAPTER 4 are shown for reference (dark and light stars, respectively). Zeta potential (d) and conductivity (e) analysis of the same systems. Two bars per sample: fresh (left, back) and after one month (right, front).

substitution ratio as the stability varies per substituting metal, see FIGURE 6.2a-c.

It can be seen from FIGURE 6.2d and e that all systems had similar zeta-potentials while the magnesium and sodium containing samples had slightly lower conductivity. As mentioned in the Methods section we prepared all systems at the same concentration of PP_i to ensure that the (initial) concentration of counterions is the same for all systems. The different conductivity of the resulting systems could cause the instability of the calcium substituted systems: a lower zeta-potential with a higher conductivity might result in an insufficiently high stabilizing barrier in the interaction potential (see CHAPTER 4 and APPENDIX IIIb for discussion and calculations regarding interaction potentials). Similarly, the higher

zeta-potential together with the lower conductivity could cause the increased stability of the Na-substituted systems.

The higher conductivity of CaPP_i (and thus higher ionic strength [5]) compared to the MgPP_i might indicate a difference in solubility between these materials. The resulting higher ionic strength could explain the decreased dispersion stability. The difference in solubility seems to be confirmed by literature [6], but we were unable to find reliable data on MgPP_i solubility [7] and no data on solubility of mixed systems whatsoever.

That the sodium and magnesium substituted systems remained stable for longer period of time than the pure FePP_i is surprising, but could be related to the discussion in CHAPTER 5; substitution with another mineral might lead to different surface composition and ionic strength (through solubility), resulting in the observed differences in zeta-potential and dispersion stability.

Finally, there is a clear difference between the pure FePP_i sample from CHAPTER 4 and the one prepared here (light and dark grey stars in FIGURE 6.2a-c, respectively): the previous sample immediately starts to grow after preparation while the current system shows no growth for up to 20 days. Unfortunately, we did not measure the conductivity or final zeta-potential of the previous sample, as this might have been influenced by the slightly different preparation method and the storage in a glass bottle instead of a plastic one. While the previous sample consists of somewhat smaller clusters, cluster size does not affect the zeta-potential as we show in APPENDIX 1b.

6.3.II pH-DEPENDENT PRECIPITATION METHOD

MORPHOLOGY Using the pH-dependent precipitation method we have prepared FeMgPP_i systems at Fe:Mg ratios of 1:10, 1:20, 1:50 and 1:100. TEM analysis of the 1:100 and 1:50 mixed systems showed similar particles to the pure MgPP_i found in CHAPTER 3: small, irregular platelets of about 20 nm, see FIGURE 6.3a and b. At higher Fe^{3+} content the particles became less well-defined and were also much more beam-sensitive as it was impossible to image the individual particles before they melted, see FIGURE 6.3c.

Surprisingly, XRD analysis indicated that the 1:10 ratio system was more crystalline than the other systems: FIGURE 6.4 shows sharper peaks and a lower signal-to-noise ratio for that particular system. Furthermore, there is no agreement in peak position between the 1:10 ratio sample and the other two systems. However, the systems prepared here do show agreement with the XRD patterns from CHAPTER 2: the pure MgPP_i prepared here corresponds to the SDS-containing sample of CHAPTER 2, while the 1:10 sample has peak positions similar to the pure MgPP_i prepared by coprecipitation, see FIGURE 6.4b. As mentioned before, there is no correspondence to reference patterns found in literature.

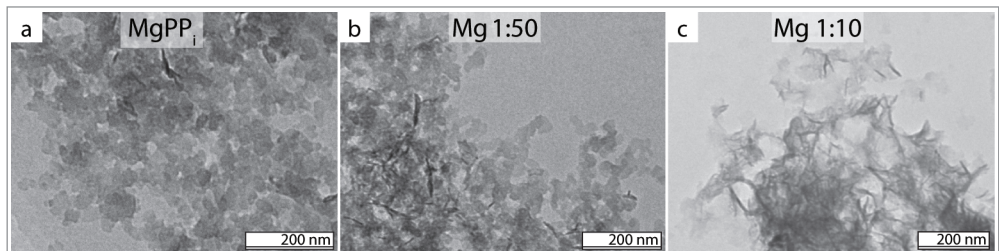


FIGURE 6.3 TEM images of the mixed Mg systems prepared by the pH-dependent precipitation method: (a) Pure MgPP_i , (b) an Fe:Mg 1:50 mixed system and (c) an Fe:Mg 1:10 system.

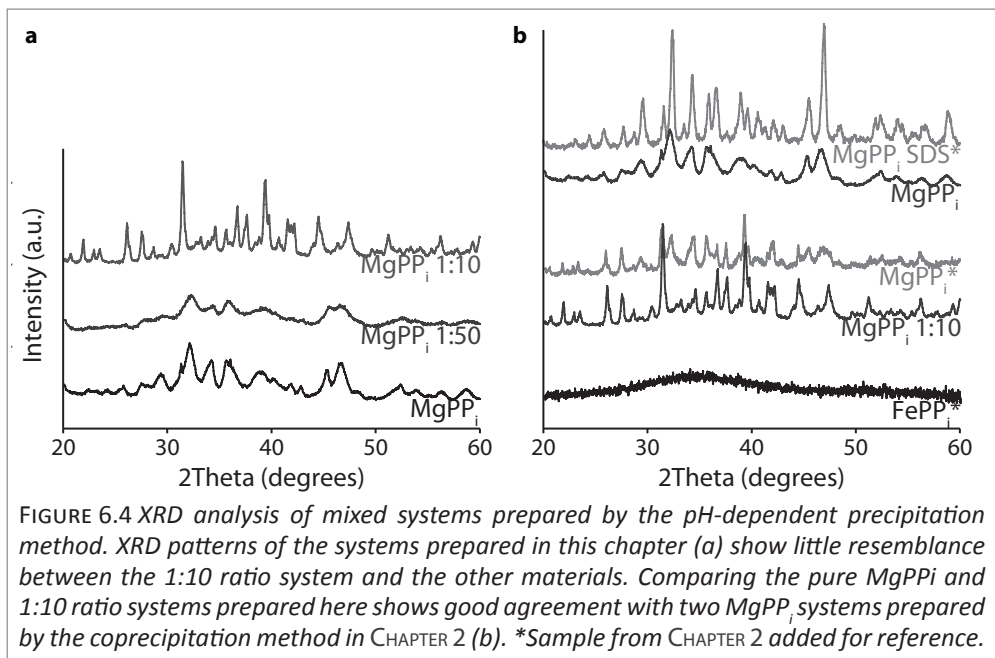


FIGURE 6.4 XRD analysis of mixed systems prepared by the pH-dependent precipitation method. XRD patterns of the systems prepared in this chapter (a) show little resemblance between the 1:10 ratio system and the other materials. Comparing the pure MgPP_i and 1:10 ratio systems prepared here shows good agreement with two MgPP_i systems prepared by the coprecipitation method in CHAPTER 2 (b). *Sample from CHAPTER 2 added for reference.

Elemental analysis using EDX shows good agreement with what was added during preparation for the Mg 1:50 system, but the pure MgPP_i and 1:10 systems deviate significantly: while the intended MgFe_{0.1}PP_{10.6} resulted in MgH_{9.5}Fe_{0.5}PP₁₃ for the 1:10 system, the pure MgPP_i resulted in MgH₁₄PP₁₄ instead of Mg₂PP_i. EDX analysis indicated no significant inclusion of Na⁺ or Cl⁻. The crystallinity of the 1:10 system could explain this divergence as this ratio might form a charge neutral unit cell more easily. That the pure MgPP_i sample deviates so much but does not result in a crystalline material is then unexpected, especially considering the agreement in XRD-patterns between the pure MgPP_i and the 1:50 mixed system.

For Ca and Zn, no stable dispersions of mixed-metal pyrophosphates could be obtained; all particles resembled those found for pure M^{II}PP_is as described in CHAPTER 3 (not shown) and the stability could not be improved by further washing steps or the addition of surfactants.

STABILITY The DLS results also showed a difference between samples with higher and lower Fe³⁺ content: Fe:Mg samples with iron content of 1:50 or lower yielded stable dispersions with cluster sizes of around 200 nm, while at higher concentrations the cluster sizes were much larger, see TABLE 6.1. The stability of the particles is therefore linked to the degree of crystallinity as we have also found in CHAPTER 2: only the largely amorphous systems of metal-pyrophosphates lead to stable colloidal dispersions.

The samples that were stable after preparation remained in dispersion for months before further aggregation began as was shown in CHAPTER 3. Careful examination of the influence of washing steps on the stability of the samples showed a strong relationship between conductivity, zeta-potential and particle size, see FIGURE 6.5. There clearly was a stability optimum at a conductivity between 1.2 and 0.2 mS/cm, as this yielded a zeta-potential of -45 mV and a cluster size of around 200 nm. Both higher and lower conductivities resulted in large aggregates that precipitated completely within minutes. This shows that not only

TABLE 6.1 DLS and electrophoretic mobility analysis of Mg containing systems

	Ratio	Size (nm)	ZP (mV)	Conductivity (mS/cm)
MgPP _i	-	150	-40	0.92
Fe : Mg	1 : 10	*3800	-39	0.01
	1 : 20	*2800	-29	0.06
	1 : 50	270	-35	0.14
	1 : 100	260	-33	0.06

*Indicative values, samples too aggregated for accurate analysis.

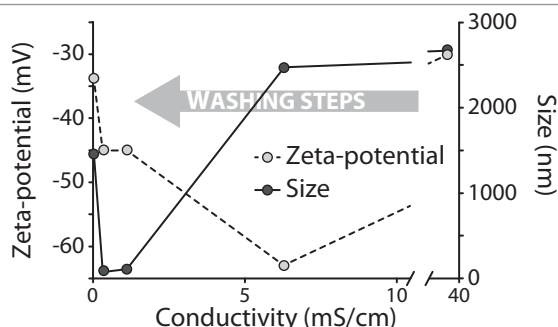


FIGURE 6.5 Following a sample of pure MgPP_i through several washing steps shows that there is an optimum in conductivity (between 1.2 and 0.2 mS/cm) that yields a zeta-potential below 40 mV and a cluster size of around 200 nm (b). The system at lowest ionic strength (0.079 mS/cm) is unstable as well. Largest cluster sizes are indicative: sizes greater than roughly 1000 nm usually indicate macroscopic aggregation in these systems. Arrow indicates direction of washing steps.

a system with too high ionic strength is unstable, but a system with too low ionic strength as well indicating that these systems can be washed 'too much'. This bears similarity to the results of CHAPTER 5, where we found that only systems with a conductivity close to 0.1 mS/cm and a zeta-potential higher than -50 mV (i.e. more negative values) remained stable for more than a year. It is therefore most likely caused by similar surface effects that were mentioned in that chapter. Also note in this respect that during the washing steps, FIGURE 6.5b shows that the zeta-potential first went through a lower value (-60 mV) before reaching the stable state, possibly indicating the surface modification by dissolution that was discussed in CHAPTER 5.

6.4 CONCLUSIONS

We have successfully prepared stable dispersions of mixed-metal pyrophosphate salts containing various ratios of Fe:M^{II} using two different preparation methods. Stable dispersions with high concentrations of iron (ratios up to 4:1) were prepared using the coprecipitation method, while stable particles containing excess M^{II} (1:50 and 1:100) have been prepared by the pH-dependent precipitation method. When preparing systems using the coprecipitation method we find that the substituting cation strongly influences the colloidal stability of the dispersion, with Ca²⁺ resulting in the least stable systems

and Na^+ the most stable dispersions. With the pH-dependent precipitation method we could only prepare stable (mixed) systems if they contained Mg^{2+} . We show that there is an optimum ionic strength for dispersion stability as a conductivity above 1.2 mS/cm or below 0.2 mS/cm will result in completely aggregated systems, indicating that excessive washing actually destabilizes the particles. These results are likely caused by a correlation between surface composition and ionic strength similar to what we have described in CHAPTER 5, but the exact origins of these effects are still unknown. Both methods show that the samples with the lowest crystallinity result in the most stable dispersions.

6.5 ACKNOWLEDGEMENTS

We thank Jenneke Pandelaar for preparing the systems using the pH-dependent precipitation method and J.D. Meeldijk of the Electron Microscopy group for EDX analysis. We also thank M. Versluijs-Helder of the Inorganic Chemistry and Catalysis group at the University of Utrecht for performing XRD measurements.

6.6 REFERENCES

- [1] Wakimoto, P.; Block, G. Dietary Intake, Dietary Patterns, and Changes with Age: An Epidemiological Perspective. *Journals of Gerontology - Series A Biological Sciences and Medical Sciences* **2001**, *56*, 65-80.
- [2] Haynes, W. M. In *Handbook of Chemistry and Physics*; Lide, D. R., Ed.; CRC Press: Boca Raton, FL, 2011.
- [3] Mehansho, H.; Mellican, R. I.; Walter, T. Multiple-Micronutrient Fortification Technology Development and Evaluation: From Lab to Market. *Food Nutr. Bull.* **2003**, *24*, S111-S119.
- [4] Groves, P. J.; Wilson, R. M.; Shellis, R. P. Synthesis of Triclinic Calcium Pyrophosphate Crystals. *J. Mater. Sci. Mater. Med.* **2007**, *18*, 1355-1360.
- [5] McCleskey, R. B. Electrical Conductivity of Electrolytes found in Natural Waters from (5 to 90) °c. *J. Chem. Eng. Data* **2011**, *56*, 317-327.
- [6] Bennett, R. M.; Lehr, J. R.; McCarty, D. J. Factors Affecting the Solubility of Calcium Pyrophosphate Dihydrate Crystals. *J. Clin. Invest.* **1975**, *56*, 1571-1579.
- [7] Nanbu, H. Mineral Composition. *European Patent Application* **1998**, EP0870435.

SECTION 3

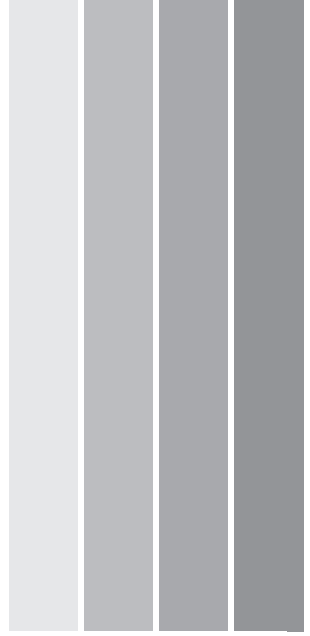
A GENERAL PREPARATION METHOD FOR BIOCOMPATIBLE COM

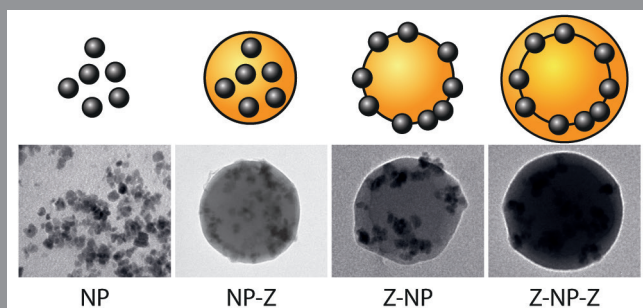
REACTI

POSITE NANOPARTICLES

VITY OF COLLOIDAL IRON-CONTAINING PYROPHOSPHATE SALTS

APPLICATIONS





CHAPTER 7

A GENERAL PREPARATION METHOD FOR BIOCOMPATIBLE COMPOSITE NANOPARTICLES

We present a general and reproducible method to prepare biocompatible composite nanomaterials in aqueous media. The method comprises the heterocoagulation of negatively charged nanoparticles with the positively charged zein protein without employing any further additives. We demonstrate that composites can be obtained with three different morphologies and that each morphology can be prepared using nanoparticles of various size, shape and material. All resulting composite particles have a net positive charge, including the morphology where nanoparticles cover the outer surface of the zein protein spheres. An important feature of our composites is that nanoparticles combined with zein have long-term stability in water, even when the free nanoparticles in absence of zein completely aggregate within days.

7.1 INTRODUCTION

Composite nanoparticles are of great interest because combining multiple materials in a single particle can have various advantages, such as decreased reactivity [1], increased stability [2], combined properties (such as magnetic or optic) within a single system [3] or the specific, targeted interactions that are useful for medical imaging [4] or drug delivery [5]. However, most of the currently available preparation methods are laborious, require expensive materials or equipment, and lack general applicability as they are designed for one specific material or morphology [6-8].

Here we present a general, reproducible method to prepare biocompatible core-shell particles with adjustable morphology and core content using the zein protein as matrix material. Zein, a seed storage protein obtained from corn and belonging to the prolamine class of proteins, is insoluble in water and rich in the amino acids glutamic acid, leucine, proline and alanine but deficient in basic and acidic amino acids. The 44 kDa zein protein is actually a mixture of peptides of different size, charge and solubility that occurs as a heterogeneous mixture of disulfide-linked aggregates in whole corn [9].

Zein is currently mainly used as adhesive, binder material and coating in foodstuffs, but has also been proposed as a potential biomaterial for delivery systems [10, 11]. Combining the protein with various (nano)materials into a single composite system will add functionality to the current applications of zein as well as generate new ones. For instance, incorporating magnetic and/or optically active materials may result in particles applicable in medical imaging or (targeted) drug delivery.

As the heterocoagulation used in our method is based on Coulombic attraction between the nanoparticles and the zein protein, any negatively charged nanoparticle, in principle, is able to form a composite material with the positively charged zein. To demonstrate this generality, we prepare composite systems with several types of nanoparticle with different (surface) properties but all having a negative surface charge.

Among the nanoparticles (NP) we use is iron(III) pyrophosphate (FePP₂), the only white iron-containing material. It is commercially available as food additive because of its good bioavailability [12] and the fact that a white material is easily concealed in foodstuffs. This application of iron pyrophosphate would greatly benefit from a colloidal preparation method [13], but unfortunately all previous attempts towards such a method have resulted in inherently unstable systems of amorphous nanoparticles as we have shown in CHAPTER 2 [14]. The complete aggregation that occurs within days in these systems can be delayed for weeks to months only at very low ionic strengths, which is unpractical especially in view of the intended applications. Other methods of stabilization such as the addition of surfactants are often either very expensive or unsuitable for nutritional applications [15].

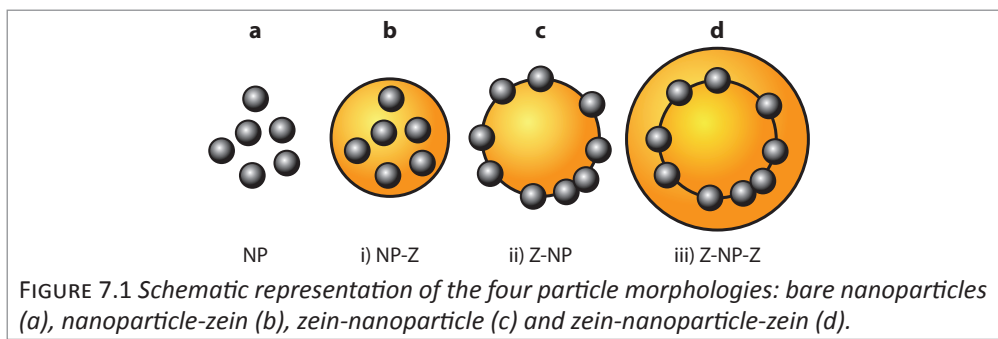


FIGURE 7.1 Schematic representation of the four particle morphologies: bare nanoparticles (a), nanoparticle-zein (b), zein-nanoparticle (c) and zein-nanoparticle-zein (d).

Here we demonstrate that the preparation of a composite material consisting of zein and FePP_i results in a fully biocompatible system that remains in dispersion for months, even without using purification steps such as centrifugation or dialysis.

Besides iron(III) pyrophosphate, five other types of nanoparticle were used in the preparation of the composite systems: magnetite (Mag), cobalt ferrite (CoFe), gold (Au), silver (Ag) and anisotropic hematite spindles (Hem). Three composite morphologies (schematically represented in FIGURE 7.1) were prepared using these nanomaterials: i) NP-Z: zein spheres with a homogeneous distribution of nanoparticles, ii) Z-NP: zein spheres with a surface coverage of nanoparticles and iii) Z-NP-Z: these consist of Z-NP particles covered with an additional layer of zein, see for a schematic representation. Specific composite systems will be referred to by substituting the nanoparticle material abbreviation into the name of the system (e.g. Hem-Z, Z-Mag, Z-Au-Z).

7.2 MATERIALS

Chemicals were obtained from the following suppliers: urea (ACS, 99%) and AgNO₃ (ACS, 99.9%) from Brunschwig Chemie B.V., tetramethylammonium hydroxide solution (TMAH, 25 wt. % in water), NaH₂PO₄ (purum p.a., ≥99.0% (T)) and CoCl₂·6H₂O (purum, ≥98.0% (KT)) from Fluka Analytical (Sima-Aldrich Chemie B.V.), NaBH₄ (reagent grade, ≥98.5%), zein protein, Fe(CIO₄)₃·6H₂O (crystalline), FeCl₃·6H₂O (ACS reagent grade, 97%), FeCl₂·4H₂O (98%) and AuCl₄H.aq (puriss. p.a.) from Sigma-Aldrich Chemie B.V., ethanol 100% from Interchema, Na₄P₂O₇·10H₂O (ACS reagent grade), trisodium citrate dihydrate (crystalline) and HCl (fuming 37%) from Merck. All chemicals were used as received. All water used in this work has been deionized by a Millipore Synergy water purification system.

7.3 NANOPARTICLE PREPARATION

ZEIN. Colloidal zein was prepared by antisolvent precipitation [16]. Typically, 1 gram of zein powder was added to 40 ml of a 80:20 v/v ethanol:water mixture and stirred for 10 minutes. The zein solution was then slowly poured into 120 ml pure water while stirring upon which a yellow, turbid dispersion was formed. While the ethanol can be removed from the mixture by using a rotary evaporator, this method was not used for the experiments described in the current work.

IRON PYROPHOSPHATE. As colloidal iron pyrophosphate aggregates over time in water as we have shown in CHAPTER 4 [17], the nanoparticles were prepared immediately before the zein precipitation. Iron pyrophosphate nanoparticles were prepared by coprecipitation of Na₄P₂O₇ with FeCl₃. 0.86 mmol iron chloride dissolved in 50 ml water was added drop wise in about 15 minutes to 0.64 mmol sodium pyrophosphate in 100 ml. A turbid white precipitate formed in the final 5 minutes of the addition (pH 4).

MAGNETITE (Fe₃O₄) nanoparticles were prepared by the coprecipitation method described by Massart *et al.* and stabilized by TMAH [18]. In a typical preparation, 0.02 mol FeCl₂ was dissolved in 10 ml of 2 M hydrochloric acid and mixed with 0.04 mol FeCl₃ in 40 ml of water. The mixture was ultrasonicated briefly and added to 500 ml 0.7 M ammonia while stirring vigorously. The solution turns black immediately and stirring is continued for another 10 minutes. The particles were precipitated on a magnet, redispersed in 50 ml 1 M TMAH and stirred overnight. Next, the particles were precipitated again and redispersed in water to remove the excess TMAH.

COBALT FERRITE (CoFe₂O₄) nanoparticles were prepared following the co-precipitation method described by Claesson *et al* [19], based on the method developed by Tourinho

et al [20]. In a typical preparation, 0.01 mol CoCl_2 dissolved in 5 ml 2.4 M HCl solution, and 0.02 mol FeCl_3 dissolved in 40 ml water were heated to 50°C and mixed. They were then immediately added to 200 ml boiling 1 M NaOH while stirring vigorously. After 30 min of stirring at 100°C , the black mixture was cooled to room temperature, the particles were washed four times with 100 ml water and then redispersed in 30 ml 2M HNO_3 . To this dispersion, 30 ml 0.35 M $\text{Fe}(\text{NO}_3)_3$ was added and heated to 100°C , at which it was kept for 45 minutes. After cooling to room temperature the particles were sedimented on a magnet, redispersed in 50 ml 1 M TMAH and stirred overnight. Finally they were redispersed in 50 ml water.

HEMATITE ($\alpha\text{-Fe}_2\text{O}_3$) spindles were prepared by the method described by Ocaña *et al* [21, 22]. 0.1 mol $\text{Fe}(\text{ClO}_4)_3$, 0.1 mol urea and 0.004 mol NaH_2PO_4 were dissolved in 200 ml water and aged for 24 hours at 100°C . The dispersion was cleaned by centrifugation and redispersion in water, followed by redispersion in 1 M TMAH and another washing step with water.

GOLD nanoparticles were prepared as citrate coated gold as described by Pérez-Juste *et al* [23]. In a typical preparation, a 20 ml aqueous solution containing $1.25 \cdot 10^{-4}$ M HAuCl_4 and $2.5 \cdot 10^{-4}$ M trisodium citrate was prepared. To this, 0.3 ml freshly prepared, ice cold 0.01 M NaBH_4 solution was added while stirring vigorously. The reaction was completed by storing the dispersion for 15 minutes at 40°C .

SILVER nanoparticles were prepared by reducing the silver salt with citrate in water at reflux temperature [24]. 52 ml AgNO_3 solution (0.769 mM) was heated to reflux, after which 4 ml 1 wt. % trisodium citrate solution was added. The reaction was completed at reflux for one hour, during which a turbid grey/yellow dispersion formed.

7.3.I COMPOSITE NANOPARTICLES CONTAINING IRON PYROPHOSPHATE NANOPARTICLES

As mentioned, due to the instability of colloidal FePP_i the nanoparticles were prepared either immediately before (in case of the NP-Z system), or simultaneously with the zein precipitation

FePP_i-Z. After complete precipitation of the iron pyrophosphate, 30 ml dispersion was removed and 40 ml zein solution (1 g zein in 80 vol. % ethanol) was slowly poured into the dispersion, which turned more turbid and slightly yellow. Some aggregates were formed, which were filtered out of the dispersion before further analysis.

Z-FePP_i. 40 ml zein solution (0.5 g in 80 vol. % ethanol) was slowly poured into 120 ml water. To the resulting turbid yellow dispersion, 0.21 mmol $\text{Na}_4\text{P}_2\text{O}_7$ in 5 ml water was added, immediately followed by 0.29 mmol FeCl_3 in 5 ml water. The dispersion slowly turned more turbid.

Z-FePP_i-Z. The Z-NP dispersion was stirred for 5 minutes after complete addition of the Fe solution, after which another 40 ml zein solution (0.5 g in 80 vol. % ethanol) was poured into the dispersion.

7.3.II COMPOSITE NANOPARTICLES CONTAINING MAG, COFE, HEM, AU OR AG NANOPARTICLES

These materials did not need to be freshly prepared as they can be stored in water for longer periods of time.

NP-Z. The nanoparticle dispersions were diluted to 120 ml, this final volume containing the following weight percentages of nanoparticles: magnetite and cobalt ferrite 0.3 wt. % (pH 8 and 7, respectively), hematite 0.03 wt. % (pH 7). Composites containing silver and gold were prepared at smaller volumes, see below. While stirring, 40 ml zein solution (1 g

zein in 80 vol. % ethanol) was poured into the dispersion. The dispersions were stirred for another 5 minutes after complete addition.

Z-NP. 40 ml zein solution (0.5 g zein in 80 vol. % ethanol) was poured into 80 ml water while stirring. After complete addition, the same amount of NP dispersion that was added to the NP-Z system, was added to the dispersion (resulting in the same final wt. % of nanoparticles in the Z-NP-Z system).

Z-NP-Z. Immediately after the NP addition in the preparation of Z-NP, another 40 ml zein solution (0.5 g zein in 80 vol. % ethanol) was added to the dispersion. The dispersion was stirred for another 10 minutes after complete addition. Composite particles containing magnetic materials were purified by allowing the dispersion to sediment next to a magnet for 24 hours, decanting the turbid supernatant and redispersing the dark brown sediment in water. Composite materials containing gold or silver were prepared using the same methods described above, but at 10 times smaller volumes and with concentrations of 0.003 wt. % (pH 5) and 0.008 wt. % (pH 5) for gold and silver, respectively. Due to the large size of the nanoparticles, silver and hematite composites were only prepared as NP and NP-Z systems. All resulting composite systems have a pH of 4, independent of the pH of the type of nanoparticle used.

7.4 ANALYSIS

Dynamic Light Scattering (DLS) and electrophoretic mobility measurements were performed using a Malvern Instruments Zetasizer Nano series machine in backscatter mode at 25°C with 5 minutes of equilibration time. Samples were filtered and then diluted ten times before analysis. The DLS measurements were performed in ten runs of 15 measurements per run, electrophoretic measurements used ten runs of 50 measurements. For transmission electron microscopy (TEM), dispersions were diluted roughly 100 times and dried on a copper grid prior to analysis using a Tecnai 12 electron microscope from FEI Company.

7.5 RESULTS

7.5.1 TEM

As is shown in FIGURE 7.2, we have successfully prepared each composite morphology with each type of nanoparticle. Silver and hematite composite materials were only prepared as NP and NP-Z systems due to the large size of the nanoparticles. The only system for which separate nanoparticles were still found were the gold-containing Z-Au and Z-Au-Z systems. While TEM images show that while the majority of the gold nanoparticles were attached to the zein, we also found individual NPs and empty zein particles, see the inset of FIGURE 7.2o. The coverage of the Z-Au en Z-Au-Z systems with nanoparticles was also lower than for the other nanoparticles. Centrifugation of the Au dispersions confirmed this: the supernatant of Z-Au remained pink and contained individual gold nanoparticles, see FIGURE 7.3. That the TEM images of some systems do not resemble their corresponding schematic representation is due to a combination of drying effects and the fact that these images are a two-dimensional representation of a three-dimensional object. This is confirmed by preliminary TEM-tomography experiments that have been performed and which are described in APPENDIX V.

Empty zein particles were found in most of the samples (not shown). While the fraction of empty zein particles (i.e. zein particles that did not contain nanoparticles) seemed to be less for the Z-NP-Z than for the NP-Z systems, the NP-Z particles that did contain nanoparticles

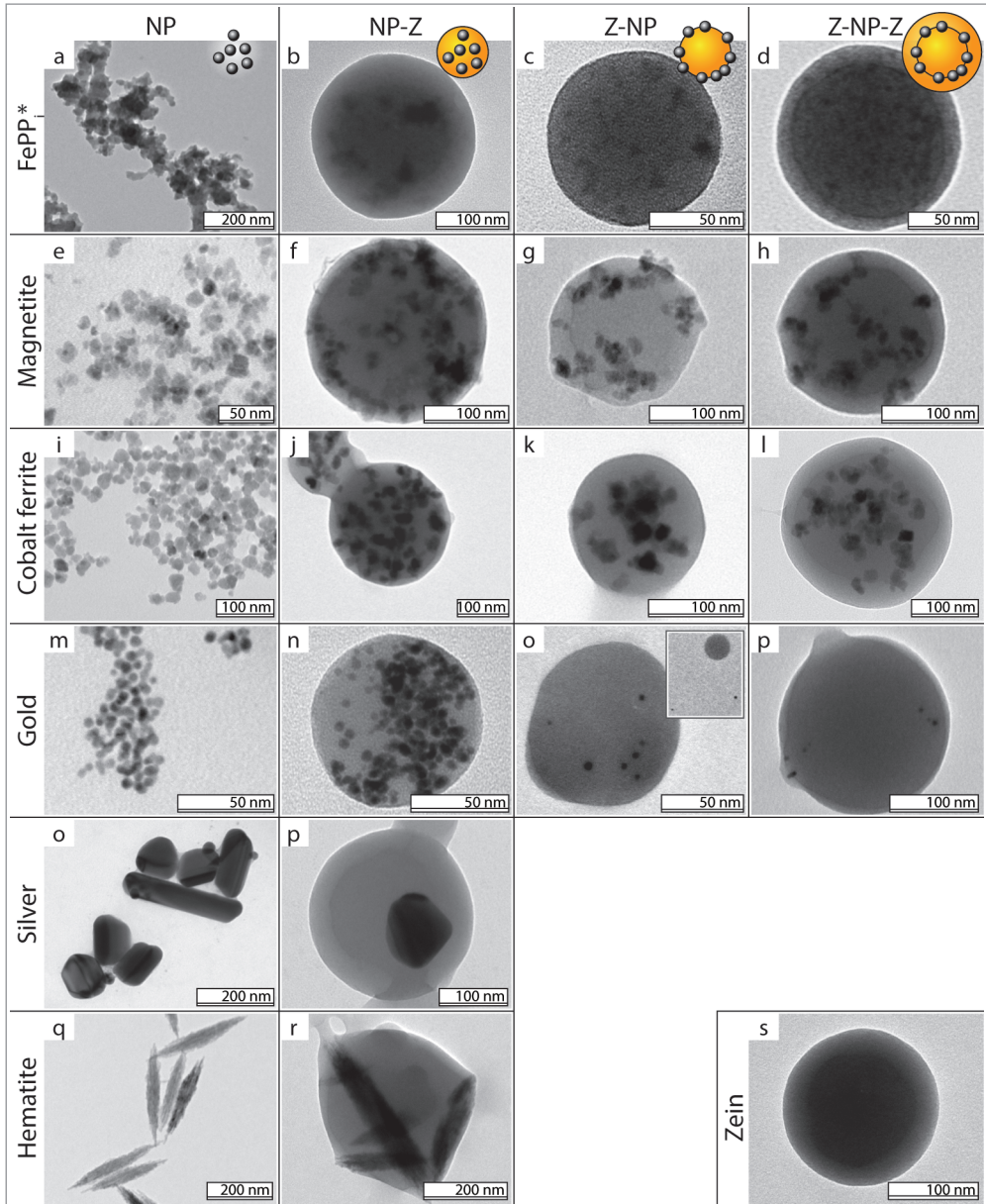


FIGURE 7.2 TEM image matrix of the prepared particles. Columns represent the various composite systems, which are from left to right: the bare nanoparticles, NP-Z, Z-NP and Z-NP-Z. Schematic representations of the systems are shown at the top of each column. Nanoparticle systems are represented in the rows, with from top to bottom: iron pyrophosphate, magnetite, cobalt ferrite, gold, silver and hematite. A bare zein particle is shown for comparison at the bottom right (s). The dark inner ring that can be observed in some images (d and h for example) is the contact area of the zein particle with the polymer film.

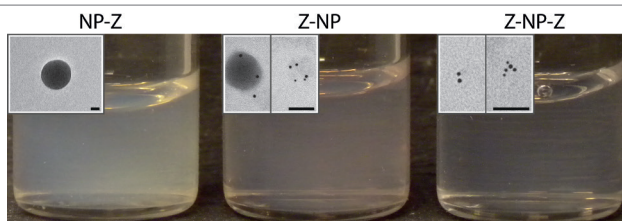


FIGURE 7.3 Supernatants of the three gold composite systems. The slightly pink color (see online version for color reproduction) of the Z-NP and Z-NP-Z supernatants indicates the presence (bare) nanoparticles. Representative TEM images in the insets show only empty zein particles for the NP-Z system, while individual nanoparticles are observed for the other two systems. Scalebars are 50 nm.

had a much higher concentration of them (e.g. compare FIGURE 7.2n and o). The empty zein material was easily removed from the magnetite and cobalt ferrite composite particles by magnetic separation as described in the experimental section, but the hematite system insufficiently magnetic to do the same. For this system and the composites containing non-magnetic materials, it is possible to remove the empty particles by centrifugation as these are lighter and smaller on average (50 nm diameter). While not all particles could be redispersed due to aggregate formation after strong centrifugation had been applied (1400 g), lower centrifugation speeds mitigated this effect. Furthermore, we expect that colloidal stability can be further improved by coating the zein particles with e.g. sodium caseinate, as has been demonstrated by Patel *et al* [16]. For magnetic applications it might be desirable to have greater control over particle size and magnetic content, which can be achieved by using size fractionation by depletion. This has been demonstrated by Bibette to be a powerful technique for size control [25].

7.5.II ELECTROPHORETIC MOBILITY AND DYNAMIC LIGHT SCATTERING.

Zeta-potential analysis by electrophoretic mobility measurements show the same trend for all materials: while all employed nanoparticles were negatively charged, the zeta potentials were positive for the composite materials, see TABLE 7.1. As would be expected, the systems with a zein surface (NP-Z and Z-NP-Z) had the highest zeta potentials of the

TABLE 7.1 Zeta-potential and dynamic light scattering results

	NP		NP-Z		Z-NP		Z-NP-Z	
	D* (nm)	ZP** (mV)	D* (nm)	ZP** (mV)	D* (nm)	ZP** (mV)	D* (nm)	ZP** (mV)
Zein	112	50	-	-	-	-	-	-
FePP _i	135	-42	166	42	188	15	228	53
Magn	57	-52	248	33	163	34	239	49
CoFe	38	-54	189	39	149	34	261	46
Au	15	-17	133	53	150	45	187	50
Ag	84	-43	145	54	-	-	-	-
Hem	158	-49	152	55	-	-	-	-

*Diameter **Zeta potential

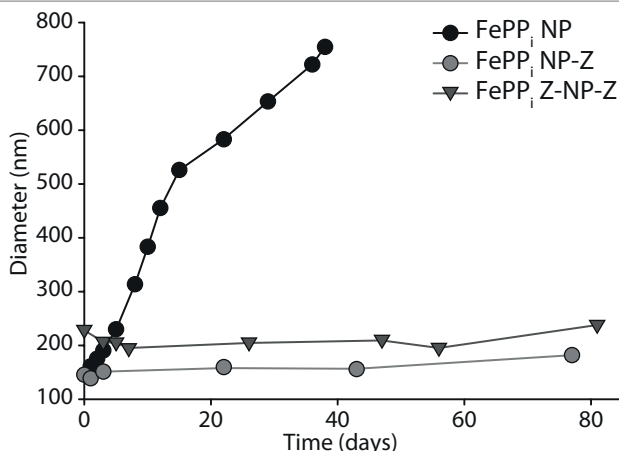


FIGURE 7.4 Particle growth over time as measured by DLS analysis. While the FePP_i NP system grows over time (dark circles), there is no significant change in the size of the zein composite systems for a period of almost three months.

composite materials. DLS analysis showed average diameters comparable to those found in TEM images with a broad size distribution, the Z-NP-Z systems were slightly larger on average. When following the size of the FePP_i particles with DLS over time, we again observed the slow aggregation of the bare nanoparticles found in CHAPTER 4 [17], while the NP-Z and Z-NP-Z systems remain at a stable particle diameter for months, see FIGURE 7.4. The Z-NP system aggregates on a similar timescale as the NP system (not shown).

7.6 CONCLUSIONS

We have shown that the zein protein can be used as a general heterocoagulation material for the preparation of biocompatible composite colloidal particles. We have used iron(III) pyrophosphate, cobalt ferrite, silver, gold and two types of iron oxide to prepare colloidal NP-Z, Z-NP and Z-NP-Z systems stabilized by a positive surface charge without any further additives. Because of the generality of the method, it should be possible to use any type (or mixture of types) of negatively charged nanoparticles to create these composite particles. Furthermore, we have illustrated one of the benefits of composite materials by showing that the inherently unstable iron pyrophosphate nanoparticles are stable for periods of months when prepared as a composite system. Finally, to further increase the applicability of the system, it has been shown elsewhere that zein can be made stable at physiological pH and redispersible after drying by coating with sodium caseinate [16]. Depending on the nature of the incorporated nanoparticles, this may result in a versatile, fully biocompatible composite material that can be tailor-made to the desired application.

7.7 ACKNOWLEDGEMENTS

We thank Laura Rossi for supplying the hematite spindles, Bob Luigjes for supplying the magnetite and cobalt ferrite particles and Julius de Folter for introducing us to the zein preparation.

7.8 REFERENCES

- [1] Prakash, A.; McCormick, A. V.; Zachariah, M. R. Tuning the Reactivity of Energetic Nanoparticles by Creation of a Core-Shell Nanostructure. *Nano Letters* **2005**, *5*, 1357-1360.
- [2] Ning, Y.; Zhang, H.; Yang, B. Versatile Fabrication of Water-Dispersible Nanoparticle-Amphiphilic Copolymer Composite Microspheres with Specific Functionalities. *J. Mat. Chem.* **2011**, *21*, 6837-6843.
- [3] Wang, G.; Su, X. The Synthesis and Bio-Applications of Magnetic and Fluorescent Bifunctional Composite Nanoparticles. *Analyst* **2011**, *136*, 1783-1798.
- [4] Koole, R.; Van Schooneveld, M. M.; Mulder, W. J. M. Paramagnetic Lipid-Coated Silica Nanoparticles with a Fluorescent Quantum Dot Core: A New Contrast Agent Platform for Multimodality Imaging. *Bioconjug. Chem.* **2008**, *19*, 2471-2479.
- [5] Caruthers, S. D.; Wickline, S. A.; Lanza, G. M. Nanotechnological Applications in Medicine. *Curr. Opin. Biotechnol.* **2007**, *18*, 26-30.
- [6] Caruso, F.; Spasova, M.; Liz-Marzán, L. M. Multilayer Assemblies of Silica-Encapsulated Gold Nanoparticles on Decomposable Colloid Templates. *Adv. Mater.* **2001**, *13*, 1090-1094.
- [7] Durán, J. D. G.; Arias, J. L.; Delgado, A. V. Magnetic Colloids as Drug Vehicles. *J. Pharm. Sci.* **2008**, *97*, 2948-2983.
- [8] Ichikawa, H.; Fukumori, Y. A Novel Positively Thermosensitive Controlled-Release Microcapsule with Membrane of Nano-Sized Poly(N-Isopropylacrylamide) Gel Dispersed in Ethylcellulose Matrix. *J. Controlled Release* **2000**, *63*, 107-119.
- [9] Shukla, R.; Cheryan, M. Zein: The Industrial Protein from Corn. *Ind. Crop. Prod.* **2001**, *13*, 171-192.
- [10] Hurtado-López, P.; Murdan, S. Zein Microspheres as Drug/Antigen Carriers: A Study of their Degradation and Erosion, in the Presence and Absence of Enzymes. *J. Microencapsul.* **2006**, *23*, 303-314.
- [11] Liu, X.; Sun, Q.; Wang, J. -. Microspheres of Corn Protein, Zein, for an Ivermectin Drug Delivery System. *Biomaterials* **2005**, *26*, 109-115.
- [12] Sakaguchi, N.; Theertham, P. R.; Juneja, L. R. Iron Absorption and Bioavailability in Rats of Micronized Dispersible Ferric Pyrophosphate. *Int. J. Vitam. Nutr. Res.* **2004**, *74*, 3-9.
- [13] Velikov, K. P.; Pelan, E. Colloidal Delivery Systems for Micronutrients and Nutraceuticals. *Soft Matter* **2008**, *4*, 1964-1980.
- [14] van Leeuwen, Y. M.; Velikov, K. P.; Kegel, W. K. Morphology of Colloidal Metal Pyrophosphate Salts. *RSC Adv.* **2012**, *2*, 2534-2540.
- [15] Baimark, Y.; Srisa-Ard, M.; Kittipoom, S. Preparation of Surfactant-Free Nanoparticles of Methoxy Poly(Ethylene Glycol)-B-Poly(D,L-Lactide-Co-Glycolide-Co-E-Caprolactone). *Colloid J.* **2009**, *71*, 18-21.
- [16] Patel, A. R.; Bouwens, E. C. M.; Velikov, K. P. Sodium Caseinate Stabilized Zein Colloidal Particles. *J. Agric. Food Chem.* **2010**, *58*, 12497-12503.
- [17] van Leeuwen, Y. M.; Velikov, K. P.; Kegel, W. K. Stabilization through Precipitation in a System of Colloidal Iron(III) Pyrophosphate Salts. *J. Colloid Interface Sci.* **2012**, *38*, 43-47.
- [18] Massart, R. Preparation of Aqueous Magnetic Liquids in Alkaline and Acidic Media. *IEEE Trans. Magn.* **1981**, *MAG-17*, 1247-1248.
- [19] Claesson, E. M.; Philipse, A. P. Monodisperse Magnetizable Composite Silica Spheres with Tunable Dipolar Interactions. *Langmuir* **2005**, *21*, 9412-9419.
- [20] Tourinho, F. A.; Franck, R.; Massart, R. Aqueous Ferrofluids Based on Manganese and

Cobalt Ferrites. *J. Mater. Sci.* **1990**, *25*, 3249-3254.

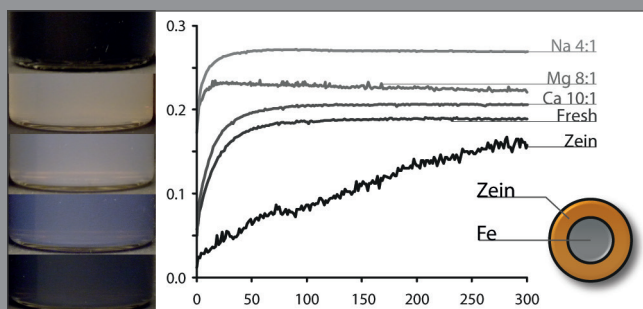
[21] Ocaña, M.; Morales, M. P.; Serna, C. J. Homogeneous Precipitation of Uniform A-Fe₂O₃ Particles from Iron Salts Solutions in the Presence of Urea. *J. Colloid Interface Sci.* **1999**, *212*, 317-323.

[22] Sacanna, S.; Rossi, L.; Philipse, A. P. Fluorescent Monodisperse Silica Ellipsoids for Optical Rotational Diffusion Studies. *Langmuir* **2006**, *22*, 1822-1827.

[23] Pérez-Juste, J.; Liz-Marzán, L. M.; Mulvaney, P. Electric-Field-Directed Growth of Gold Nanorods in Aqueous Surfactant Solutions. *Adv. Funct. Mater.* **2004**, *14*, 571-579.

[24] Tan, Y.; Li, Y.; Zhu, D. Preparation of Silver Nanocrystals in the Presence of Aniline. *J. Colloid Interface Sci.* **2003**, *258*, 244-251.

[25] Bibette, J. Depletion Interactions and Fractionated Crystallization for Polydisperse Emulsion Purification. *J. Colloid Interface Sci.* **1991**, *147*, 474-478.



CHAPTER 8

REACTIVITY OF COLLOIDAL IRON-CONTAINING PYROPHOSPHATE SALTS

In this chapter we determine the relative reactivity of the iron contained within the particles prepared throughout this thesis and compare it to 'free' Fe^{3+} in the form of FeCl_3 by making use of a model system for reactivity of iron in food products. We analyse and compare three types of systems: iron pyrophosphate, mixed-metal pyrophosphates containing Fe^{3+} and a divalent cation M^{II} , and protein-coated iron pyrophosphate. We find that: (i) Incorporating iron in a colloidal salt reduces its reactivity compared to free Fe^{3+} . (ii) Coating the particles with a layer of hydrophobic protein (zein) further decreases the reactivity but interferes with the analysis method due to the increased turbidity of the dispersion. And finally, our most surprising result is that (iii) preparing a dispersion containing more Fe than M^{II} actually increases the reactivity of the contained iron, while the reversed, a system containing excess M^{II} , seems to inhibit the reactivity completely.

8.1 INTRODUCTION

As mentioned in the introduction of this thesis, one of the challenges of adding iron to foodstuffs is the complex formation of iron ions with the polyphenols that are abundant in fruits and vegetables. Polyphenols strongly chelate iron ions and the complexes with iron have intense and persistent colours [1-3], illustrated by the fact that gallotannic acid (a polyphenol from gallnuts) combined with iron(II) has been used abundantly as a black ink for about 2000 years [4].

Throughout this thesis we have prepared various systems of nanoparticles that contain iron, with the intent of reducing the reactivity of this iron with respect to iron ions in solution. In CHAPTER 6 we incorporated a secondary mineral in order to dilute the iron content and therefore reduce its reactivity even further, while in CHAPTER 7 we coated the particle with a hydrophobic protein to shield the particles from the surrounding medium. In this chapter, we investigate the reactivity of these systems by using gallic acid (GA) as a model system for the polyphenols present in foodstuffs [5, 6]. The three systems analysed are (a) iron(III) pyrophosphate (FePP_i) from CHAPTER 2, (b) mixed-metal pyrophosphates from CHAPTER 6 and (c) zein composite systems from CHAPTER 7, see FIGURE 8.1.

The formation of the Fe^{III}-GA complex is followed in time using spectrophotometry [1, 7]. However, the analysis is complicated by the ability of polyphenols to reduce Fe³⁺, resulting in Fe²⁺ and a quinone. Although various possible pathways are known for this reaction [8-10], the most probable one under physiological conditions is described by Hynes *et al* [11] as shown in FIGURE 8.2. Once the quinone has been formed, the Fe²⁺ can be oxidized to form a new complex with free gallic acid. As we will show in this chapter, the oxidation reaction is much slower than the initial complex formation and the cyclization of the reaction can be limited by sealing the sample air tight. However, due to the side reactions and the complexity of the system we will only analyse the initial reactivity during the first five hours after addition and we will only make qualitative comparisons between identically prepared samples.

8.2 METHODS

8.2.1 COLLOIDAL METAL PYROPHOSPHATES

All systems were prepared using the methods described in their respective chapters: pure iron(III)pyrophosphate (FePP_i) as described in CHAPTER 2, mixed systems as described in CHAPTER 6 and zein coated systems as described in CHAPTER 7. The mixed-metal pyrophosphates in this chapter consist of iron and another mineral being Ca²⁺, Mg²⁺ or Zn²⁺ (commonly referred to as M^{II} in this thesis), or Na⁺. The systems are indicated by their Fe:M^{II} or Fe:Na ratio, so that the 'mixed Mg 10:1 system' denotes Fe₁₀MgPPi₈. See CHAPTER 6 for details.

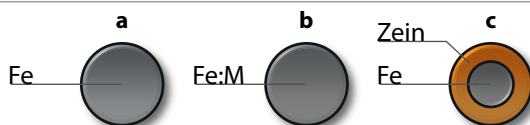


FIGURE 8.1 Schematic representation of the three colloidal systems analysed in this chapter: pure iron pyrophosphate (a), mixed-metal pyrophosphates (b) and the zein composite system (c).

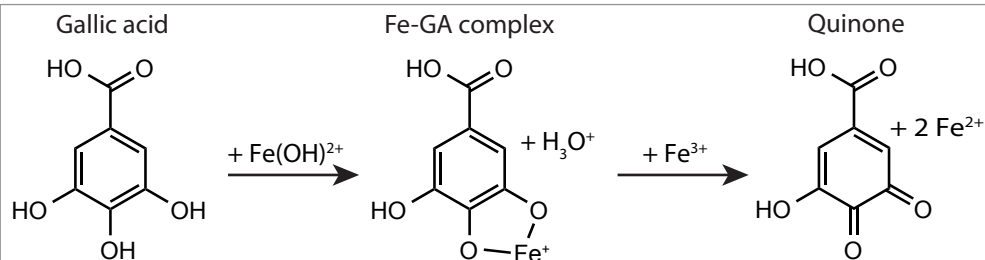


FIGURE 8.2 Iron(III)-gallic acid complex formation and the subsequent oxidation of gallic acid to its quinone.

8.2.II REACTIVITY ANALYSIS BY SPECTROPHOTOMETRY

All samples for spectrophotometry were prepared to contain the same concentration of iron (0.7 mM). Excess gallic acid (3.5 mM, Scharlau Chemie, extra pure $\geq 99.5\%$) was added and the cuvette sealed air-tight for spectrophotometry using a Perkin-Elmer Lambda-35 spectrophotometer. All samples were thermostated at 23°C and magnetically stirred during analysis. The influence of (a change in) sample turbidity on the absorbance was countered by using the dispersion at the same concentration but without added gallic acid as reference.

8.3 RESULTS

An initial test reaction already showed the clear inhibition of the Fe-GA complex formation by incorporating the iron in an inorganic matrix. FIGURE 8.3a-e shows that a solution of FeCl_3 sample immediately turned black upon addition of gallic acid while a sample

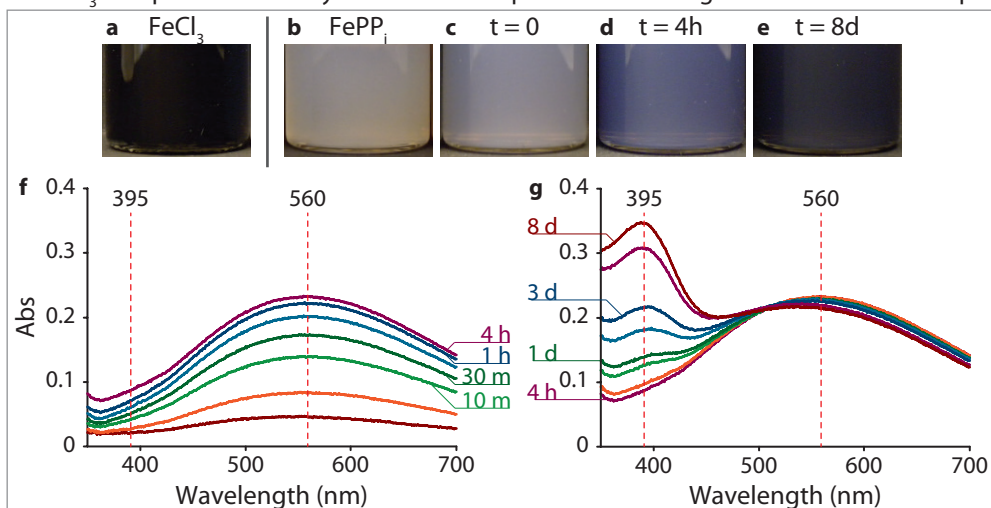


FIGURE 8.3 Initial reactivity studies. Top row of photos shows the inhibited reactivity of FePP_i compared to FeCl_3 at same concentration of iron (a-e). While FeCl_3 turns black instantaneously upon addition of gallic acid (a), a freshly prepared dispersion of FePP_i (b), immediately (c), four hours (d) and eight days (e) after addition of gallic acid shows the slow discoloration of the dispersion. UV-Vis spectra of the reaction mixture up to four hours (f) and up to seven days (g) after addition of gallic acid show the fast initial complex formation at 560 nm, and the slower reaction of quinone formation at 395 nm.

containing iron pyrophosphate had only reached full coloration after seven days. Analysis using spectrophotometry (FIGURE 8.3f and g) showed that most of the complex formation occurred within the first hour and that the quinone signal started to become significant after about four hours, making further analysis of the reaction inaccurate. Therefore, it was decided to analyse the absorbance at 560 nm only for the first five hours after the addition of gallic acid.

8.3.I REACTIVITY OF COLLOIDAL IRON PYROPHOSPHATE

Spectrophotometric analysis of the complex formation in time showed a clear influence of the preparation method on the reactivity of the particles. A sample freshly prepared by the coprecipitation method (see CHAPTER 2) increased absorbance until it reached its maximum value after about 60 minutes, see FIGURE 8.4a, while a dialyzed system increased much more slowly and had not fully reached its plateau value after 300 minutes. A solution of FeCl_3 at the same concentration of iron had an initial absorbance of 0.8 (not shown), indicating successful protection of the majority of the Fe^{3+} at least for the duration of the analysis. FIGURE 8.4a also shows that aging a system for one month before the addition of gallic acid further decreased its reactivity. This cannot be due to the larger cluster size caused by aging (discussed in CHAPTER 4) as a dialyzed system that was aged for one month also showed the lowered reactivity while the clusters had not grown (see TABLE 8.1).

It is interesting to note that while both the freshly prepared and freshly dialyzed systems started at the same initial value, this initial jump was significantly smaller for the aged systems. The initial jump indicates that a large part of the reaction occurs at the surface of the particles, while the decrease with aging seems to indicate that the surface reactivity somehow lowers over time.

TABLE 8.2 shows no significant change of the cluster size and zeta-potential due to the reaction with gallic acid, the increased conductivity is due to the addition of gallic acid. TEM analysis (FIGURE 8.5) showed that the surface of the particles had become somewhat smoother after reaction, possibly due to dissolution.

8.3.II REACTIVITY OF COLLOIDAL MIXED-METAL PYROPHOSPHATES

The data of the zein-coated pure FePP_i (FIGURE 8.4b) shows that coating the particles

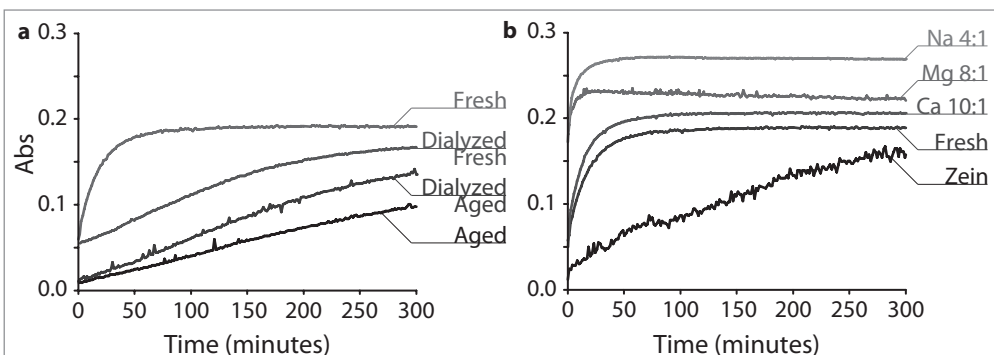


FIGURE 8.4 Iron-gallic acid complex formation followed over time. Comparison of reactivity between the pure FePP_i samples (a) and mixed systems (b), all prepared at the same concentration of Fe^{3+} . The absorbance of FeCl_3 with gallic acid at this concentration is 0.8 (not shown).

TABLE 8.1 Cluster size, zeta-potential (ZP) and conductivity (C) of aged and dialyzed FePP_i

	Size (nm)	ZP (mV)	C (mS/cm)
Freshly prepared	270	-38	2.2
Freshly Dialyzed	295	-40	0.03
Aged 1 month	360	-36	2.3
Dialyzed aged	290	-24	0.04

TABLE 8.2 Cluster size, zeta-potential (ZP) and conductivity (C) before and after reaction with

	Size (nm)	ZP (mV)	C (mS/cm)
Fresh	215	-32	2.10
Diluted*	215	-35	0.35
Aged 5 h	210	-34	0.34
Aged with gallic acid	210	-33	0.51
Gallic acid	-	-	0.15

*Diluted to the concentration used for spectrophotometry, 0.7 mM Fe³⁺

with zein reduced the reactivity of the contained iron. However, the data also shows one important disadvantage of this analysis method: the high turbidity of these dispersions significantly increased the noise level.

MIXED SYSTEMS WITH HIGH Fe³⁺ CONTENT. As can be seen in FIGURE 8.4b, the reactivity of the mixed systems with high iron content is higher than the reactivity of the pure FePP_i as the initial slopes are steeper and the final absorbances are higher. We used the most stable mixed system for every cation: 4:1 for Na, 8:1 for Mg and 10:1 for Ca (see CHAPTER 6 for details on dispersion stability). The reactivity of the dispersions increases with the stability of the dispersion: while the Ca mixed system completely aggregated within days, its reactivity was closest to that of pure FePP_i. On the other hand, the Na system was the most reactive of all compounds tested in this chapter while it remained stable in dispersion for months.

MIXED SYSTEMS WITH HIGH M^{II} CONTENT. As we have shown in CHAPTER 6, we have only been able to prepare stable colloidal systems at high M^{II} content using magnesium. Systems containing Ca and Zn sediment within minutes to hours while Na containing systems do not form particles at all. However, we have been unable to analyse the reactivity of Fe:Mg mixed systems with low iron content: the addition of gallic acid caused the dispersion to aggregate completely as shown in FIGURE 8.6 for a Fe:Mg 1:50 dispersion. However, the figure also shows that there was no appreciable discoloration for up to five hours after the

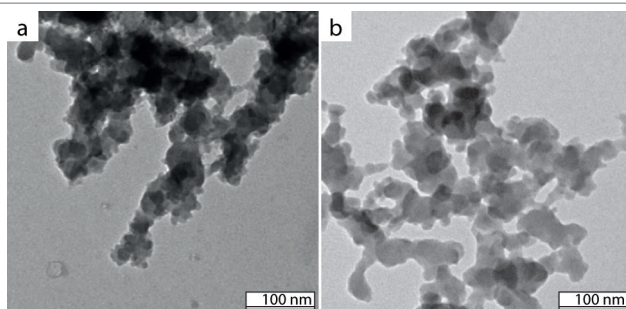


FIGURE 8.5 TEM images of pure FePP_i before (a) and after (b) the reaction with gallic acid shows a smoother particle surface after the reaction.

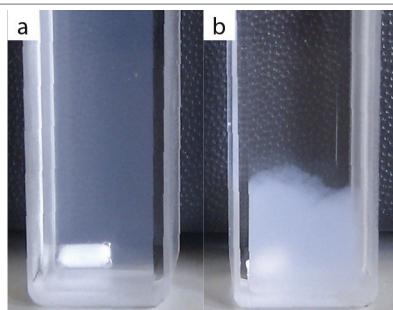


FIGURE 8.6 The Fe:Mg 1:50 mixed system five hours after the addition of gallic acid: (a) without GA and (b) with GA. While the GA-containing dispersion has aggregated, the sample does not show the coloration characteristic of the Fe-GA complex seen in FIGURE 8.3.

addition of gallic acid, indicating that the contained iron was successfully protected from reaction.

8.4 CONCLUSIONS

Using gallic acid as a model system for the reactivity of Fe^{3+} in foodstuffs, we have shown that embedding the iron in an inorganic matrix reduces its reactivity relative to FeCl_3 . Analysis of aged and dialyzed systems indicates that most of the reactivity occurs at the surface of the particles and that this surface reactivity decreases over time for reasons that are yet unclear. Coating the particles with zein successfully protects the incorporated iron as it further decreases its reactivity.

We show that mixed systems actually increase reactivity at low iron content: there is a counterintuitive trend for the mixed systems in the sense that the less iron the particles contain, the more reactive they become for Fe:M ratios below 1:1. However, above this ratio and at much lower iron content (below 5%), the reactivity decreases significantly as we observed no discoloration of the Fe:Mg 1:50 mixed system at all.

We find that while the polyphenol-method is useful for determining the relative reactivity of iron-containing materials, the side reaction makes the method hard to control and inaccurate over longer periods of time. Moreover, due to the colloidal size of the particles there is significant interference with the analysis method, especially when the particles aggregate in the presence of gallic acid as shown in FIGURE 8.6.

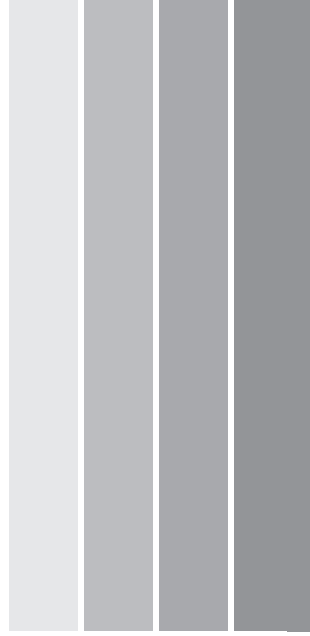
Future research should focus on finding a different (in-situ) analysis method for determining the reactivity of iron in colloidal dispersions that does not depend on the optical properties of the samples. The colloidal nature of our systems will almost always cause them to interfere with optical measurements, especially when the stability or concentration of the particles changes during the reaction as we have shown here.

Finally, we have yet to prepare a stable zein-coated Fe:Mg 1:50 system. Coating them with zein might prevent the particles from aggregation upon addition of gallic acid and result in the best candidate for food application as it is the least reactive system we have studied.

8.5 REFERENCES

[1] Mellican, R. I.; Li, J.; Nielsen, S. S. The Role of Iron and the Factors Affecting Off-Color Development of Polyphenols. *J. Agric. Food Chem.* **2003**, *51*, 2304-2316.

- [2] Hider, R. C.; Liu, Z. D.; Khodr, H. H. Metal Chelation of Polyphenols. *Method. Enzymol.* **2001**, *335*, 190-203.
- [3] Van Acker, S. A. B. E.; Van Den Berg, D. J.; Bast, A. Structural Aspects of Antioxidant Activity of Flavonoids. *Free Radical Bio. Med.* **1996**, *20*, 331-342.
- [4] De Feber, M. A. P. C.; Havermans, J. B. G. A.; Defize, P. Iron-Gall Ink Corrosion: A Compound-Effect Study. *Restaurator* **2000**, *21*, 204-212.
- [5] Chvátalová, K.; Slaninová, I.; Slanina, J. Influence of Dietary Phenolic Acids on Redox Status of Iron: Ferrous Iron Autoxidation and Ferric Iron Reduction. *Food Chem.* **2008**, *106*, 650-660.
- [6] Fazary, A. E.; Taha, M.; Ju, Y. H. Iron Complexation Studies of Gallic Acid. *J. Chem. Eng. Data* **2009**, *54*, 35-42.
- [7] Chvátalová, K.; Slaninová, I.; Slanina, J. Influence of Dietary Phenolic Acids on Redox Status of Iron: Ferrous Iron Autoxidation and Ferric Iron Reduction. *Food Chem.* **2008**, *106*, 650-660.
- [8] H.K.J. Powell, M. C. T. Interactions of Iron(II) and Iron(III) with Gallic Acid and its Homologues: A Potentiometric and Spectrophotometric Study. *Aust. J. Chem.* **1982**, *35*, 739-756.
- [9] Arif Kazmi, S.; Saqib Qureshi, M.; Maqsood, Z. Reactivity of an Iron(III) Complex of Gallic Acid. *Inorg. Chim. Acta* **1987**, *137*, 151-154.
- [10] Funabiki, T.; Mizoguchi, A.; Yoshida, S. Oxygenase Model Reactions. 1. Intra- and Extradiol Oxygenations of 3,5-Di-Tert-Butylcatechol Catalyzed by (Bipyridine)(Pyridine) Iron(III) Complex. *J. Am. Chem. Soc.* **1986**, *108*, 2921-2932.
- [11] Hynes, M. J.; Ó Coinceannainn, M. The Kinetics and Mechanisms of the Reaction of Iron(III) with Gallic Acid, Gallic Acid Methyl Ester and Catechin. *J. Inorg. Biochem.* **2001**, *85*, 131-142.



SUMMARY

S.1 SUMMARY

The objective of this thesis work was to incorporate (mixed) dietary minerals into a colloidal, colourless, inorganic matrix material suitable for food fortification, as food fortification is often problematic due to the interaction of the mineral ions with the foodstuffs to which they are added. The addition of iron is the most problematic due its reactivity with certain components of the foodstuffs, but incorporating the cation in an insoluble particle will greatly reduce the reactivity compared to free ions in solution. In search of a stable colloidal dispersion of such a material, we have used various methods to prepare metal pyrophosphate salts containing divalent mineral cations ($M^{II}PP_i$), trivalent cations ($M^{III}PP_i$) or mixtures thereof. We have studied the colloidal properties of the resulting systems and tested the stable dispersions for their reactivity with foodstuffs using a model system.

S.2 SECTION 1: PREPARATION

In the first section we explore various methods for preparing colloidal metal pyrophosphate salts.

We show in CHAPTER 2 that during coprecipitation the valence of the metal cation determines the morphology of the resulting particles. Using trivalent cations (Fe, Al) results in small, amorphous nanoparticles while divalent metals (Ca, Mg, Zn) yields large crystalline particles of various shapes. Furthermore, altering the preparation method by addition of surfactants or use of autoclave treatment drastically changes the morphology of $M^{II}PP_s$, while it has no effect on $M^{III}PP_s$ whatsoever. The difference in crystallinity between $M^{II}PP_i$ and $M^{III}PP_i$ could be caused by the greater complexity necessary in the formation of an uncharged unit of $M^{III}PP_i$ compared to $M^{II}PP_i$, thereby resulting in an amorphous structure upon fast precipitation of $M^{III}PP_i$.

Because the $M^{II}PP_s$ prepared in the first chapter are too large to form stable colloidal dispersions, we use the pH-dependent solubility of metal pyrophosphates to prepare smaller particles of $M^{II}PP_i$ in CHAPTER 3. Using the fact that $M^{II}PP_s$ are soluble in acid, we examine two methods for raising the pH of such an acidic solution of metal pyrophosphate. In the first method the pH is raised by the gradual decomposition of urea, while in the second it is raised instantaneously by injecting the dissolved complex in alkaline media. While most preparation routes and material compositions lead to unstable systems, we find that the injection method results in stable dispersions of $MgPP_i$.

S.3 SECTION 2: PROPERTIES

In this section we first focus on the colloidal stability of iron(III) pyrophosphate and next investigate the stability of $M^{II}PP_s$ and mixed-metal pyrophosphates.

In CHAPTER 4 we study the stability of colloidal iron(III) pyrophosphate. We find that the 5-20 nm nanoparticles that form during precipitation immediately aggregate into finite sized (~200 nm) clusters. These clusters remain in dispersion for periods of days even without additives such as surface active molecules, but eventually aggregate completely. While dialysis postpones this final aggregation, a system at low ionic strength will destabilize as well after a period of months. We suggest that the stability of the particles is influenced by the decreasing ionic strength during the precipitation of the iron salt. We corroborate this coupling of ionic strength and colloidal stability by calculating the interaction potentials between the aggregates and show that while the nanoparticles are initially unstable, the lowered ionic strength causes them to become (meta-)stable once

all particles have formed.

In CHAPTER 5 we demonstrate the repectization of an aggregated colloidal system under circumstances that should not allow for redispersion according to commonly accepted theory. We show that we are able to redisperse a system of colloidal iron(III) pyrophosphate that has been aggregated at high ionic strength (2 M NaCl) even after having aged for one month. This is intriguing as we still have not added any means of stabilization such as surfactants. While repectization from the primary minimum is known to occur under certain conditions, this is much less likely for a charge-stabilized system aged for such a long period of time. We propose that these results are due to the open structure of the material: large, open clusters connected by nanometer sized particles. During dialysis the interconnecting particles dissolve (due to the limited solubility of the material) and the clusters are released from their aggregated state. Furthermore, we find that a certain combination of salt addition and repectization leads to a colloidal system that is stable for a longer period of time than a freshly prepared sample. This is most likely due to surface effects again linked to the slight solubility of the material.

Finally, in CHAPTER 6, we prepare mixed-metal pyrophosphates by using both preparation methods described in the first two chapters: in the first method we incorporate M^{II} into $FePP_i$ by means of coprecipitation, in the second we incorporate Fe^{3+} into $M^{II}PP_i$ using the pH-dependent precipitation method. The use of two separate methods is necessary as we are able to incorporate only up to 20% of M^{II} when using the coprecipitation method. However, when using the second method we can prepare stable dispersions containing up to 95% of magnesium. When preparing mixed systems we find that the morphology of the resulting material is dominated by that of the metal in excess: M^{III} excess yields amorphous particles while M^{II} excess forms (partially) crystalline materials. Furthermore, substitution of iron with Na^+ or Mg^{2+} in the coprecipitation method yields dispersions that are be stable for longer periods of time than pure $FePP_i$.

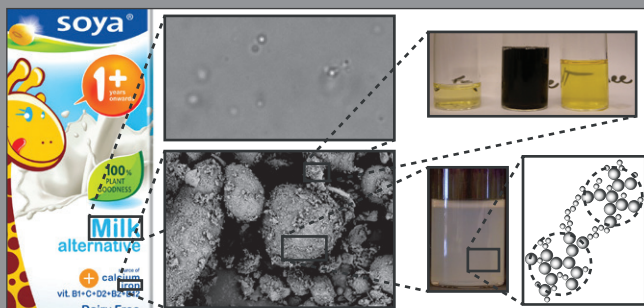
S.4 SECTION 3: APPLICATIONS

The final section deals with the application of the metal pyrophosphates in two ways: first we design an advanced delivery system for the (mixed-)metal pyrophosphate salts and in the CHAPTER 8 we investigate the applicability of the materials prepared in this thesis by testing the reactivity of the incorporated iron.

In CHAPTER 7 we demonstrate a method to further protect the iron from the surrounding medium. As we have shown in CHAPTER 5, dispersions of $FePP_i$ are only stable for long periods of time when prepared at very low ionic strength. As this is unpractical for the intended applications, we embed the particles in a composite system using a protein as the matrix material and show that the resulting systems are stable for much longer periods of time than the original $FePP_i$ dispersions. We establish that the preparation method is general and based on electrostatic interactions by incorporating other types of nanoparticles into the composite particles as well, such as iron oxide, silver and gold nanoparticles (all stabilized by a negative surface charge).

In the CHAPTER 8 we compare the reactivity of the iron-containing colloidal dispersions prepared in this thesis. By using a model system for the reactivity of iron in foodstuffs, we determine the relative reactivity of the colloidal dispersions by following the complex formation over time using spectrophotometry. We find that incorporating iron in an inorganic matrix lowers its reactivity. Surprisingly, we find that introducing low concentrations of another mineral into $FePP_i$ will increase the reactivity of the iron

while incorporating Fe^{3+} into $\text{M}^{\text{II}}\text{PP}_i\text{s}$ decreases it. Finally, using the newly designed zein composites, we demonstrate that incorporating FePP_i into zein not only increases the stability of the colloidal dispersion as shown in CHAPTER 7, but also reduces the reactivity of the contained iron as intended.



SAMENVATTING

IN HET NEDERLANDS (OOK VOOR LEKEN)

Nadat u de kaft uitvoerig bestudeerde (voor- en achterkant) en de titel een paar keer gelezen had kwam u er achter dat er ook een Nederlandse vertaling op de titelpagina staat. Na ook die gelezen te hebben was u helaas nog steeds niet veel wijzer. U bladerde wat door het boekje, bekeek hier en daar een illustratie en las een paar zinnen, maar nu vraagt u zich toch echt af waar dit boekje nou eigenlijk over gaat. Wetenschap is, net als andere vakgebieden, meestal 'van ingewijden voor ingewijden'. De titel is er al een mooi voorbeeld van. "Colloïdale metaal-pyrosfaatzouten: bereiding, eigenschappen en toepassingen". Het deel na de dubbele punt gelooft u wel (vooral het laatste punt lijkt u relevant), maar colloïdale metaal-pyrosfaatzouten?

Of misschien bent u gewoon benieuwd naar wat Mikal nou eigenlijk heeft gedaan in de afgelopen vier jaar. Voor u daarom hier een samenvatting in het Nederlands (ook voor leken), opgedeeld in de afzonderlijke termen van de titel.

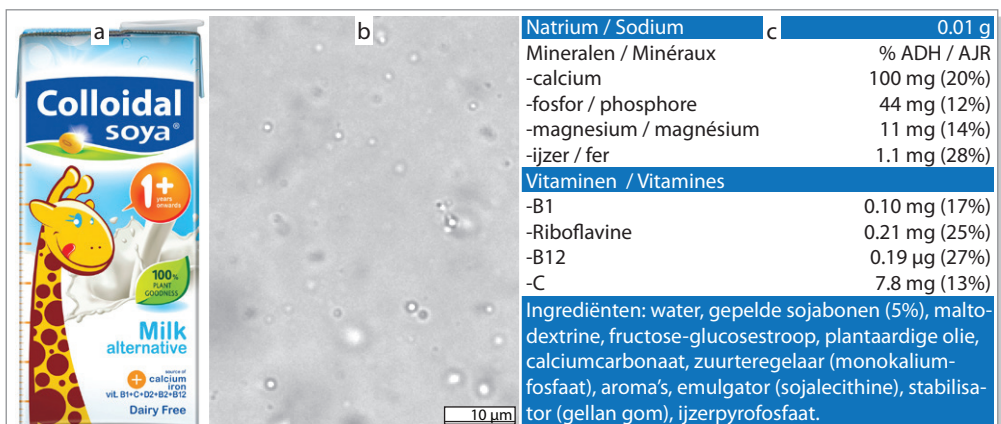
S.1 COLLOÏDALE

Kort door de bocht is het enige dat een colloïde of colloïdaal deeltje definieert zijn grootte, die moet liggen tussen 1 en 1000 nanometer. Een nanometer is een miljardste deel van een meter. Als u een lijn zou trekken van een miljoen nanometer lang (wat een prestatie zou zijn), zou deze ongeveer even lang zou zijn als de breedte van de punt aan het einde van deze zin. Met deze definitie vallen nanodeeltjes ook in het domein van de colloïden, of, zo u wilt, zijn de meeste colloïden ook nanodeeltjes.

Het interessante van colloïdale deeltjes is dat ze zich op het grensgebied bevinden van de microscopische wereld van atomen en moleculen en de macroscopische wereld van bijvoorbeeld het boekje dat u nu in uw handen houdt of, wat makkelijker voor de komende vergelijking, een hoopje zandkorrels. Doordat ze zich op dit grensgebied bevinden vertonen de deeltjes een belangrijke combinatie van eigenschappen: ze zijn klein genoeg om zich nog te gedragen als atomen en moleculen, maar (meestal) groot genoeg om gezien te kunnen worden. Waar zandkorrels in een glas water direct naar de bodem zullen zakken, kunnen colloïdale deeltjes net als atomen en moleculen door de vloeistof heen blijven bewegen en een zogenaamde **colloïdale dispersie** vormen. Waar atomen en moleculen alleen onder zeer bijzondere omstandigheden 'zichtbaar' gemaakt kunnen worden, kun je colloïden vaak al bestuderen met een eenvoudige microscoop.

Zoals gezegd is de enige voorwaarde de afmeting; materiaal en samenstelling doen er niet toe. Colloïdale systemen komen dan ook in vele soorten voor. Enkele alledaagse voorbeelden zijn mist (waterdruppels in de lucht), rook (roetdeeltjes in de lucht), modder (kleideeltjes in water), latexverf (oliedruppels in water), slagroom (luchtbellen in vet) en (nu hoort u op de achtergrond een kleine zucht van de gemiddelde colloïdchemicus) melk: een dispersie van vetdruppeltjes en eiwitten in water zoals te zien in FIGUUR S.1. Dat sommige van deze systemen uiteindelijk toch uitzakken komt doordat de deeltjes na verloop van tijd samenklonteren en zo buiten de colloïdale lengtemaat vallen. Dit samenklonteren heet **aggregatie**, of samenvloeiing in het geval van vloeibare deeltjes en gasbellen.

Kijkt u echter nog een keer naar de verpakking van deze sojamelk in FIGUUR S.1.c, dan zult u zien dat vooral aan dit soort niet-dierlijke voedingsmiddelen aardig wat zaken toe



FIGUUR S.1 Sojamelk is een voorbeeld van een colloïdale dispersie (a). Onder de microscoop zijn de vetdruppels zichtbaar, waarvan een deel de colloïdale afmeting heeft (b). Op de ingrediëntenlijst is een hoop interessants te vinden (c).

worden gevoegd. Dit brengt ons bij de volgende term uit de titel.

S.2 METAAL-

Deze term is enigszins misleidend, aangezien we niet metaal bedoelen als in de meest gebruikte betekenis van het woord. We hebben het over de 'essentiële mineralen' die een mens over het algemeen via de voeding binnen krijgt, zoals ijzer, calcium, magnesium en zink, en die nodig zijn voor het menselijk lichaam om goed te kunnen functioneren. Is er een tekort aan een van deze mineralen (een zogenaamde mineraal deficiëntie) kan dit gevolgen hebben. Zo kan de meest voorkomende mineraal deficiëntie ijzertekort leiden tot bloedarmoede. Om dit tegen te gaan maken we gebruik van voedingssupplementen. Hier wil ik graag een onderscheid maken tussen twee vormen van voedingssupplementen waar op taalgebied eigenlijk geen onderscheid tussen is.

Van Dale:

sup-ple-ment (het; o; meervoud: supplementen): bijvoegsel, aanvulsel

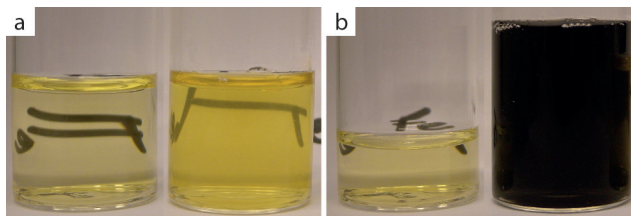
We zullen hier deze twee definities gebruiken om het onderscheid duidelijker te maken. In de eerste, meer gangbare definitie van het **bijvoegsel** hebben we het over supplementen zoals bijvoorbeeld de vitaminepillen of bruistabletten die apart ingenomen worden. In dit proefschrift hebben we echter gewerkt aan een systeem uit de tweede definitie: het **aanvulsel**, een aanvulling op het voedsel zelf. Waar het bijvoegsel altijd naast de etenswaren wordt ingenomen, is het aanvulsel een onderdeel van de voedingsmiddelen zoals te zien in FIGUUR S.1c. In het Engels wordt dit *food fortification* genoemd, oftewel het 'versterken' van voedingsmiddelen met essentiële voedingsstoffen. Het belangrijkste verschil tussen de twee vormen van supplementen is de ervaring van de consument of patiënt. Iedereen die wel eens staalpillen heeft moeten innemen voor ijzertekort of bloedarmoede weet dat dit geen pretje is: de smaak, die vaak wordt omschreven als die van bloed, kan de hele dag blijven hangen, wat tot misselijkheid en verlies van eetlust kan leiden. Maar als de mineralen direct aan de voedingsmiddelen kunnen worden toegevoegd dan zouden deze problemen wellicht te voorkomen zijn.

Hierbij stuiten we wel meteen op een paar problemen, of eigenlijk de voorwaarden voor een bruikbaar aanvulsel. Ten eerste moet het aanvulsel zelf niet waarneembaar zijn voor de consument; het mag geen duidelijke smaak, kleur, geur of textuur hebben die opgemerkt kan worden. Ten tweede mag het product waar het aanvulsel aan het toe wordt gevoegd niet beïnvloed worden door het aanvulsel (door bijvoorbeeld een reactie).

Ijzer is in beide opzichten een probleem. Bijna alle vormen van ijzer hebben een sterke kleur: ijzeroxides (roest) kunnen in bijna elke denkbare kleur verkregen worden, wat ze aantrekkelijk maakt als verfpigment maar onbruikbaar als aanvulsel. Bovendien heeft ijzer net als in de staalpillen vaak een sterke smaak. Maar wat wellicht het grootste probleem is, is dat ijzer in oplossing kan reageren met verschillende onderdelen van voedingsmiddelen.

Een voorbeeld hiervan is de reactie met plantaardige voedingsmiddelen die zogenaamde **polyfenolen** bevatten. Wanneer ijzer en polyfenol met elkaar binden vormt dit een **complex** met een zeer sterke, paars tot zwarte kleur. Niet voor niets is de inkt die gemaakt kan worden door een combinatie van galappels en ijzer ongeveer 2000 jaar lang zeer populair geweest. Gefermenteerde galappels van eikenbladeren bevatten een polyfenol, looizuur, dat samen met ijzer een donkere, permanente inkt geeft (zie ook referentie[1]).

Wellicht heeft u bij een scheikunde- of biologiesles wel eens een ijzerzout aan thee



FIGUUR S.2 IJzerchloride en groene thee. (a) een oplossing van ijzerchloride (links) en een glas groene thee (rechts). Wanneer het ijzerchloride aan de thee wordt toegevoegd wordt deze direct zwart en ondoorzichtig (b).

toegevoegd; dit experiment maakt gebruik van diezelfde reactie. Heeft u dit nog niet gedaan dan is hier uw kans: los een mespuntje ijzerchloride (als etsmiddel verkrijgbaar bij drogist, zelfbouw-electronica zaak of kunstenaarswinkel) of ijzersulfaat (een mosbestrijdingsmiddel, of misschien heeft u nog een paar staalpillen liggen) op in wat water en het zal een zeer lichte, geel of groene kleur hebben. Voegt u het echter toe aan een heet kopje groene thee dan zult u vervolgens niet meer door het glas heen kunnen kijken zoals te zien in FIGUUR S.2.

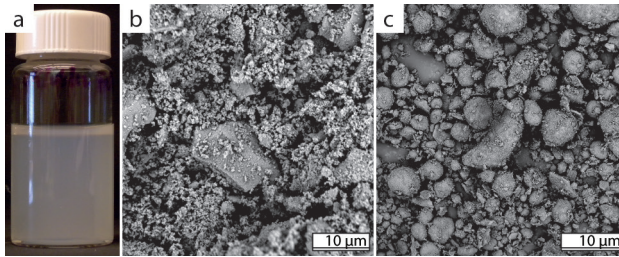
S.3 PYROFOSFAATZOUTEN

In dit proefschrift zoeken wij naar een manier om aan alle voorwaarden voor een goed aanvulsel te voldoen en toch ijzer en andere mineralen aan voedingsmiddelen toe te kunnen voegen. Het systeem dat wij hiervoor gebruiken is gekozen vanwege de volgende **drie criteria**: geen reactiviteit, geen textuur en geen kleur.

Geen reactiviteit. De reactiviteit van ijzer (en andere mineralen) geldt vooral voor het mineraal in oplossing. Om de reactiviteit te beperken is het ons doel om het ijzer in deeltjes te vangen die onoplosbaar zijn in voedingsmiddelen. In het lichaam moeten de deeltjes vervolgens wél oplosbaar zijn om het ijzer beschikbaar te maken voor opname.

Geen textuur. Nu wij voor een onoplosbaar materiaal hebben gekozen brengt dit een volgend probleem met zich mee. Het materiaal zal in het voedingsmiddel zitten als kleine korreltjes, en een theelepeltje zand in je melk of yoghurt levert geen 'plezierige smaaksensatie' op. Daarom willen we de deeltjes zo klein mogelijk maken, klein genoeg om geen textuur meer te geven. Dit brengt echter een ander probleem met zich mee: geen enkel materiaal is namelijk absoluut onoplosbaar. Er zal altijd een kleine hoeveelheid materiaal oplossen en dus beschikbaar zijn voor reactie. Nu is het zo dat hoe fijner het materiaal verdeeld is (dus hoe kleiner de deeltjes zijn), hoe hoger de oplosbaarheid wordt. Kleinere deeltjes zullen meer oplosbaar zijn dan grotere deeltjes, wat zal leiden tot een reactiever materiaal. Er zal dus een balans gevonden moeten worden tussen de lage reactiviteit van grote deeltjes en afwezigheid van textuur van kleine deeltjes. Het zal u niet verbazen dat de optimale grootte binnen de colloïdale definitie valt.

Geen kleur. Het laatste probleem is de keuze van het onoplosbare materiaal: zoals in het vorige stukje vermeld hebben bijna alle materialen die ijzer bevatten een sterke kleur. Hier is echter één uitzondering op, en dat is ijzer-pyrofosfaat. Een colloïdale dispersie van ijzer-pyrofosfaat is wit (zie FIGUUR S.3), heeft geen smaak, en de deeltjes zijn te klein om opgemerkt te kunnen worden door de consument. Bovendien is het materiaal onoplosbaar onder normale omstandigheden en dus toepasbaar in voedingsmiddelen, terwijl het onder sterk zure of basische omstandigheden geheel oplost. Dit zal het ijzer beschikbaar maken voor opname in een maag-darmstelsel.



FIGUUR S.3 Een colloïdale dispersie van ijzer pyrofosfaat (a). Sterk vergrote plaatjes van commercieel verkrijgbaar ijzer pyrofosfaat (b en c). De plaatjes zijn gemaakt met een electronenmicroscop, schaalbalken van 10 micrometer zijn aangegeven in de figuren.

Maar in FIGUUR S.1c is te zien dat ijzer-pyrofosfaat al toegevoegd wordt aan onze voedingsmiddelen! Waarom hebben we er dan nog een heel boekje over geschreven? Ten eerste bestaat het huidig verkrijgbare product uit grote, onregelmatige deeltjes van allerlei vormen en afmetingen (zie FIGUUR S.3) die over het algemeen te groot zijn om als colloïd bestempeld te mogen worden. Nu is dit voor droge voedingsmiddelen geen probleem, maar er zijn een paar kunstgrepen nodig om deze deeltjes ook toe te kunnen passen in vloeibare voedingsmiddelen. In een groot deel van dit proefschrift onderzoeken wij daarom (nieuwe) manieren om deze systemen te bereiden en zo een algemeen toepasbaar systeem te maken.

Ten tweede is de titel van het proefschrift ‘metaal-pyrofosfaat-zouten’, niet ‘ijzer-pyrofosfaat-zouten’: we willen niet alleen ijzer in de deeltjes vangen, maar ook andere essentiële mineralen. Dit maakt het systeem niet alleen nog breder toepasbaar, maar zal ook een ander voordeel hebben dat besproken zal worden onder het kopje EIGENSCHAPPEN.

Dit proefschrift is opgedeeld in drie secties genoemd naar de laatste drie termen uit de titel: bereiding, eigenschappen en toepassingen. In de komende alinea's wordt een overzicht gegeven van de inhoud van deze secties.

S.4 BEREIDING,

Hoe maak je een colloïdale dispersie van een onoplosbaar zout? Eén manier is om grote deeltjes van het materiaal te nemen (zoals in FIGUUR S.3b) en deze net zo lang te vermalen totdat ze de colloïdale afmetingen hebben. Voor deze methode is echter veel energie nodig en bovendien is er weinig controle over de grootte en vorm van de deeltjes die gevormd zullen worden. Daarom zoeken wij in deze sectie naar andere methoden voor het maken van onze systemen.

De methode die we in HOOFDSTUK 2 gebruiken wordt co-precipitatie genoemd. In deze methode worden eerst twee oplossingen van oplosbare zouten gemaakt, in ons geval één oplossing van ijzerchloride en één oplossing van natrium-pyrofosfaat. Wanneer die vervolgens aan elkaar toe worden gevoegd zal het onoplosbare zout ijzer-pyrofosfaat gevormd worden ('neerslaan') terwijl het overgebleven natriumchloride (keukenzout) in oplossing zal blijven (zie ook referentie [2]). In dit hoofdstuk laten we zien dat deze methode gebruikt kan worden om onder de juiste omstandigheden colloïdale deeltjes te vormen.

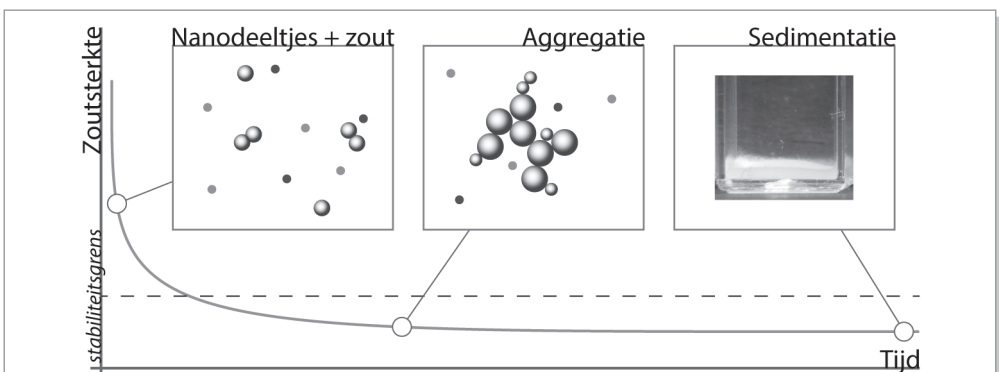
Maar omdat de co-precipitatie methode (net als het vermalen) óók weinig gecontroleerd is, gebruiken we in HOOFDSTUK 3 een andere methode, vergelijkbaar met het maken van kandijstokjes. Bij het maken van kandij gebruikt men het feit dat er meer suiker op kan

lossen in warm water dan in koud water: er wordt zoveel mogelijk suiker opgelost in heet water en de oplossing wordt vervolgens langzaam weer afgekoeld. Tijdens het afkoelen zal de suiker minder oplosbaar worden, waardoor het teveel aan suiker grote kristallen vormt op het stokje dat in de oplossing geplaatst is. Zou je de oplossing echter heel snel afkoelen, dan wordt de suiker niet op het stokje gevormd, maar juist overal tegelijk. Hierdoor worden er heel veel kleine suikerkristalletjes gevormd. Dit laatste gebruiken we in HOOFDSTUK 3 voor het maken van colloïdale metaal-pyrofosfaten, maar in plaats van een temperatuurverschil gebruiken we de pH, de zuurtegraad. Metaal-pyrofosfaat-zouten zijn namelijk oplosbaar bij lage pH (een zure oplossing). We laten zien dat wanneer we de pH eerst verlagen tot alles opgelost is en vervolgens weer heel snel verhogen (basisch maken), we gecontroleerd heel kleine, colloïdale deeltjes kunnen vormen.

In deze twee hoofdstukken vinden we dat het met de eerste methode alleen mogelijk is om colloïdaal ijzer-pyrofosfaat te bereiden, terwijl de tweede alleen gebruikt kan worden voor colloïdaal magnesium-pyrofosfaat. Hoewel beide methoden ook gebruikt kunnen worden om grote calcium- en zink-pyrofosfaatdeeltjes te maken, zijn de deeltjes te groot om binnen de colloïdale definitie te kunnen vallen.

S.5 EIGENSCHAPPEN

Vervolgens bestuderen we de colloïdale eigenschappen van de bereide systemen. IJzer-pyrofosfaat vertoont op het eerste gezicht zulk afwijkend gedrag dat we hier twee hoofdstukken aan wijden. In HOOFDSTUK 4 vinden we dat bij het maken van ijzer-pyrofosfaat de kleine deeltjes die gevormd worden direct aggregeren (samenklonteren), maar dat de aggregatie stopt voordat het systeem te groot wordt om buiten de colloïdale definitie te vallen. De dispersie die dan gevormd is kan vervolgens wekenlang stabiel blijven totdat het systeem uiteindelijk toch uitzakt. Er zijn dus blijkbaar twee tijdsschalen in ons systeem; de initiële instabiliteit (de kleine deeltjes aggregeren) en de uiteindelijke stabiliteit, die toch niet helemaal stabiel is. Na enig rekenwerk (zie APPENDIX III) bevestigen we dat dit aan de veranderende zoutsterkte ligt. Zoals eerder vermeld gebruiken we twee oplosbare zouten om één onoplosbaar zout te maken. Dit betekent dat voordat er deeltjes gevormd zijn de zoutsterkte hoger is dan wanneer alle deeltjes gevormd zijn. Voor de meeste



FIGUUR S.4 De veranderende zoutsterkte tijdens het vormen van het onoplosbare zout zorgt ervoor dat de deeltjes in het begin onstabiel zijn en direct aggregeren (a). Maar hoe meer deeltjes er gevormd zijn, hoe lager de zoutsterkte is, totdat de gevormde aggregaten stabiel zijn in dispersie (b). Ze zijn echter niet helemaal stabiel, aangezien ze na verloop van tijd toch uitzakken (c).

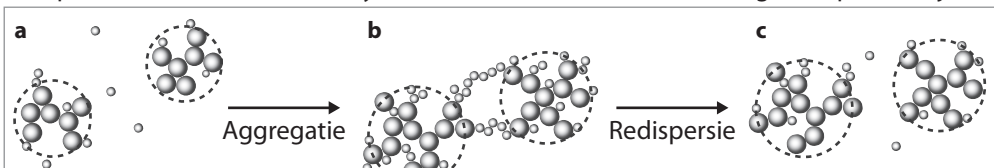
colloïdale dispersies geldt dat hoe hoger de zoutsterkte is, hoe minder stabiel de deeltjes zijn. Tijdens het vormen van de ijzer-pyrofosfaatdeeltjes gaat de zoutsterkte omlaag en passeert het systeem ergens de grens tussen colloïdale instabiliteit en stabiliteit zoals schematisch weergegeven in FIGUUR S.4.

In HOOFDSTUK 5 ontdekken we dat de deeltjes die uitgezakt zijn vrij eenvoudig weer in dispersie gebracht kunnen worden: de deeltjes wassen is voldoende om weer op een dispersie uit te komen vergelijkbaar met die in FIGUUR S.3. Dit wassen doen we door middel van dialyse, een term die u wellicht kent uit de medische wereld. Hierbij spoelen we schoon water langs de deeltjes die we gevangen houden in een 'membraan', een filter dat klein genoeg is om de deeltjes tegen te houden maar groot genoeg om het water en restproducten door te laten. Hierdoor houden we uiteindelijk alleen de deeltjes en schoon water over in het systeem. We onderzoeken de verschillende omstandigheden waaronder het mogelijk is om uitgezakte deeltjes weer in dispersie te krijgen en vinden dat dit zelfs kan met systemen waarbij het volgens de berekeningen uit het vorige hoofdstuk niet zou moeten kunnen. De geaggregeerde deeltjes zouden zo sterk aan elkaar geplakt moeten zitten dat alleen wassen niet voldoende kan zijn om ze weer los te krijgen. Hier blijkt de oplosbaarheid van kleine deeltjes weer een rol te spelen. De geaggregeerde deeltjes vormen niet één grote klomp, maar een open netwerk. Tijdens het wassen lossen de kleinste deeltjes in dit netwerk op, waardoor de afzonderlijke, colloïdale aggregaten weer in dispersie kunnen komen (redispersie), zie FIGUUR S.5 voor een schematische weergave van dit effect.

In HOOFDSTUK 6 gebruiken we de methoden uit HOOFDSTUKKEN 2 EN 3 om naast ijzer nog een tweede mineraal in de deeltjes te stoppen. We hopen hiermee de reactiviteit nog verder te verlagen door met het tweede mineraal de hoeveelheid ijzer aan het oppervlak van de deeltjes te verminderen. Zo lang de deeltjes onoplosbaar zijn, is alleen het ijzer aan het oppervlak van de deeltjes beschikbaar voor reactie en door het ijzer aan het oppervlak te verdunnen zal het systeem minder reactief zijn. In dit hoofdstuk vinden we dat we alleen stabiele colloïdale systemen kunnen maken wanneer de deeltjes óf heel veel ijzer (meer dan 80%), óf juist heel weinig ijzer (minder dan 5%) bevatten. De precieze oorzaak hiervan hebben wij helaas niet kunnen achterhalen. Net als in HOOFDSTUK 3 is het ook hier alleen met magnesium mogelijk om stabiele systemen te krijgen.

S.6 EN TOEPASSINGEN

In HOOFDSTUK 7 proberen we de mineralen nog verder te beschermen door een laagje eiwit (zeïne, een maiseiwit) op de deeltjes aan te brengen. We laten zien dat dit laagje eiwit de deeltjes stabielier maakt: een systeem zonder het eiwit zal binnen enkele weken compleet uitzakken, maar een systeem met zeïne kan maandenlang in dispersie blijven.



FIGUUR S.5 Redispersie door het oplossen van deeltjes. De colloïdale aggregaten (a) groeien langzaam uit tot open netwerken van deeltjes die te groot zijn om dispersie te blijven (b). Wanneer het systeem gewassen wordt lossen de kleine deeltjes op en komen de aggregaten weer in dispersie (c).

Verder laten we zien dat het eiwit niet alleen gebruikt kan worden om pyrofosfaat-zouten te beschermen, maar ook toegepast kan worden op verschillende andere soorten materialen. Zo bedekten we goud-, zilver- en ijzeroxide-deeltjes van verschillende vormen en afmetingen succesvol met een laag eiwit. Deze algemeenheid maakt de coatingsmethode potentieel erg interessant voor allerlei (biomedische) toepassingen.

HOOFDSTUK 8 is de uiteindelijke test voor de toepasbaarheid van de systemen uit dit proefschrift. Hier testen we de reactiviteit van het ijzer in de relevante systemen. Zoals in het begin besproken, is de reactiviteit van ijzer aan te tonen door de complexvorming met polyfenolen: beschikbaar ijzer zal direct binden aan de aanwezige polyfenolen en een sterke, paars tot zwarte kleur geven. Nu willen we wat wetenschappelijker te werk gaan dan gewoon onze systemen in een kopje hete thee te gieten en daarom gebruiken we een modelsysteem voor polyfenolen, namelijk galluszuur (*gallic acid*). Dit relatief kleine molecuul gedraagt zich vergelijkbaar met de grote polyfenolen uit voedingsmiddelen en kan daardoor dus goed als indicator gebruikt worden voor de reactiviteit van ijzer.

Uit al deze experimenten concluderen we dat het vangen van ijzer in de colloïdale deeltjes het ijzer inderdaad minder reactief maakt. Het toevoegen van een tweede mineraal verlaagt de reactiviteit onder bepaalde omstandigheden, en het aanbrengen van een extra eiwitlaagje beschermt de deeltjes nog verder.

Ik hoop dat ik u, door het schrijven van deze samenvatting, enigszins deelgenoot heb kunnen maken van het onderzoek dat me de afgelopen tijd heeft beziggehouden.

S.7 DANKWOORD

Ik wil Laura Rossi bedanken voor het maken van de SEM plaatjes in FIGUUR S.3.

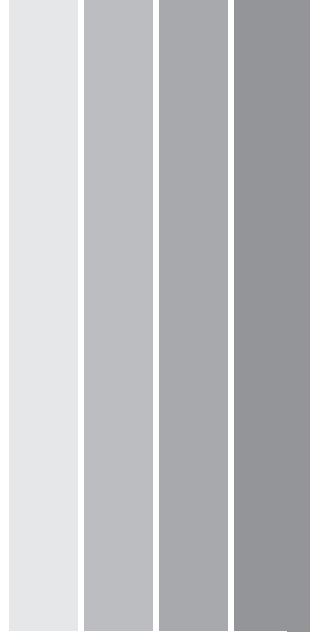
S.8 REFERENTIES

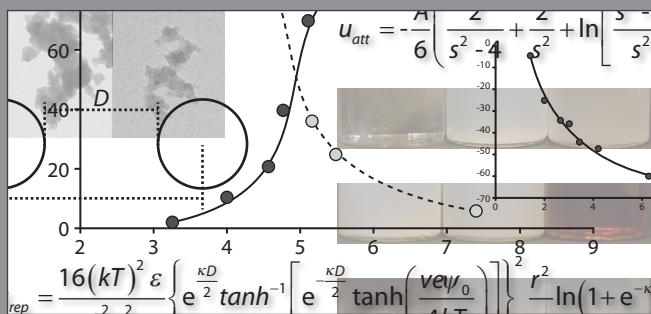
[1] Zie <http://nl.wikipedia.org/wiki/Galappel> en http://en.wikipedia.org/wiki/Iron_gall_ink.

[2] Vergelijkbare proeven worden gedaan op de middelbare school: zie bijvoorbeeld de neerslagtabellen uit BINAS, Tabel 45 A in de editie van mei 2004.

<http://www.ebook.noordhoff.nl/noordhoff/vo/binas/hv/pk/magazine.html>







APPENDICES

APPENDIX I COPRECIPITATION METHOD

I.A ADDITION ORDER AND SPEED

Besides the preparation method described in CHAPTER 2, variations on this method were tried as well. These are (i) reverse addition (addition of PP_i to Fe), (ii) injection addition and (iii) simultaneous addition. For the inverse addition the precursor solutions were simply swapped: 50 ml PP_i solution was added drop wise to 100 ml Fe^{3+} solution. For the injection method, one component was dissolved in 145 ml water in a 250 ml round bottom flask (rbf). The other component was dissolved in 5 ml and injected directly into the solution using a syringe while stirring. In the simultaneous slow addition method, 50 ml water was added to a 250 ml rbf and the Fe^{3+} and PP_i were dissolved in 50 ml water each. The two solutions were added drop wise to the rbf in about 15 minutes. For the simultaneous injection addition, the rbf was filled with 140 ml water. The Fe^{3+} and PP_i were dissolved in 5 ml water each and simultaneously injected into the water. Final concentrations of Fe^{3+} and PP_i were identical for all reaction methods. All used methods are summarized in TABLE A.1

	Code	V_{Fe} (ml)	V_{PP_i} (ml)	V_{water}^* (ml)	Method	$[Fe]^{**}$ (mmol)	$[PP_i]^{**}$ (mmol)
Fe to PP_i (used in chapter)	<i>N</i>	50	100		Drop wise (15 min)		
PP_i to Fe	<i>P</i>	100	50	0			
Fe inject	<i>Fi</i>	145	5		Syringe (inject)	0.857	0.643
PP_i inject	<i>Pi</i>	5	145				
Simultaneous slow	<i>Ss</i>	50	50	50	Drop wise (15 min)		
Simultaneous inject	<i>Si</i>	5	5	140	Syringe (inject)		

* V_{water} indicates the volume of water added to the rbf in case of the simultaneous addition method.
 **Concentration in final volume.

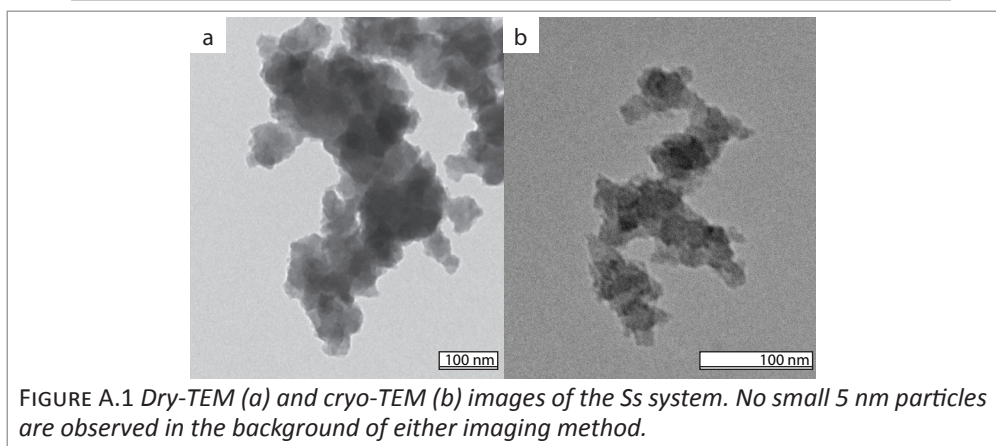


FIGURE A.1 Dry-TEM (a) and cryo-TEM (b) images of the *Ss* system. No small 5 nm particles are observed in the background of either imaging method.

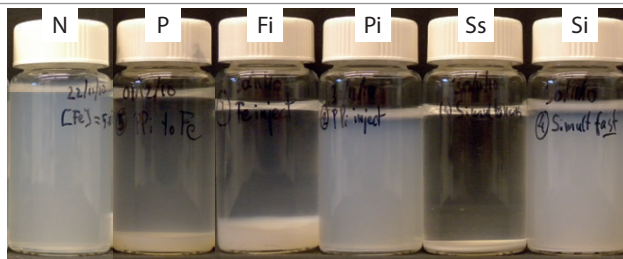


FIGURE A.2 Dispersions of all preparation methods, one day after preparation.

(Cryo-)TEM analysis of all the prepared dispersions yielded similar images to what is shown in CHAPTER 2. The only exception to this was the *Ss* sample, which showed more compact clusters and lacked the smaller nanoparticles, see FIGURE A.1a. In the cryo-TEM images the clusters again resemble those found in the other preparation methods, but the smaller particles are still missing, FIGURE A.1b.

One day after preparation a clear difference in dispersion stability could be seen between samples of the different preparation methods, see FIGURE A.2. DLS analysis reflects this difference: *N*, *Pi* and *Si* yield stable dispersions with cluster sizes around 200 nm while *P* and *Ss* are completely sedimented with cluster sizes too large and polydisperse to be accurately determined, see TABLE A.2. Sample *Fi* shows different behavior in that the cluster size was around 200 nm immediately after preparation, but after one day the dispersion had completely sedimented and cluster size had grown to 1200 nm. All samples showed high polydispersity in cluster size (>30%), correlation functions always showed smooth curves with no discontinuities or anomalous noise unless noted otherwise (not shown). Ultrasonication of the samples during or after preparation yielded no difference in cluster size. Zeta-potentials were around -40 mV at pH 3.6 and a conductivity of 2.3 mS/cm for all samples.

I.B CLUSTER SIZE AND ZETA POTENTIAL

We prepared three new samples at different cluster size by varying the stirring speed during addition. Faster stirring speeds resulted in smaller particles. As can be seen from TABLE A.3, there was no clear relation between size and zeta-potential.

TABLE A.2 DLS diameter fresh and one day after preparation

Sample	Fresh (nm)	One day (nm)
<i>N</i>	200	200
<i>P</i>	3000*	**
<i>Fi</i>	230	1200*
<i>Pi</i>	210	210
<i>Ss</i>	6000*	**
<i>Si</i>	310	320

*Indicative value. Particles too large and polydisperse for reliable analysis.

**Not analyzed

TABLE A.3 Zeta-potential dependent on cluster size

Sample	Size (nm)	Zeta potential (mV)	Conductivity (mS/cm)
1	460	-36.6	2.21
2	313	-38.8	2.24
3	192	-34.0	2.19

APPENDIX II SOLUBILITY AND ISO-ELECTRIC POINT DETERMINATION

II.A SOLUBILITY OF IRON PYROPHOSPHATE

PREPARATION. For determination of absolute solubility, FePP_i was precipitated in the same way as described in CHAPTER 4. The precipitate was centrifuged and washed 6 times with MQ, and another 3 times with acetone. The sample was then dried 4 days at room temperature, after which 0.5 grams of the white powder was added to 20 ml water and stirred for four days. The sample was again centrifuged and the supernatant filtered and analyzed for elemental content using ICP-AES at the Geo-lab in Utrecht.

RESULTS. The solubility of iron pyrophosphate at pH 3.8 and a solid content of 25 g/L (0.14 M iron, 0.11 M pyrophosphate assuming pure FePP_i) was determined to be 0.61 mM iron and 0.67 mM pyrophosphate. Solubility of similar materials have been shown to vary with experimental conditions such as solid content [5].

II.B pH-DEPENDENT SOLUBILITY OF FePP_i AND CaPP_i

PREPARATION. The pH dependent solubility analysis of CaPP_i was performed by precipitating the reactants in roughly 80 ml, adjusting the pH of the solution with 1 M NaOH or HCl and filling to 100 ml. For this, the molar amounts were adapted to 100 ml final volume instead of the usual 150 ml. The resulting liquid was centrifuged and the supernatant analyzed using AAS. Samples needed to be acidified for AAS measurements. For this and for background correction, the samples were prepared by mixing 0.4 ml of the supernatant, 10 ml 10% KCl solution, 10 ml 4 mM AlCl_3 solution and 1.2 ml 1 M HCl and filled to 100 ml.

FePP_i samples could not be prepared in an acidic medium as they precipitated even at these low concentrations. Therefore, we used the spectrophotometric analysis method of Fortune *et al.* [6] for the solubility analysis of FePP_i . This method uses the Fe^{II} -o-phenantrolene complex, the Fe^{III} present is reduced to Fe^{II} using Hydroxylamine HCl.

RESULTS. It is interesting to observe that the pH dependent solubility of $\text{M}^{\text{II}}\text{PP}_i$ and $\text{Fe}^{\text{III}}\text{PP}_i$ are reversed: while iron pyrophosphate was insoluble at low pH, pyrophosphate salts of divalent metals dissolved at low pH, see FIGURE A.3. The range differs for M^{III} , as LaPP_i is insoluble at all pHs (it first dissolves at low pH, then precipitates again), while AlPP_i is only insoluble at intermediate pH. Here it should be noted that FePP_i can be dissolved completely in strong acid as well [7]

After preparation, FePP_i had a pH of 3.3 while CaPP_i was at 7.3. pH-dependent analysis of the solubility is shown in FIGURE A.4 and again shows the reversed solubility of metal-pyrophosphates depending on the valence of the cation. Such accurate analysis of mixed systems proved exceedingly difficult due to this difference in pH dependent solubility. We attempted to dissolve all species at low pH using strong ligand molecules such as EDTA, but were unable to successfully prepare stable solutions at low or high pH.

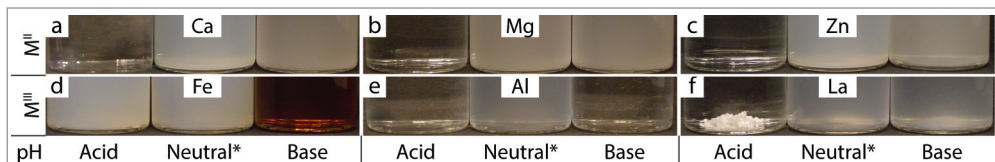


FIGURE A.3 pH dependent solubility of metal pyrophosphate salts at three different pHs: acidic, neutral and basic. Top row: divalents cations: (a) calcium, (b) magnesium and (c) zinc. Bottom row: trivalents cations: (a) iron(III), (b) aluminium, (c) lanthanum. *Neutral indicates the pH after preparation, which is not necessarily pH 7.

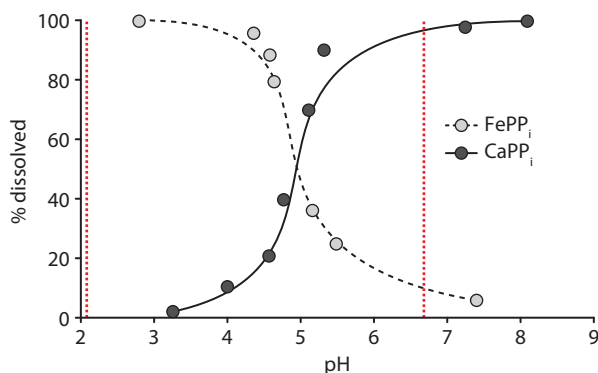


FIGURE A.4 Detailed pH dependent solubility of FePP_i (dark circles) and CaPP_i (light circles). Closest pK_a values of pyrophosphate are indicated with dotted lines (see TABLE A.4)

TABLE A.4 pK_a values of pyrophosphate [3]

Step	pK_a
1	0.91
2	2.10
3	6.70
4	9.32

II.C DETERMINATION OF THE ISO-ELECTRIC POINT

PREPARATION. Samples for the determination of the iso-electric point (IEP) of FePP_i were prepared using the coprecipitation method (see CHAPTER 2). The pH of the dispersion was adjusted by adding 1 M HCl or NaOH, the total ionic strength of the solution was kept constant over the range of pHs by addition of NaCl.

RESULTS. FIGURE A.5 shows that the IEP of FePP_i could not be reached at the solid content that was used. The zeta-potential was close to -4 mV at a pH of 1.4, below which the FePP_i started to dissolve completely. Zeta-potentials above pH 6 were inaccurate as the material started to dissolve in these samples as well.

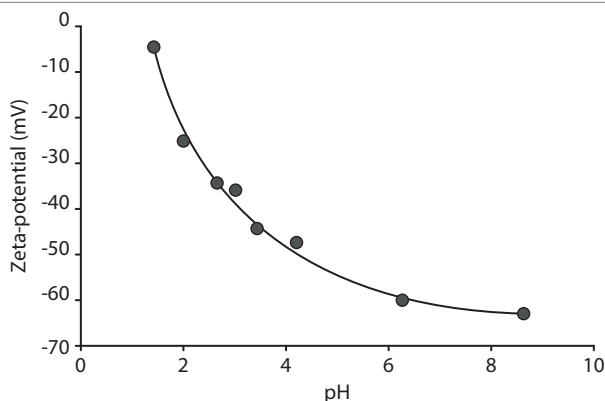


FIGURE A.5 Determination of the iso-electric point: pH-dependent zeta-potential for FePP_i . The IEP cannot be reached for this system, as the zeta-potential is still negative at the lowest pH.

APPENDIX III INTERACTION POTENTIALS

III.A SCHULZE-HARDY RULE AND CALCULATION OF INTERACTION POTENTIALS

The Schulze-Hardy rule (SHR) states that the concentration of electrolyte needed to critically destabilize a dispersion (see Chapter 4 for details) inversely scales with ion valence to the power six [1]. Plotting the critical coagulation concentrations (ccc) found in Figure 4.4 in a log-log fashion in FIGURE A.7 we find a slope of -5.5, in close agreement with the SHR (red line). Verwey and Overbeek have shown that the DLVO theory is consistent with the Schulze-Hardy rule [1, 2]. From their work on the stability of colloids they found that the critical coagulation concentration ccc (in molar) can be calculated by

$$ccc = \frac{98.5(k_B T)^5 (\epsilon)^3}{N_{av} e^6} \cdot \frac{\gamma^4}{v^6 A^2} \quad (A1)$$

in which k_B is the Boltzmann constant, T absolute temperature, ϵ the permittivity of the solvent, N_{av} Avogadro's number, e the elementary charge, v the valence of the electrolyte, A the Hamaker constant (in Joules) and

$$\gamma = \tanh \frac{ve\psi_0}{4k_B T} \quad (A2)$$

with ψ_0 the surface potential in mV. In the case of high surface potential ($\psi_0 > 100$ mV), and therefore $ccc \sim 1/v^6$ in agreement with the SHR. Equation (A1) is the solution of the combination of the van der Waals attraction and the double layer repulsion, which can be done analytically for two spheres at small separation distances ($r \gg D$, see Figure A.6). However, the limits $\psi_0 > 100$ mV and $r \gg D$ do not hold for our system, as zeta potentials are around 40 mV and r is close to D as we will show. Calculations have been done in literature for small particles at larger separation distances (large κ) [3, 4], showing that the full treatment of the repulsion and attraction potentials will result in a radius dependent ccc. Here we compare the results of the 'simplified' ccc as written in equation (A1) with three numerical solutions. All of these solutions use same full attraction potential:

$$u_{att} = -\frac{A}{6} \left(\frac{2}{s^2 - 4} + \frac{2}{s^2} + \ln \left[\frac{s^2 - 4}{s^2} \right] \right) \quad (A3)$$

where $s = x/r$, r the particle radius and x the center-to-center distance between two particles, see FIGURE A.6 [1]. The more commonly used approximated form $u_{att} = -Ar/12D$ is

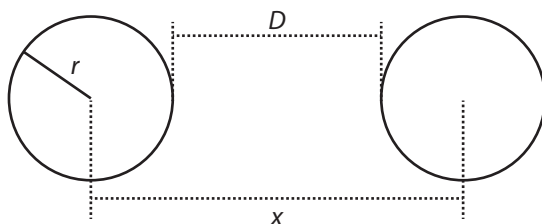


FIGURE A.6 The three size variables r (radius), x (center-to-center distance) and D (surface-to-surface distance).

again only valid for $r \gg D$.

The three repulsion potentials used for our calculations are:

1. The repulsion potential commonly used for calculation of the ccc; a screened potential with $r \gg D$

$$u_{rep} = \frac{64\pi k_B T r \rho}{\kappa^2} \gamma^2 e^{-\kappa D} \quad (A4)$$

with ρ the ionic strength in particles per m^3 , D the distance between the particle surfaces ($x-2r$) and κ the inverse Debye length [2]

2. The screened potential at low surface potential without the assumption that $r \gg D$:

$$u_{rep} = \frac{4\pi r^2}{x} (e\psi_0)^2 e^{-\kappa D} \quad (A5)$$

3. An approximate solution for two spheres at large κr and moderate to high surface potentials [4]

$$u_{rep} = \frac{16(kT)^2 \varepsilon}{e^2 v^2} \left\{ e^{\frac{\kappa D}{2}} \tanh^{-1} \left[e^{-\frac{\kappa D}{2}} \tanh \left(\frac{ve\psi_0}{4kT} \right) \right] \right\}^2 \frac{r^2}{x} \ln(1 + e^{-\kappa D}) \quad (A6)$$

For each of these interactions, the surface potential ψ_0 is approximated by the experimental zeta potential for each valence Table 4.1 and the total interaction is numerically solved for κ and D simultaneously. As can be seen from the results, the deviation for smaller particles between the different full calculations is negligible in the log-log plot, while the models do differ significantly from the simplified form, see FIGURE A.7. The Hamaker constant found from these calculations is $25 k_B T (1.0 \cdot 10^{-19} \text{ J})$.

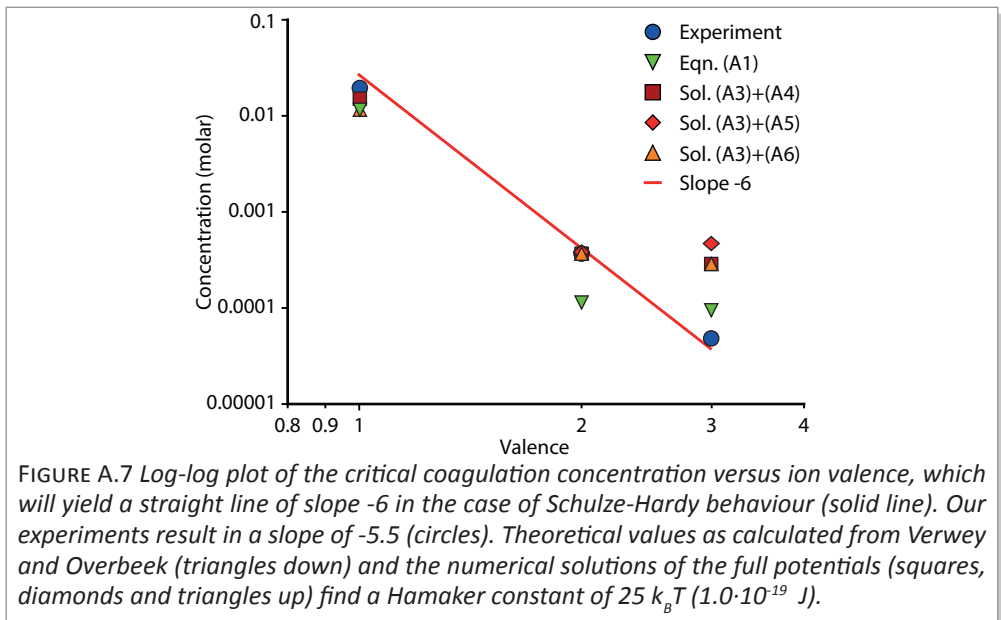


FIGURE A.7 Log-log plot of the critical coagulation concentration versus ion valence, which will yield a straight line of slope -6 in the case of Schulze-Hardy behaviour (solid line). Our experiments result in a slope of -5.5 (circles). Theoretical values as calculated from Verwey and Overbeek (triangles down) and the numerical solutions of the full potentials (squares, diamonds and triangles up) find a Hamaker constant of $25 k_B T (1.0 \cdot 10^{-19} \text{ J})$.

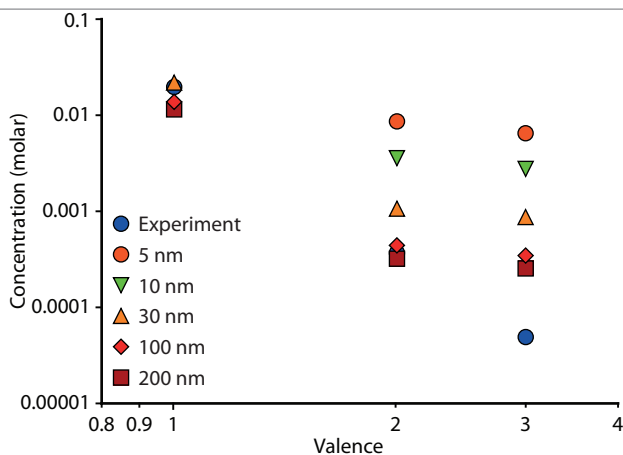


FIGURE A.8 Log-log plot of the ccc as a function of the particle radius, obtained by numerical solution of eqns. (A3) and (A6). The other repulsion potentials give similar results.

As was mentioned above, the numerical solutions of the combined attractive and repulsive potentials (e.g. solving eqn. (A3) and (A5)) are radius dependent, as the radius will only cancel when using the assumptions necessary for the analytic solution (resulting in eqn. (A1)). This radius dependence is illustrated in FIGURE A.8, where we calculate the ccc for particles of various sizes by numerical solution of eqn. (A3) and (A6). At radii larger than 100 nm the radius dependence is negligible: we return to the limit of $r \gg D$ and the value of the ccc converges. However, at smaller radii the deviation becomes significant: the slopes of the calculated values are -1.5 and -2.4 for the 5 and 20 nm particles, respectively. Therefore, the results in FIGURE A.7 were calculated using a particle radius of 130 nm. However, this does not agree to the TEM images which show particles of 5 and 20 nm observed in CHAPTER 4. Apparently the size of the aggregates is the physically relevant length scale in this system, not the size of the primary particles as would have been expected.

III.B MIXED SYSTEMS, ZETA-POTENTIAL

We have recalculated the interaction potentials for the mixed systems and found that substituting part of the Fe^{III} with M^{II} does not significantly change the potentials: the difference between pure FePP_i and the 4:1 ratio system is within 8% (not shown).

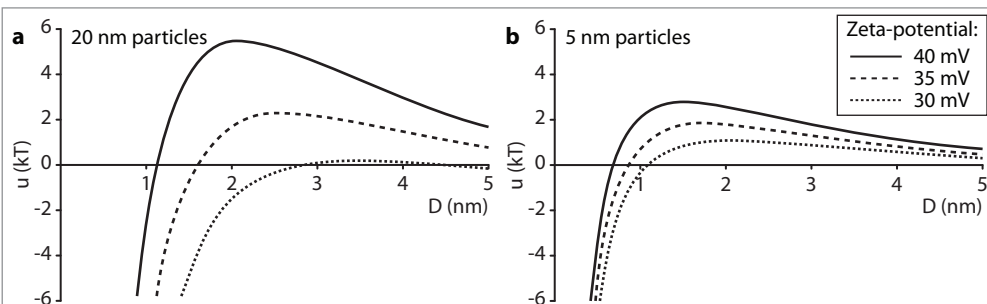


FIGURE A.9 Influence of zeta-potential on 20 nm (a) and 5 nm particles (b). Calculated at zeta-potentials of 35 mV (dotted line), 40 mV (dashed line) and 45 mV (solid line). All at final concentration after complete precipitation ($[\text{PP}_i] = 0 \text{ mM}$).

Furthermore, there was little difference between the M^{II} and Na substituted systems. The zeta-potential has a much stronger influence on the stability of the particles, see FIGURE A.9c and d. Especially the stability of the 20 nm particles is very sensitive to the zeta potential, as the particles go from no stabilizing barrier at 35 mV to a barrier of roughly $6 k_B T$ at 45 mV.

APPENDIX IV EXCESS M^{III} AND Fe^- OR PP^- -DEFICIENT SYSTEMS

IV.A HIGH-SALT SYSTEMS WITH M^{III} AS BACKGROUND IONS.

Addition of 1 M Al^{3+} or Fe^{3+} completely dissolved the $FePP_i$, see FIGURE A.10. This might be caused by the lowered pH, see TABLE A.5.



FIGURE A.10 M^{II}/M^{III} excess dispersions: (a) Freshly prepared $FePP_i$, (b) 1M $MgCl_2$, (c) 1M $AlCl_3$, (d) 1M $FeCl_3$.

IV.B IRON- OR PYROPHOSPHATE-DEFICIENT SYSTEMS

Iron- or pyrophosphate-deficient samples were prepared by reducing the amount of the respective salt by 10% during preparation. The PP_i deficient systems had a positive zeta-potential that was insufficient to keep the system dispersed, see TABLE A.6. The Fe -deficient system remained stable but did not have an increased zeta-potential that might be expected for an electrocratic system.

TABLE A.5 pH of $FePP_i$ dispersions

	Concentr. (M)	pH
No salt*	0	3.30
Li^+	2	2.84
K^+	2	2.69
Mg^{2+}	1	2.68
Al^{3+}	1	1.79
Fe^{3+}	1	0.81
Fe^{3+} 10%	0.0002	2.80

*No additional salt: freshly prepared $FePP_i$ system.

TABLE A.6 10% Fe or PP_i deficient systems

	Size (nm)	zeta potential (mV)	Conduct. (mS/cm)
Stoichiometry	210	-37	2.2
Fe deficit	250	-40	2.1
PP_i deficit	*20000	*4.2	2.5

*Indicative values, size and measurement polydispersity too large for accurate analysis.

APPENDIX V TEM-TOMOGRAPHY: NANOPARTICLE DISTRIBUTION IN ZEIN COMPOSITE SYSTEMS

To see how the nanoparticles were distributed throughout the composite particles we performed TEM tomography on magnetite-containing systems. FIGURE A.11a shows that the magnetite is indeed distributed evenly throughout the NP-Z particles as intended. The coverage in the Z-NP and Z-NP-Z particles was lower, however, and it is therefore harder to say where the majority of the NPs are actually located, see FIGURE A.11b and c. Furthermore, analysis of the Z-NP particles shows the particles slightly below the surface, instead of on top of it as would be expected. This is most likely due to drying effects and cryo-TEM tomography might give different results. However, for both the Z-NP and Z-NP-Z systems the NPs are situated mainly slightly below the surface and not in the center of the particles. The poor resolution in the X and Y planes is due to sub-optimal stack alignment as no tracer particles were added prior to analysis.

Here it should be noted that preparing zein-containing samples suitable for tomography is laborious. While the material does not suffer from beam damage significantly, drying the dispersions on the TEM-grids often leads to molten, aggregated and/or coalesced particles for unknown reasons. Only at very low particle concentrations usable samples are sometimes obtained. As can be observed in FIGURE A.11b, the Z-NP particle is asymmetric due to these drying effects.

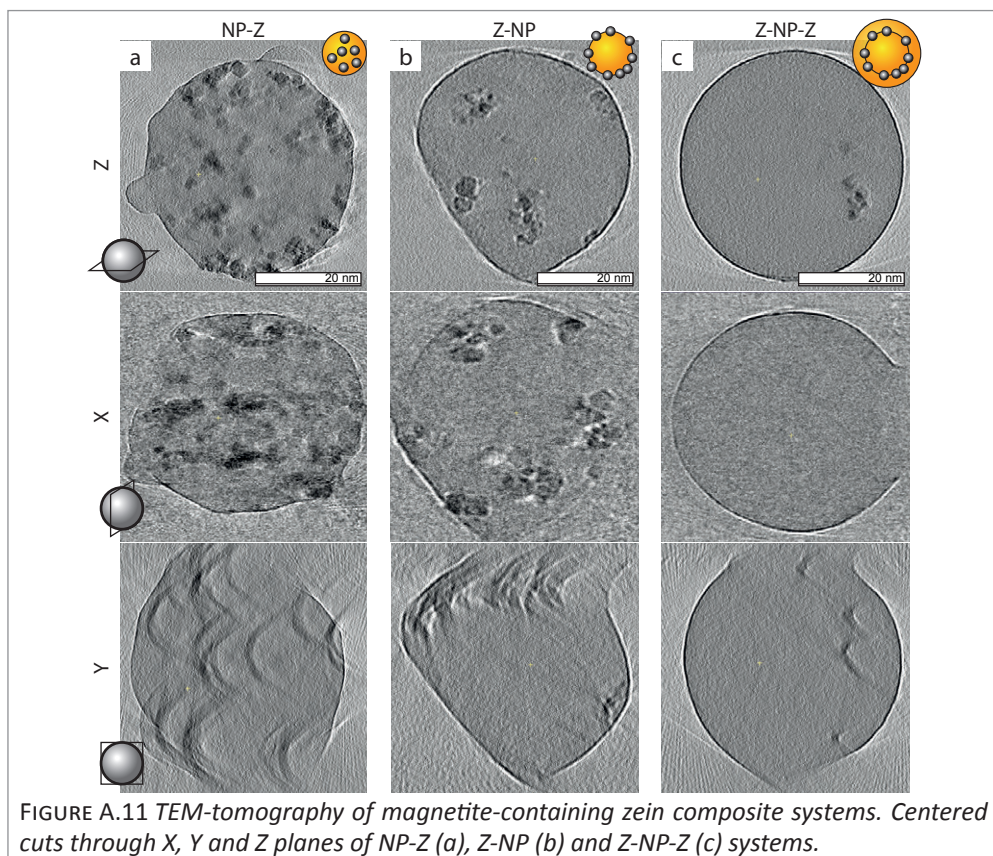
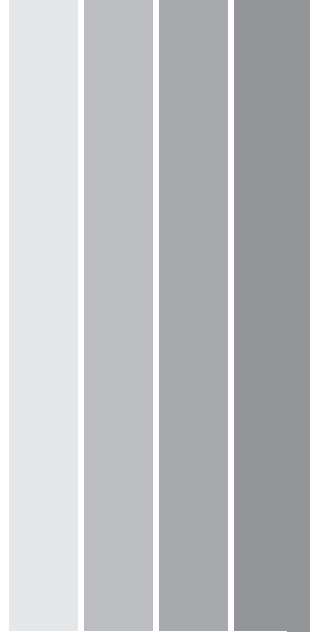


FIGURE A.11 TEM-tomography of magnetite-containing zein composite systems. Centered cuts through X, Y and Z planes of NP-Z (a), Z-NP (b) and Z-NP-Z (c) systems.

- [1] Verwey, E. J. W.; Overbeek, J. T. G. In *Theory of the Stability of Lyophobic Colloids*; Dover Publications, Inc.: 1999.
- [2] Israelachvili, J. N. In *Intermolecular & Surface Forces*; Academic Press, Inc.: 1985.
- [3] Sader, J. E.; Carnie, S. L.; Chan, D. Y. C. Accurate Analytic Formulas for the Double-Layer Interaction between Spheres. *J. Colloid Interface Sci.* **1995**, *171*, 46-54.
- [4] Hsu, J. P.; Liu, B. T. Effect of Particle Size on Critical Coagulation Concentration. *J. Colloid Interface Sci.* **1998**, *198*, 186-189.
- [5] Leach, S. A. Electrophoresis of Synthetic Hydroxyapatite. *Arch. Oral Biol.* **1960**, *3*, 48-56.
- [6] Fortune, W. B.; Mellon, M. G. Determination of Iron with O-Phenanthroline: A Spectrophotometric Study. *Industrial and Engineering Chemistry* **1938**, *10*, 60-64.
- [7] Haynes, W. M. In *Handbook of Chemistry and Physics*; Lide, D. R., Ed.; CRC Press: Boca Raton, FL, 2011.



DANKWOORD

One must be sane to think clearly, but one can think deeply and be quite insane. [1]

Als je vier jaar lang aan één onderwerp hebt gewerkt dan zou je kunnen stellen dat je hier diep over na hebt gedacht. Het feit dat ik vier jaar lang over colloïdale metaal-pyrosfosfaat-zouten na heb kunnen denken en tóch mijn geestelijke gezondheid heb weten te behouden, heb ik dan ook aan een heleboel mensen te danken. In vier jaar tijd komen er veel mensen voorbij en hoe lang ik de lijst ook maak, ik weet zeker dat ik mensen zal vergeten, waarvoor alvast mijn excuses. Hier volgt een hopelijk zo compleet mogelijke lijst van (in volkomen willekeurige volgorde) alle mensen die me in de afgelopen vier jaar geholpen, vermaakt, beziggehouden of gesteund hebben en die ik daar graag voor wil bedanken.

PROMOTOREN		CO-PROMOTOR
Willem	Albert	Krassi
STUDENTEN		
Jenneke	Simone Vissers	Simone Droog
Quinten	Ludo	Ali
Jasper	Addy	Niek
OFFICEMATES		
Tian Hui	Laura	Esther van den Pol
Rocio	Mark	
FCC LEDEN		
Susanne	Sonja	Anke
Bas	Joost	Chris
Esther Groeneveld	Rob	Roel
Julius	Jos	Karel
Lia	Maurice	Henk
Andrei	Ben	Jan Groenewold
Dzina	Marina	Dima
Ping	Jaakko	
SUPPORT		
Hans Meeldijk	Dominique	Kanvaly
Bonny		
SOUS LE ROC		
Merlijn	Sigrid	Rinke
Maaïke	Maj	Floris
Eric	Leonie	Eveline
Poy	Robert	Peter
Martijn	Inge	Daan
Marjan	Tikoi	Marieke
Joop	Judith	

EXTRA-CURRICULAIRE ACTIVITEITEN

Tamara	Marije	Albert
Lodewijk	Emiel	Bart
Matti	Hilde	Loek

BROOD EN SPELEN

Janne-Mieke	Winnie	Tiemen
Tim	Percy	Tijn Rams

VERY SPECIAL THANKS TO

Hans	Tijn
Hilleke	Luc
Jorn	Herma
	Stef

PARANIMFEN

Merel
Jan

REFERENTIE

[1] Tesla, N.; Radio Power Will Revolutionize the World, *Modern Mechanics and Inventions*. 1934, July.

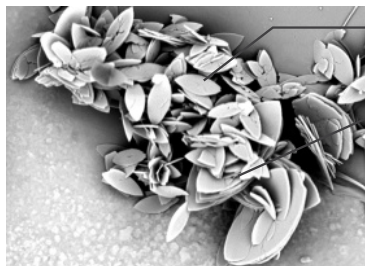
YOURI MIKAL VAN LEEUWEN



E-mail: ymvleeuwen@gmail.com
 Web: www.ymvanleeuwen.nl

2008 - 2013 PHD RESEARCH

COLLOIDAL METAL PYROPHOSPHATE SALTS



PhD at the Van 't Hoff Laboratory, Utrecht University || The research resulting in the thesis you are currently holding

Collaboration with Unilever Research, funded by Agentschap NL
 Preparation and characterization of colloidal food fortification systems for the addition of nutritional minerals.



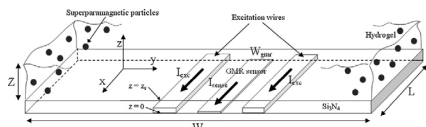
2006 - 2008 MASTER'S DEGREE CHEMISTRY AND PHYSICS

CUM LAUDE

2006 || *Master Thesis* || Sensors for in-body monitoring



2008 || *Research Project* || Studies of Metallic Nanoparticles: from Synthesis to Optical Properties and Interactions



Research project at Philips Research and the Van 't Hoff Laboratory on the preparation and testing of biosensors based on colloidal systems



Research at the Colloid Chemistry group of Prof. dr. L.M. Liz-Marzán, Spain. Synthesis of goethite-silica-gold composite nanoparticles and analysis with Near-field Scanning Optical Microscopy.



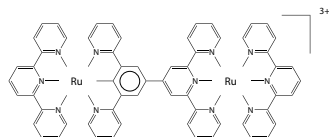
2002 - 2006 BACHELOR'S DEGREE CHEMISTRY

CUM LAUDE

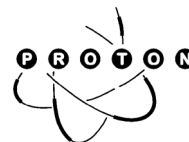
2006 || *Bachelor Thesis* || Synthesis of an asymmetric bimetallic dye: A possible two step upconverter



2003 || *U.S.S. Proton* || External Relations



Research project on organic synthesis at the Organic Chemistry group of Prof. dr. G. van Koten



Member of the Board of the *Utrecht Chemistry Students Association Proton*. Responsible for acquisition of funds and maintaining relationships with external parties (mainly companies).